SURFACE ENERGY BALANCE ALGORITHM FOR LAND (SEBAL) BASED EVAPOTRANSPIRATION ESTIMATION IN LOWER GILGEL ABAY CATCHMENT TANA SUB-BASIN, ETHIOPIA.

MASTER OF SCIENCE IN WATER RESOURCE ENGINEERING AND MANAGEMENT

TEWODROS KASSAYE SEMAW

HAWASSA UNIVERSITY, HAWASSA ETHIOPIA

MARCH 2018 G.C

SURFACE ENERGY BALANCE ALGORITHM FOR LAND (SEBAL) BASED EVAPOTRANSPIRATION ESTIMATION IN LOWER GILGEL ABAY CATCHMENT TANA SUB-BASIN, ETHIOPIA.

TEWODROS KASSAYE SEMAW

A THESIS SUBMITTED TO THE FACULTY OF BIO SYSTEM AND
WATER RESOURCE ENGINEERING,
SCHOOL OF GRADUATE STUDIES

INSTITUTE OF TECHNOLOGY

HAWASSA UNIVERSITY

HAWASSA ETHIOPIA

IN THE PARTIAL FULFILMENT OF THE REQUIREMENT FOR THE DEGREE OF

MASTER OF SCIENCE IN WATER RESOURCE ENGINEERING AND MANAGEMENT

MARCH 2018 G.C

SCHOOL OF GRADUATE STUDIES

HAWASA UNIVERSITY

ADVISORS' APPROVAL SHEET

(Submission sheet -1)

This is to certify that "**Tewodros Kassaye Semaw**" submitted in partial fulfillment of the requirements for the degree of master's with specialization in **Water Resource Engineering and Management, the graduate program of the Bio-systems and Environmental Engineering, and has been certified out by Water Resource Engineering and Management Id. No WREM/0067/05 under our supervision**. Therefore, we recommend that the student has fulfilled the requirements and hence hereby can submit the thesis to the department.

Dr. Sirak Tekleab ____ ____________________ ____________
Major advisor **Signature** **Date**

Dr. Marco Napoli ____ ____________________ ____________
Co-advisor **Signature** **Date**

Acknowledgements

First and for most my deep greatest thanks go to Almighty God, for giving me strength and courage to continue my study and for all things done in all my life.

Then, for all your sincere, faithful and immense devotion to help me for the accomplishment of this thesis work and to bring me here from the start, much appreciation is expressed for my advisers **Dr. Sirak Tekleab and Dr. Marco Napoli**. Your ultimate and sweet advice that smoothen my educational journey, it could not be otherwise, is printed in my heart.

Special thanks are goes to Dr. Brook A., Dr. Mihret D., Dr. Feto, Dr. Abraham W/M., Dr. Awdenegest M., Desalegn J., Ato Yohaness M., Dr. Amlaku Asres (Director of ORDA) and others for their honest friendship and cooperation for the accomplishment of this study.

In addition, the generous support and contribution of all my colleagues, friends, families and relatives are deeply acknowledged and emphasized in all case of my future life.

Dedication

I dedicate this thesis manuscript to my late Mother ***Kelemua Demeke*** *while I was conducting master's program in Italy; for my father Kassaye Semaw, for my baby and my wife and my sisters and brothers for nursing me with affection and love and for their dedicated partnership in the success of my life.*

Table of Contents

List of Tables

List of Figures

List of Acronyms and Abbreviations

Symbol	Description	Unit
ET	Actual evapotranspiration rate	mm/hr
ASTER	Advanced Space borne Thermal Emission and Reflection Radiometer	
AVHRR	Advanced Very High Resolution Radiometer	
rah	Aerodynamic resistance to heat transport	s/m
ρ	Air density	kg/m^3
Cp	Air specific heat	J/kg/K
αtoa	Albedo at top of atmosphere	-
αpath-radiance	Albedo path radiance	0.03
ASCE	American Society of Civil Engineers	
γ	Aspect angle of the pixel	Radians
εa	Atmospheric emissivity	-
AWS	Automatic weather station	
BREBS	Bowen ratio energy balance systems	
εo	Broad band surface emissivity	-
Rc	Corrected thermal radiance from the surface	$W/m^2/sr/\mu m$
CWSI	Crop Water Stress Index	
DOY	Day of the year	-
DST	Daylight savings time	
δ	Declination of the earth	Radians
Ts-DEM	DEM adjusted temperature	
DEM	Digital elevation model	
ECS	Eddy correlation systems	
EMA	Ethiopian Meteorological Agency	
ETrF	ETr fraction	-
Eto	Evapotranspiration	mm/day
ESUN	Exo-atmospheric spectral solar irradiance	$W/m^2/\mu m$
FAO	Food and Agricultural Organization	
u*	Friction velocity	m/s
GRASS	Geographic Resources Analysis Support System	
g	Gravitational force	m/s^2

GMT	Greenwich mean time	
z	Height	m
RL↓	Incoming longwave radiation	W/m^2
RS↓	Incoming shortwave radiation	W/m^2
ETinst	Instantaneous ET	mm/hr
iNDVI	integrated NDVI	
ITCZ	Inter Tropical Convergence Zone	
dr	Inverse squared relative earth-sun distance	-
λET	Latent heat flux	W/m^2
LE	Latent heat flux	
λ	Latent heat of vaporization	J/kg
φ	Latitude of the pixel	Radians
LAI	Leaf area index	
METRIC	Mapping Evapotranspiration at High Resolution and with Internalized Calibration	
MoWIE	Mister of Water, Irrigation and Electricity	
MODIS	Moderate Resolution Imaging Spectro radiometer	
Zom	Momentum roughness length	m
L	Monin-Obukhuv length	m
MDT	Mountain Daylight Savings Time	
ϖ	Mountain wind speed weighting coefficient	-
Rsky	Narrow band downward thermal radiation for a clear sky	W/m^2/sr/µm
εNB	Narrow band surface emissivity	-
τNB	Narrow band transmissivity of air	-
NOAA	National Oceanic and Atmospheric Administration	
NIR	Near Infrared	
Ta	Near surface air temperature	K
Rn	Net radiation flux	W/m^2
NDVI	Normalized Difference Vegetation Index	
Ts	Surface temperature	K
OLI/TIRS	Operational Land Imager/Thermal Infrared Sensor	
RL↑	Outgoing longwave radiation	W/m^2
Lp	Path radiance in the 10.4 – 12.5 µm band	W/m^2/sr/µm

Etr	Reference evapotranspiration	mm/hr
REF-ET	Reference evapotranspiration	
$\rho\lambda$	Reflectivity for band λ	-
RS	Remote sensing	
H	Sensible heat flux	W/m^2
SWIR	Shortwave Infrared	
τsw	Shortwave transmissivity of air	-
SAVI	Soil adjustment vegetation index	
G	Soil heat flux	W/m^2
Td	Soil surface air specific heat at constant pressure	
dT	Soil to atmosphere temperature difference	
SVAT	Soil Vegetation Atmosphere Transfer	
GSc	Solar constant	1,367 W/m^2
β	Solar elevation angle	Degrees
θ	Solar incidence angle	Degrees
$L\lambda$	Spectral radiance for band λ	W/m^2/sr/μm
Ψh	Stability correction for heat transport	-
ψm	Stability correction for momentum transport	-
σ	Stefan-Boltzmann constant	5.67×10^{-8} W/m^2/K^4
α	Surface albedo	-
SEBAL	Surface Energy Balance Algorithm for Land	
SEBI	Surface Energy Balance Index	
SEBS	Surface Energy Balance System	
RCMRD	The Regional Centre for Mapping of Resources for Development	
TM	Thematic Mapper	
TIR	Thermal Infrared	
TOA	Top of Atmosphere	
TSM	Two-Source Models	
UTM	Universal Transverses Mercator	
k	Von Karman’s constant	0.41
$\omega\lambda$	Weighting coefficient for band λ	-
u	Wind velocity	m/s
d	Zero plane displacement	m

Abstract

On land, Evapotranspiration (ET) is a combination of evaporation from the soil surface and transpiration from vegetation and it is one of the climate elements that plays an important role in water cycle and an important parameter in water resources management. As a result, many mathematical equations and algorithms have been developed and designed to compute evapotranspiration by different authors. Estimating from conventional methods of ET, which uses meteorological data, cannot estimate at a larger scale rather at certain location. To overcome this problem, remote sensing are one of the important sources of data and techniques to estimate many climate elements including evapotranspiration. The study area was located in Gilgel Abay catchment Tana sub basin in North West part of Ethiopia. The main objective of this study was estimation of evapotranspiration using SEBAL algorism and Landsat 8 imagery with climate data. In this study, SEBAL based remote sensing technique was applied to estimate spatially as well as temporal distributed evapotranspiration. For this analysis, ASTER GDEM, GRASS-python file & reference weather parameters from Bahir Dar weather station was used. The SEBAL python file was used to calculate the values of all parameters including surface radiance, surface reflectance, surface albedo, NDVI, LAI, surface emissivity, surface temperature, net radiation, soil heat flux, sensible heat flux, latent heat flux, which are consequently used to calculate the hourly and daily evapotranspiration in study area. Based on the analysis the results obtained from pixel wise calculation shows the values of the spatial variation of mean ET for different land cover ranged from 4.42 mm/day for closed grassland to 6.25 mm/day for dense forest areas. While the daily ET varied from 0 mm/day to 7.39 mm/day for the study area and its mean, value was 4.78 mm/day for 23 December 2016. For monthly ET calculation selected months were used and results show the maximum estimated actual evapotranspiration over the whole catchment ranged from 6.51 mm/day (Jan) to 7.82 mm/day (Mar). The mean actual evapotranspiration ranged from 4.37 mm/day (Feb) to 4.78 mm/day (Dec). The seasonal ET also was analyzed using the same approach as daily from Landsat 8 data for selected months and results showed with the mean value of 539.92 mm in 2016.

Keywords: *Gilgel Abay, Landsat-8, remote sensing, evapotranspiration, solar radiation, SEBAL, GRASS-GIS, NDVI, ASTER GDEM*

1. Introduction

1.1. General

Fresh water has become the most precious natural resource and the intelligent management of this resource is one of the biggest challenges. An understanding of natural systems and the physical laws that govern each component of the hydrological cycle is very important for the administrator of water resources. In particular, the evaporation processes of the various land areas that must be understood to achieve sustainable development of our water resources. The irrigation of croplands is an important consumer of water in semi-arid waters and arid regions and an efficient and reliable method to determine the use of water by crops is crucial for proper water management. As it becomes fresh water more scarce, competition for fresh water intensifies and irrigation management will be improved necessary to achieve greater efficiency in the use of this valuable resource (Waters et al., 2002).

In recent years, water resources management has become an important issue. This is especially true with the increased demand and competition for fresh water between different users. Consequently, monitoring the consumption of water has become one of the most popular issues regarding water resources management (FAO, 1993).

Evapotranspiration (ET) is a collective term for all the processes by which water is lost from the soil surface by evaporation and from the plants by transpiration. Both of them evaporation and transpiration occur simultaneously and there is no easy way to separating the two processes (Dingman, 2002). Real evapotranspiration is an indicator of the amount of water that crops and trees need for healthy growth and productivity. Apart from the availability of water on the evaporation surface, several other factors affect the evapotranspiration process. These factors include meteorological parameters such as solar radiation, air temperature, humidity and wind speed.

In addition, the type and density of the vegetation cover, the depth of rooting and the reflection characteristics of the earth's surface are also important factors that must be taken into account. A quantitative understanding of evapotranspiration is of great importance in the study of the water balance of the basin in such a way that first, over a period of time, the difference between precipitation and evapotranspiration is the water available for its use.

Secondly, most of the food supply is grown on irrigated land and the knowledge of real ET helps the efficient use of water without the loss necessary for the growth of the plant (Ayoub, 2009).

The ability to predict ET levels would be a valuable asset for water resource managers. ET is a good indicator of the effectiveness of irrigation and the total water consumption of vegetation. Evapotranspiration information is useful for irrigation supply planning, regulation of water rights and watershed studies (Waters et al., 2002). The major advantage of applying remote sensing is the water consumed as ET can be derived directly without needing for quantifying other complex hydrological processes (Trezza et al., 2013). The importance of ET in predicting soil water availability, flood forecasting, rainfall forecasting and projecting changes in occurring heat waves and droughts also referred in (Merlin, et al., 2014).

This satellite based evaporation estimation is implemented in the lower catchment of Gilgel Abay, Lake Tana sub-basin. The catchment contributes much of the water into the Lake Tana. Consequently, the evapotranspiration estimation is vital from the perspective of accurate water balance study of the Lake Tana and water resources planning in the catchment.

1.2. Statement of the Problem

It is known that agriculture is the backbone of our economy. Therefore, to maximize agricultural production for domestic use and to complement the industry's leading economy, irrigation is the non-alternative option. Therefore, it will help rain-fed agriculture and mitigate the impact of recurrent draft in the country. This can be achieved by working together with the community, local and international NGOs and government organizations to use all available resources efficiently and achieve meaningful change.

Gilgel Abay Diversion Irrigation Project is designed based on the client’s requirement to address the beneficiaries demand. It is believed that this irrigation project will change the living standard of that society. Technical, environmental and socio economic issues are well addressed by the respective disciplinary. The river is flowing in gentle slope with destabilized and confined natural channel. The project is proposed to irrigate 3,264 ha of land with two crops growing on the same field during the same year. Beside to this some part of Koga irrigation project is included in this study area. Hence, knowledge and quantification of surface energy fluxes in this area is important for many purposes to be practiced. However, the evaporation flux was estimated only through hydrological models. Thus, the estimation of evapotranspiration using remote sensing based approaches are largely unexplored research in the catchment.

Wise use of limited water resource, reliable maps of surface energy fluxes for assessing surface atmosphere interaction and knowledge & proper quantification of evapotranspiration are important for maximizing production through irrigation management practices.

1.3. Objective

1.3.1. General objective

The main objective of this study is to estimate evapotranspiration using Surface Energy Balance Algorism for Land /SEBAL/ in the Lower Gilgel Abay catchment, Tana sub-basin, Ethiopia.

1.3.2. Specific objectives

To achieve this main objective the following specific objectives were accomplished.

- To estimate the reference evapotranspiration from ground based meteorological data using **RefET** software
- To quantify evapotranspiration for the classified land use in the catchment
- To investigate the seasonal variation of evapotranspiration in the catchment
- To compare the SEBAL based evapotranspiration estimation with empirical model

1.4. Research Questions

This research questions mainly addressed on

- ➢ How does ET vary spatially and temporally over the Lower Gilgel Abay catchment?
- ➢ How remote sensing estimation be used to improve or substitute ground based measurements of ET?
- ➢ How ET estimate for large land surface areas using minimal amount of ground data?
- ➢ How land use type affect ET?

2. Literature Review

2.1. Overview of Evaporation Process

Evaporation is the process by which liquid water is converted into water vapour (vaporization) and removed from the evaporation surface (vapour elimination). Water evaporates from a variety of surfaces, such as lakes, rivers, pavements, soils and wet vegetation. Energy is required to change the state of water molecules from liquid to vapour. Direct solar radiation and, to a lesser extent, the ambient temperature of the air provide this energy. The driving force to remove water vapour from the evaporation surface is the difference between the vapour pressure of water at the evaporation surface and that of the surrounding atmosphere. As evaporation progresses, the surrounding air gradually becomes saturated and the process slows down and could stop if the humid air is not transferred to the atmosphere. The substitution of saturated air for drier air depends largely on wind speed. Therefore, solar radiation, air temperature, air humidity and wind speed are climatological parameters to consider when evaluating the evaporation process. Where, the evaporation surface is the surface of the soil, the degree of shading of the canopy of the crop and the amount of water available on the evaporation surface are other factors that affect the evaporation process. Frequent rains, irrigation and water carried upwards in a ground of a shallow water table wet the surface of the soil. Where the soil is capable of supplying water fast enough to satisfy the demand for evaporation, the evaporation of the soil is determined only by weather conditions. However, when the interval between rainfall and irrigation becomes large and the soil capacity to drive moisture near the surface is small, the water content in the upper layer of soil falls and the soil surface dries. In these circumstances, the limited availability of water exerts a controlling influence on the evaporation of the soil. In the absence of water supply to the soil surface, evaporation decreases rapidly and can cease almost completely in a few days (Allen et al., 1990).

The transpiration consists of the vaporization of the liquid water contained in the tissues of the plant and the elimination of vapour into the atmosphere. The crops predominantly lose their water through the stomata. These are small openings in the leaf of the plant through which gases and water vapour pass. The water, along with some nutrients, is absorbed by the roots and transported through the plant. Vaporization occurs within the sheet, specifically in the intercellular spaces, and the exchange of steam with the atmosphere is controlled by the stomatal opening. Almost all the water absorbed is lost by perspiration and only a small fraction is used inside the plant. Like direct evaporation, transpiration depends on the energy supply, the vapour pressure gradient and the wind. Therefore, radiation, air temperature, air humidity and wind terms should be considered when assessing transpiration. The water content of the soil and the capacity of the soil to drive the water to the roots also determine the rate of transpiration, as does the water logging and salinity of the soil water. The transpiration rate is also influenced by crop characteristics, environmental aspects and cultivation practices. Different types of plants can have different rates of perspiration. Not only the type of crop must be considered, but also the development of the crop, the environment and the management when evaluating the transpiration (Allen et al., 1990).

Reference evapotranspiration (ET_o) is defined as the rate at which readily available soil water is vaporized from specified vegetated surfaces (Jensen et al., 1990). Then, the reference evapotranspiration is defined as the ET rate of a dense and actively growing uniform surface of vegetation with a specified height and surface resistance, not lower than ground water and representing an extension of at least 100 m equal or similar vegetation (Allen, et al., 2005). The concept of ETo was introduced to study the evaporative demand of the atmosphere independent of the type of crop, crop development and management practices. Relating ET to a specific surface provides a reference on which ET of other surfaces can be related (Allen et al., 1990).

The only factors that affect ETo are the climatic parameters. Consequently, ETo is a climatic parameter and can be calculated from meteorological data. ETo expresses the evaporation power of the atmosphere in a specific place and time of year and does not take into account the characteristics of the crop or the soil factors. The FAO Penman-Monteith method is recommended as the only method to determine ETo. The method has been selected because it closely approximates the grass ETo at the evaluated location, is physically based and explicitly incorporates physiological and aerodynamic parameters. In addition, procedures have been developed to estimate missing climatic parameters (Allen et al., 1990).

Worldwide, evapotranspiration is maximum near the equator and minimum at the poles. This has a similar pattern with the amount of radiation and solar temperature which are the main bypass forces for the phase change (liquid/solid to gas) in respective areas on an annual basis (Dingman,2002). Approximately 62% (72,000 km^3/year) of precipitation falls on the surface of the globally evapotranspired earth (Dingman, 2002). This fraction increased to 85% for the African continent, where arid and semi-arid areas predominate. Of the total ET of the continents, around 97% is lost through the evapotranspiration of the terrestrial surface and the rest 3% is lost from the open water surfaces (Dingman, 2002) cited on Temesgen (2009).

With increasing attention to the elements of climate and climate changes and their effects on the environment and ecological systems, the estimation of evapotranspiration is also increased, especially with the emergence of several measurement techniques for the evaluation of climatic elements. Recently, remote sensing becomes one of the valuable sources of data and analysis techniques to implement such studies. The precise estimation of evapotranspiration is considered the key factor in water management (Bashir et al., 2006). ET (Evapotranspiration) is a climatic element that is an important factor for the cycles of energy, hydrology, carbon and nutrients and a key element of the water balance in the continuous soil-vegetation-atmosphere (Spiliotopoulos et al., 2013).

The precise estimation of evapotranspiration (ET) plays an important role in the quantification of the water balance at the level of basin, river basin and regional scale for better planning and management of water resources. The precise quantification of ET in irrigated agriculture is crucial to optimize crop production, water distribution planning, irrigation management, assessment of the effects of land use change on water yields, development of best practices of management to minimize the degradation of surface and groundwater and assessment of land use and practices of water resources management and environmental quality (Irmak et al., 2006a; 2006b). There are several methods available for ET estimation: Bowen energy balance (BREBS) systems, swirl correlation systems (ECS), weighing lysimeters and water balance techniques offer powerful alternatives for measuring ET and other energy flows on the surface. Despite the elegance, high precision and theoretical attractions of these techniques for measuring ET, their practical use in large areas can be limited. The application of ET mapping from satellite measurements can be an expansion of field measurements using the aforementioned techniques when properly applied and can overcome the aforementioned limitations.

The major advantage of remote sensing is that ET can be computed without quantifying other complex hydrological processes. ET is highly variable in both space and time. It is variable in space due to the wide spatial variability of precipitation, hydraulic characteristics of soils, and vegetation types and densities. It is variable in time due to variability of climate. Satellite images provide an excellent means for determining and mapping the spatial and temporal structure of ET.

2.2. Surface Energy Balance Models

Today, much research has been carried out to collect spatially distributed ETs at large scales through the use of surface energy balance and remote sensing data. These techniques provide spatial information of the earth's surface by measuring the reflected and emitted electromagnetic radiation. The measurements of the infrared, infrared and visible thermal bands of remote sensing data are the inputs for the parameterization of the components of the energy balance in the ET calculation (Hailegiorgis, 2006).

There are different models developed for the estimation of ET from remote sensing data. SEBS (Su, 2002), SEBAL (Bastiaanssen et al., 1998), and TSEB (Norman et al., 1995) are few among many other algorithms. The remote sensing methods allow estimation of energy fluxes even for inaccessible areas.

2.2.1. Surface Energy Balance Index (SEBI)

Based on the contrast between dry and wet regions Choudhury & Menenti (1993) proposed the Surface Energy Balance Index (SEBI) method to derive the evapotranspiration from evaporative fraction. This method is based on the Crop Water Stress Index (CWSI) (Jackson et al., 1981). In this approach, relative evaporation is determined by scaling an observed surface temperature in a maximum range of surface temperature, denoted by extremes in the surface energy balance suggesting a theoretical lower and upper bounds on the surface and air temperature difference. Here under dry-condition, evaporation is assumed to be zero due to the limitation of water availability in soil for a particular set of boundary layer characteristics so that the sensible heat flux density takes its maximum value Ts,max (maximum surface temperature). The minimum surface temperature is obtained for the wet region by computing the potential ET from the Penman-Monteith equation considering zero internal resistance (Yuei-An & Sanjib, 2014).

Interpolating the observed surface temperature with the maximum and minimum surface temperatures, the relative evaporative fraction can then be calculated. Modifying the CWSI, Choudhury & Menenti (1993 defined theoretically the pixel-wise ranges for latent heat flux and surface temperature (Ts) to account for surface variability of actual evaporation caused by albedo and aerodynamic roughness. For a surface at particular surface albedo and roughness, pixel-wise maximum and minimum surface temperatures and redefined CWSI as a pixel-wise SEBI are computed to derive the regional ET from the relative evaporative fraction.

2.2.2. Surface Energy Balance System (SEBS)

Another well-known model is the Surface Energy Balance System (SEBS). (Su, 2001; 2002) and (Su, et al., 2003; 2005) described a modified form of SEBI for the estimation of land surface energy balance using remotely sensed data, which has been named SEBS. SEBS estimates sensible and latent heat fluxes from satellite data and routinely available meteorological data. Computations of land surface physical parameters, calculation of roughness length for heat transfer, and estimation of the evaporative fraction based on energy balance at limiting cases are the main bases of SEBS (Choudhury, 1989). In SEBS, the latent heat flux is considered to be zero at the dry limit, which means sensible heat flux reaches its maximum value (Yuei-An & Sanjib, 2014). On the other hand, at the wet limit, ET takes place at potential rate (LE_{wet}), (*i.e.*, the evaporation is restricted only by the energy available for a particular surface and atmospheric condition) and the sensible heat flux attains its minimum value, H_{wet}. Remote sensing data-derived land parameters and ground-based meteorological measurements are used as inputs in SEBS.

SEBS can be even used for both local and regional scaling under all atmospheric stability regimes (Su, 2002). Accuracy of ET value estimated from SEBS could reach 10 - 15% of that of in-situ measurements. Main advantages of the SEBS include:

I. Consideration of the energy balance at the limiting cases, which minimizes the uncertainty involved in surface temperature or meteorological variables;
II. New formulation of the roughness height for heat transfer instead of using constant values;
III. Characterizing actual turbulent heat fluxes without any prior knowledge; and
IV. Representativeness of parameters associated with surface resistance.

Note that SEBS has been widely applied over large heterogeneous areas fed with MODIS data with thermal band information of 1 km (McCabe & Wood, 2006; Gao & Long, 2008). However, relatively complex solution of the turbulent heat fluxes and too many required parameters can often cause more or less inconveniences in SEBS when data are not readily available.

2.2.3. Simplified Surface Energy Balance Index (S-SEBI)

A simplified new method derived from SEBI, called Simplified Surface Energy Balance Index (S-SEBI), has been developed to estimate the surface flux from remote sensing data (Roerink et al., 2000). Contrast between a reflectance (albedo) dependent maximum and minimum surface temperature for dry and wet conditions, respectively, is a main base of this method to partition available energy into sensible and latent heat fluxes. No additional meteorological data is needed if the surface extremes are available on the scene studied. By assuming steady global radiation and air temperature, a physical explanation to the observed surface reflectance and temperature in the S-SEBI approach can be given when surface characteristics within the observed image changes between dark/wet and dry/bright pixels. Here, evaporative fraction (EF) is constrained by the dry and wet regions and formulated by interpolating the reflection-dependent surface temperature between the reflection-dependent maximum and minimum surface temperatures (Yuei-An & Sanjib, 2014). The major advantages of S-SEBI are:

I. Additional ground-based measurement is not needed to derive the EF except the surface temperature and reflectance (albedo) derived from remote sensing data if the surface extremes are present in the remotely sensed imagery; and
II. Extreme temperatures for the wet and dry conditions vary with changing reflectance (albedo) values, but in other methods like SEBAL, a fixed temperature is determined for wet and dry conditions.

2.2.4. Mapping Evapotranspiration at High Resolution and with Internalized Calibration (METRIC)

Mapping evapotranspiration at high Resolution with Internalized Calibration (METRIC) is a variant of SEBAL, an energy balance model developed in the Netherlands. It is also an image-processing tool for mapping regional ET over more complicated surfaces as a residual of the energy balance at the Earth’s surface. METRIC has been extended from SEBAL through integration with reference ET, which is computed using ground-based weather data. The fundamental principle underlying METRIC is that evaporating liquid drops absorbs heat as indicated by Allen et al., (2005; 2007) to derive ET from remotely sensed data in visible, near-infrared, and thermal infrared spectral regions along with ground-based measurements of wind speed and near-surface dew point temperature. Two anchor conditions are selected within an observed scene to internally calibrate the sensible and latent heat flux computation and to fix boundary conditions for the energy balance. Once surface temperature, *Ts*, and d*T* are calculated corresponding to hot and cold conditions, the linear relationship is defined. However, the context-dependency of SEBAL, METRIC, and triangular models has been indicated in a recently conducted study (Long & Singh, 2013) cited on (Yuei-An & Sanjib, 2014).

2.2.5. Two-Source Models (TSM)

Norman et al. (1995) proposed a new model named two-source model, also known as duel-source model to improve the accuracy of LE estimates using satellite remote sensing data, especially over sparse surfaces. The basic principle of this model is to partitioning the composite radiometric surface temperature into soil and vegetation components, and considered sensible and latent heat fluxes are transferred to the atmosphere from both surface components. In the duel source, model, satellite-derived surface temperature (*Ts*) is considered a composition of the soil (*Tsoil*) and canopy temperatures (*Tveg*), and *H* and *LE* are divided into soil and vegetation contributions, respectively. Both the one- and Two-source models are sensitive to their use of the temperature differences to estimate H cited on (Yuei-An & Sanjib, 2014).

The TSM model requires micrometeorological measurements of air temperature, humidity, atmospheric pressure, wind speed, solar radiation, and remote sensing derived inputs of land use and normalized difference vegetation index (NDVI). The land surface was considered to be a composition of soil and vegetation and the partitioning of heat and water vapour fluxes were conducted differently for each source.

2.2.6. Surface Energy Balance Algorithm for Land (SEBAL)

Surface Energy Balance Algorithm for Land (SEBAL), an image-processing model for calculating evapotranspiration (ET) as a residual of the surface energy balance. It is used for estimating various land surface parameters i.e., surface albedo, surface temperature, and energy balance parameters, from different spatial, spectral and radiometric resolutions of satellite data.

Most current operational models such as (SEBAL, and deterministic methods generally are based on more complex models such as Soil Vegetation Atmosphere Transfer (SVAT) models), which calculate the different components of the energy budget. Many methods and models are designed for estimating the evapotranspiration using remote sensing data. SEBAL is an ET estimation approach based on satellite images via computing a land surface energy balance. The SEBAL algorithm is developed by (Bastiaanssen, et al., 1998). The model represents the most promising algorithm that needed minimum input data of ground based variables and it has been widely applied abroad the world accurately to estimate actual ET (Bashir, et al., 2006).

SEBAL method uses multispectral remote sensing data associated with complementary meteorological data to estimate instantaneous surface energy balance components (Ruhoff, et al., 2012). (Bastiaanssen, et al., 2005) proved the importance of SEBAL method in establishing a variety of measurements and assessments, including land use and water use for river basin planning, impact of water conservation, environmental impact assessment, hydrological modelling and more other application (Bastiaanssen, et al., 2005).

SEBAL requires minimum ground based measurements; equipped with automatic internal calibration and exact atmospheric corrections are not required.

2.3. SEBAL based previous evapotranspiration studies

Timmermans and Meijerink (1999) applied sequential Landsat TM and NOAA-AVHRR data to determine evapotranspiration losses from the groundwater of an aquifer in Botswana during the dry season. The SEBAL method yielded high actual evapotranspiration (Ea) rates (1.5 to 3 mm/day). No relationship between Ea and depth to water table was found, except in the valleys, where riverine forests are fed by a system of discharging groundwater flow. The patterns on a vegetation map based on a supervised classification using TM data, including thermal bands, showed similarity with the actual evapotranspiration (Ea) patterns. Continuous data on surface temperatures and soil moisture were used from a meteorological tower and field observations for calibration and partial validation of the results during satellite overpasses.

Hafeez et al. (2002) tested the feasibility of using SEBAL with multi sensors data at different processing levels: ASTER L1A, Landsat 7 ETM+ L1G, and MODIS L1B for the different periods of dry season 2001. The Surface Energy Balance Algorithm for Land (SEBAL) has been applied to ASTER (February 02, 2001), Landsat 7 ETM+ (April 16, 2001), and MODIS (May 18, 2001) sensors for the estimation of evapotranspiration in the District 1 of the Upper Pumapanga River Integrated Irrigation System (UPRIIS), in Central Luzon, of Philippine. Actual evapotranspiration was computed during satellite overpass and integrated for 24-hours on pixel-by-pixel basis. The inter-relationship of ASTER and Landsat images with the Modis images for the water consumption studies in District 1 showed unique combination. The result showed non-significant variation compared with the evapotranspiration calculations at two meteorological stations in District 1 and found close relationship with daily evapotranspiration estimated by different sensors as predicted by SEBAL.

Tasumi et al. (2005) have been applied SEBAL and METRIC remote sensing energy-balance based evapotranspiration (ET) models in the western United States. ET predicted by the models was compared to lysimeter-measured ET in agricultural settings in the semi-arid climates. These results imply that the SEBAL/METRIC remote sensing models have a high potential for successful ET estimation in the semi-arid United States.

Zwart et al. (2006) evaluate the use of water for good management practices. A methodology has been developed to quantify spatial variation of crop yield, evapotranspiration (ET) and water productivity (WPET) using the SEBAL algorithm and high and low resolution satellite images. SEBAL estimated ET was validated over a wheat dominated area in the Yaqui Valley, Mexico and proved to be accurate.

Kimura et al. (2007) targeted the water balance, especially regarding evapo-transpiration (ET), over the river basin in the northeastern Loess Plateau of China. For ET estimation, an algorithm referring to the SEBAL method based on remote sensing was outlined and validated with the observation result over natural grassland. ET by land-use difference and the spatial distribution of ET over the river basin were examined using the algorithm.

Compaoré et al. (2008) used SEBAL to map evaporation in the White Volta Basin of Ghana, West Africa, at the start and at the end of the dry season using Landsat and MODIS images. The results obtained from this study demonstrate that SEBAL is an accurate algorithm for mapping evaporation over tropical areas where few or no ground measurements are available using common satellite products such as Landsat and MODIS.

Almhab and Busu (2008) modified SEBAL model using data from Landsat TM and NOAA-AVHRR sensors, has been used to estimate net radiation, soil heat flux, sensible heat flux and ET for Sana 'a Basin in Yemen. Actual ET was computed during satellite overpass and integrated for 24-hr on pixel-by-pixel basis for daily ET distribution. As a result, a daily ET map generated from meteorological observation was compared with estimated ET data simulated from remote sensing data. In conclusion, data from both remote sensing give reasonable values with result from TM are better compare to those of AVHRR due to difference in spatial resolution, which TM data a higher spatial resolution than AVHRR.

Hong et al. (2009) used to derive ET maps from Landsat 7 and MODIS images using SEBAL. Evaluations were conducted for both "output" and "input" up-scaling procedures, with aggregation accomplished by both simple averaging and nearest neighboring resampling techniques. They conclude that good agreement exists between SEBAL estimated ET maps directly derived from Landsat 7 and MODIS images. Overall, the daily ET maps over the Middle Rio Grande Basin aggregated from Landsat images were in good agreement with ET maps directly derived from MODIS images.

Wang et al. (2009) had programmed and validated a remote sensing ET model based on SEBAL against eddy covariance data. A sensitivity analysis was conducted for full, half, and sparse canopy cover in pecan orchards. At all the three degrees of canopy cover, estimated ET changed by 40% to 270% (1 to 2 mm/day) when either variable changed from its baseline value by ±50% of the permissible range. Estimated ET was also sensitive to the selection of the wet (full ET) reference pixel and to dT (aerodynamic difference of air and land temperatures). Changes in ET estimates were 47% to 72% (1.3 to 3.7 mm/day) at both the full and half canopy areas under changes from baseline values equal to 50% of the permissible range for either variable. In addition, ET was sensitive to the roughness length in areas of half canopy cover (ET changed by 61% [1.5 mm/day]) and to the value of the normalized difference vegetation index (NDVI) in areas of sparse canopy cover (ET changed by 118% [0.35 mm/day]). Thus, they have indicated future research on ET algorithm improvement should focus on the above variables and relative equations. The selection of the wet and dry spots/anchors/ should be automated to avoid subjective errors from manual selection.

Hamimed et al. (2009) assessed the actual daily evapotranspiration for Ksar Chellala plains in Algeria. from satellite ASTER data using SEBAL. Net radiation, soil heat flux and sensible heat flux at each pixel and estimates the latent heat flux as the residual term in the energy balance using an input of NDVI, surface temperature and albedo.

Sun et al. (2011) developed a scheme to assess actual evapotranspiration (ETa) across a range of land uses in Nansi Lake Wetland, China, using a remote sensing technique and SEBAL model. The estimation of pixelscaled ETa was conducted via SEBAL using Landsat-7 images, DEM and meteorological data. Compared with the recorded pan evaporation, the estimated evapotranspiration calculated by SEBAL agreed well with the results derived from pan observations. Then, the spatial distribution characteristic of daily evapotranspiration was analyzed by referencing the land-use map and found that the open water body and creed swamp were at a high evapotranspiration rate, while the crop land, grassland and rural residential land took the second place, and the overflow land, town constructed land and bare soil were at the lowest evapotranspiration rate, which accorded with the evapotranspiration theory.

Allen et al. (2011) calculate evapotranspiration (ET) as a residual of a surface energy balance from SEBAL and METRIC models. Both models are calibrated using inverse modelling. The primary inputs for the models are short-wave and long-wave (thermal) images from satellite (e.g. Landsat and MODIS); a digital elevation model and ground-based weather data measured within or near the area of interest. ET ‘maps’ (i.e. images) developed using Landsat images provide means to quantify ET on a field basis in terms of both rate and spatial distribution. SEBAL and METRIC have advantages over conventional methods of estimating ET using crop coefficient curves or vegetation indices in that specific crop or vegetation type does not need to be known and the energy balance can detect reduced ET caused by water shortage; salinity or frost as well as evaporation from bare soil.

Ruhoff et al. (2012) evaluate the accuracy of the SEBAL algorithm for estimating surface turbulent heat fluxes at regional scale. SEBAL estimates are compared with eddy-covariance (EC) measurements and results from the hydrological model MGB-IPH. SEBAL instantaneous estimates of latent heat flux (LE) yielded r^2= 0.64 and r^2 = 0.62 over sugarcane croplands and savannas when compared against in situ EC estimates. At the same sites, daily aggregated estimates of LE were r^2 = 0.76 and r^2 = 0.66, respectively. Average daily ET from SEBAL is in close agreement with estimates from the hydrological model for an overlay of 38,100 km^2 (r^2 = 0.88). Inputs to which the algorithm is most sensitive are vegetation index (NDVI), gradient of temperature (dT) to compute sensible heat flux (H) and net radiation (Rn). It was verified that SEBAL has a tendency to overestimate results both at local and regional scales probably because of low sensitivity to soil moisture and water stress. Nevertheless, the results confirm the potential of the SEBAL algorithm, when used with MODIS images for estimating instantaneous LE and daily ET from large areas.

Yang et al. (2012) to deal with water resources crisis caused by climate change and intensified human activities, the Hetao Irrigation District of Inner Mongolia in North China and its impact on regional hydrological cycle and thus water use patterns over different land use types SEBAL model fed with MODIS data was applied in Hetao area from 2000 to 2010 to examine the spatial and temporal patterns of evapotranspiration (ET). The results indicate that inter-annual variability in ET over agricultural land, water body, woodland and irrigated grassland are primarily explained by the variation of reference ET. So it is with the seasonal variability in agricultural land ET on monthly basis.

Spiliotopoulos et al. (2013) used to derive daily actual evapotranspiration (ETa) distributions from Landsat and MODIS images separately using SEBAL model in Lake Karla basin in Thessaly, Central Greece. Meteorological data have also been used. The results are satisfactory, giving the general trend of ETa derived from the original SEBAL procedure.

Li et al. (2013) retrieved ET and the energy fluxes with Landsat 5 remote sensing images of the area in the summer of 2006 using SEBAL model for Yellow River in the eastern of Tibetan Plateau for different land use types. It was estimated that the instantaneous evapotranspiration was highest in middle-and-high coverage grassland of the southern region at 0.31 mm/h on average level, and lowest in bare soil of the northern region at 0.13 mm/h on average level.

Al Zayed et al. (2016) evaluated three methods, namely SEBAL, METRIC, and SSEB, were applied using Landsat images for estimating ET over the large-scale Gezira Scheme of Sudan. The ET methods were validated using field-scale water balance (WB) estimates during the 2004 crop season. Furthermore, the present study suggested the use of Normalized Difference Vegetation Index (NDVI) and integrated NDVI (iNDVI) as an approach to assessing the performance of the ET estimates from RS on daily and seasonal scales, respectively. Several performance measures were evaluated, and a score was given for each method in order to extract the most valuable information. Based on ranking criteria, SSEB gave the best performance followed by SEBAL. METRIC is not suitable for estimating ET where ground-data are limited. All methods showed similar spatial patterns of seasonal ET, SSEB has the advantage of estimating ET on field scale and on daily basis. The results of this study contribute to improving the understanding of performance of such methods in large irrigation schemes in arid climate zones.

Jaber et al. (2016) evaluate the SEBAL model for actual Evapotranspiration estimation in Al-babil city in Iraq using a SEBAL toolbox developed for ArcGIS software. The toolbox was evaluated with two reference actual Evapotranspiration datasets from Al-babil meteorological stations. Overall accuracy of ($R^2 = 0.86$) for the first dataset on March and ($R^2 = 0.85$) for the second dataset on September were achieved. The result of this research indicates that the SEBAL model is effective for estimating actual evapotranspiration in the studied area.

The main advantage of SEBAL model over other remote sensing methods is that it requires minimum ground data and can accurately measure seasonal or annual ET. The accuracy can be 85% on a daily basis and 95% on a seasonal basis (Bastiaanssen, et al., 2005).

Besides its several advantages, it has several drawbacks as well sited as Yuei-An & Sanjib, (2014). Major disadvantages of this method are:

- Subjective specifications of representative hot/dry and wet/cool pixels within the image are required to determine model parameters a and b. The resulting H flux and ET estimates from SEBAL can vary with differing extreme pixels selected by the operator, domain size, and spatial resolution of satellite sensors;
- Over mountainous regions, some adjustments are required based on a digital elevation model for Ts and u to account for the lapse rate;
- Estimated H is greatly affected by the errors in surface-air temperature differences or surface temperatures measurements; and
- Ignoring the effect of radiometer viewing angle, can cause variation in Ts by several degrees for some images.

2.4. Overview-how SEBAL computes evapotranspiration (ET)

In the SEBAL model, ET is computed from satellite images and weather data using the surface energy balance as illustrated in-Figure 2.1. Since the satellite image provides information for the overpass time only, SEBAL computes an instantaneous ET flux for the image time. The ET flux is calculated for each pixel of the image as a "residual" of the surface energy budget equation.

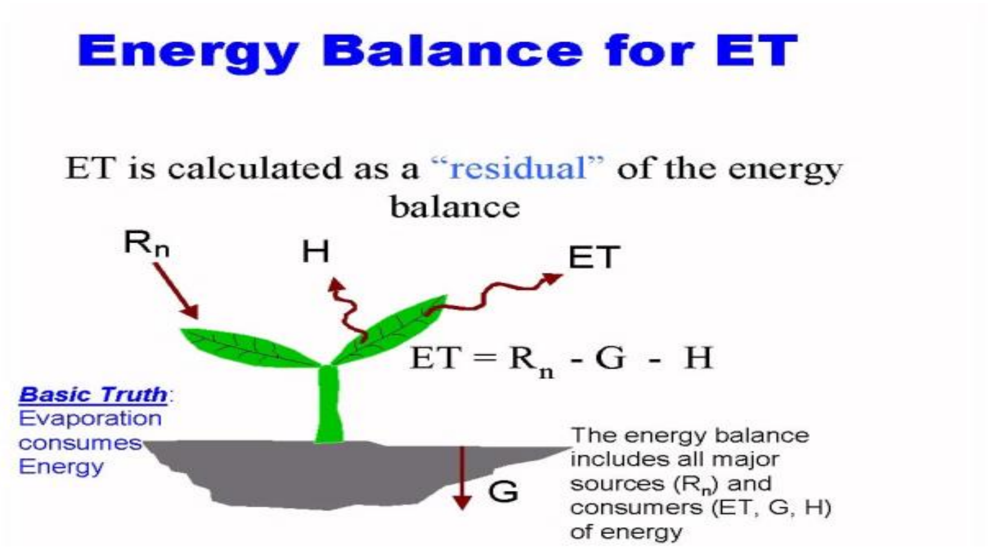

Figure 2.1: Surface Energy Balance (Source: SEBAL Training manual, 2002)

Surface Energy Balance Algorithm for Land (SEBAL), an image-processing model for calculating evapotranspiration (ET) as a residual of the surface energy balance, was developed in the Netherlands by Bastiaanssen, et al., (1998). Within the most promising approaches currently available to estimate evapotranspiration, the SEBAL has been designed to calculate the energy balance components, at both local and regional scales with minimum ground data. This model is an intermediate approach using both empirical relationships and physical parameterization. It requires digital imagery data collected by any satellite sensor measuring visible, near infrared, and thermal infrared radiation, Ts, NDVI, and albedo maps. Latent heat flux (LE) is estimated as a residual of the energy balance equation on a pixel-by-pixel basis. Net radiation (Rn) is computed from the balance of short and longwave radiations. Soil heat flux (G) is calculated utilizing the equation proposed by Bastiaanssen (2000) which is applicable to all sorts of vegetation cover and soil type. Under several climatic conditions, this method has been verified at both field and catchment scales with typical accuracy at field scale being 85% and 95% at daily and seasonal scales, respectively, in more than 30 countries worldwide (Bastiaanssen, et al., 2000; 2005). The estimation of sensible heat flux (H) is required to obtain the parameters that will allow the computation of ET as a residual from the energy balance. In SEBAL, two reference air temperatures are taken. One being an air temperature located at height (h1) close to the surface and the other at an upper height (h2). To determine the value of dT for each pixel, SEBAL assumes the existence of a linear relationship between dT and the radiometric surface temperature Ts considering homogeneous meteorological and surface conditions. The surface temperature, however, needs to be adjusted to a common reference elevation for accurate prediction of dT. Otherwise, high elevations that appear to be "cool" may be misinterpreted as having high ET. Therefore, in the Mountain Model, a "lapsed" (artificial) surface temperature map is created for purposes of computing dT by assuming that the rate of decrease in surface temperature due to elevation increase is the same as that for a typical air profile. The elevation data is provided by the DEM. This "artificial" lapse-adjusted surface temperature is referred to as a DEM corrected surface temperature (Ts-dem).

Generally, air temperature decreases 6.5 ^{0}C for each 1 km elevation increase under neutral stability conditions. Since surface temperatures are in strong equilibrium with air temperature, one can usually observe similar decreases in surface temperature.

The net radiation flux at the surface (Rn) represents the actual radiant energy available at the surface. It is computed by subtracting all outgoing radiant fluxes from all incoming radiant fluxes Figure 2.2.

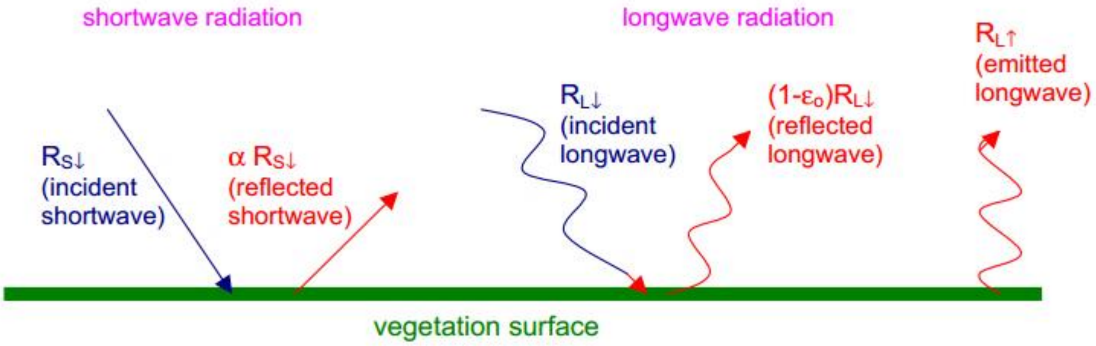

Figure 2.2: Surface Radiation Balance (Source: SEBAL Training manual, 2002)

The amount of shortwave radiation (Rs↓) that remains available at the surface is a function of the surface albedo (α). Surface albedo is a reflection coefficient defined as the ratio of the reflected radiant flux to the incident radiant flux over the solar spectrum. It is calculated using satellite image information on spectral radiance for each satellite band. The incoming shortwave radiation ($R_S\downarrow$) is computed using the solar constant, the solar incidence angle, a relative earth-sun distance, and a computed atmospheric transmissivity. The incoming longwave radiation ($R_L\downarrow$) is computed using a modified Stefan-Boltzmann equation with atmospheric transmissivity and a selected surface reference temperature. Outgoing longwave radiation ($R_L\uparrow$) is computed using the Stefan-Boltzmann equation with a calculated surface emissivity and surface temperature. Surface temperatures are computed from satellite image information on thermal radiance.

The surface emissivity is the ratio of the actual radiation emitted by a surface to that emitted by a black body at the same surface temperature. In SEBAL, emissivity is computed as a function of a vegetation index. The final term in Equation, $(1-\varepsilon_o)\ R_L\downarrow$, represents the fraction of incoming longwave radiation that is lost from the surface due to reflection.

The soil heat flux (G) and sensible heat flux (H) are subtracted from the net radiation flux at the surface (R_n) to compute the "residual" energy available for evapotranspiration (λET). Soil heat flux is empirically calculated using vegetation indices, surface temperature, and surface albedo. Sensible heat flux is computed using wind speed observations, estimated surface roughness, and surface to air temperature differences. SEBAL uses an iterative process to correct for atmospheric instability due to the buoyancy effects of surface heating.

Once the latent heat flux (λET) is computed for each pixel, an equivalent amount of instantaneous ET (mm/hr) is readily calculated by dividing by the latent heat of vaporization (λ). These values are then extrapolated using a ratio of ET to reference crop ET to obtain daily or seasonal levels of ET. Reference crop ET, termed ET_r, is the ET rate expected from a well-defined surface of full-cover alfalfa or clipped grass and is computed in the SEBAL process using ground weather data.

2.5. Limitation to the application of SEBAL retrieved from remote sensing

Beside its several advantages, it has several drawbacks as well. Major disadvantages of this method are:

i. Subjective specifications of representative hot/dry and wet/cool pixels within the image are required (Long & Singh, 2012; 2013) to determine model parameters a & b. The resulting H flux and ET estimates from SEBAL can vary with differing extreme pixels selected by the operator, domain size, and spatial resolution of satellite sensors (Long, Singh, & Li, 2011),
ii. Over mountainous regions, some adjustments are required based on a digital elevation model for Ts and u to account for the lapse rate (Gao , Long, & Li, 2008),
iii. Availability of cloud free images,
iv. lower temporal frequency but high spatial resolution imagery provided by the satellite,
v. Estimated H is greatly affected by the errors in surface-air temperature differences or surface temperatures measurements; and
vi. Ignoring the effect of radiometer viewing angle, can cause variation in Ts by several degrees for some images.

3. Material and Methods

3.1. Description of the study area

3.1.1. General

The Lake *Tana* Basin is one of the sub basin of Upper Blue Nile (Abay River Basin Integrated Development Master Plans Project, 1999) cited in (Setegn et al., 2009). This sub-basin is located in North-Western Ethiopia (latitude 269408 m and 418595.8 m N, and longitude 1211257.7 m and 1412924.8 m E) with a drainage area of about 15,000 km^2. It is shared by four administrative zones called *Agew Awi*, *North Gondor, South Gondor,* and *West Gojjam.* The Lake *Tana*, the largest lake in Ethiopia and the third largest in the Nile Basin. The climate of the Lake Tana sub-basin is dominated by tropical highland monsoon with most of its rainfall (70-90% of total rainfall) occurring between June and September.

Gilgel Abay, Gumara, Ribb, and Megech are the major rivers feeding the Lake Tana. These rivers contribute more than 93% of the flow. The Gilgel Abay River with a catchment area of 5,004 km^2 is the largest river discharging into the Lake Tana (Dile et al., 2013).

3.1.2. Location of the study area

Lower part of Gilgel Abay catchment is located in the Northwest highlands of Ethiopia between 36.79^0 to 37.27^0 N latitude and 11.35^0 to 11.82^0 E longitudes. The study area (watershed) lays in four administration boundaries (Woredas) namely: Achefer, Dangla,Merawi and Bahir Dar Zuria and it covers (1,743.47 km^2). The Gilgel Abay River is one of the major rivers, which drains into Southern part of Lake Tana and originates from a small spring that is Gish Abay Mountain near Sekela town at elevation of 2900 m a.s.l.

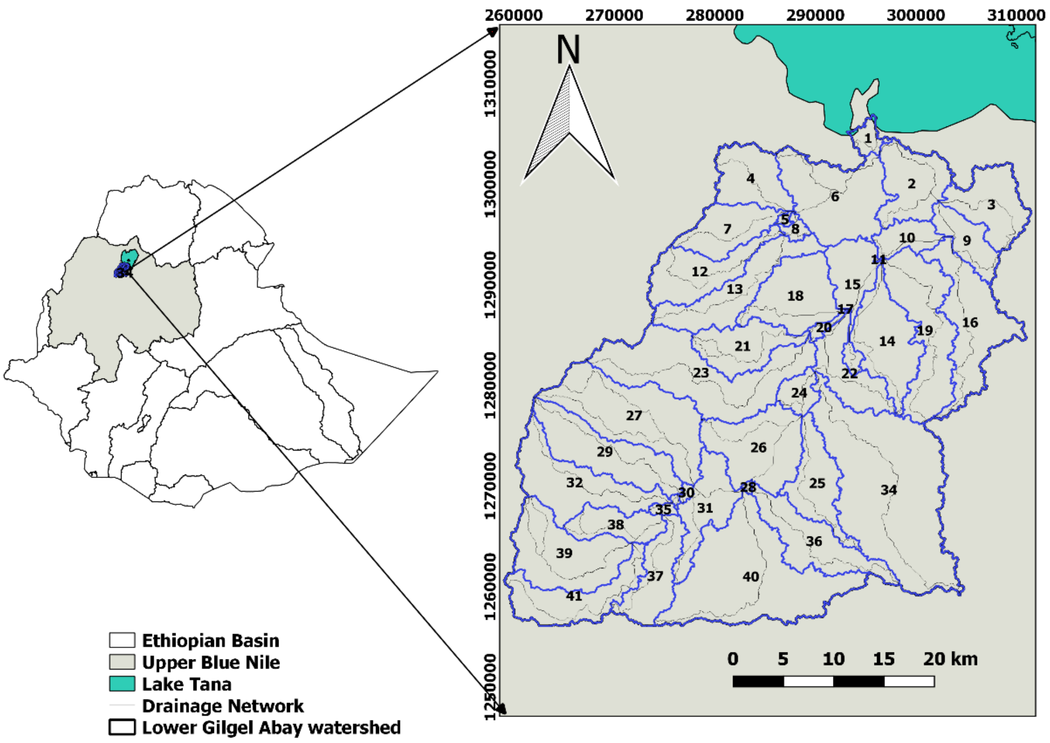

Figure 3.1: Location Map of the Study area

3.1.3. Topography

The elevation of Lower *Gilgel Abay* catchment varies from 1699 to 2667 m a.s.l. from ASTER Global DEM Figure 3.2.

The slope map of the study area was derived from DEM and varies from 0 to 50%. Table 3.1 below states that the catchment area (40.58%, 56.90% and 2.52%) falls in the slope ranges of 0 - 8%, 8 - 30% and >30% respectively following FAO slope classification.

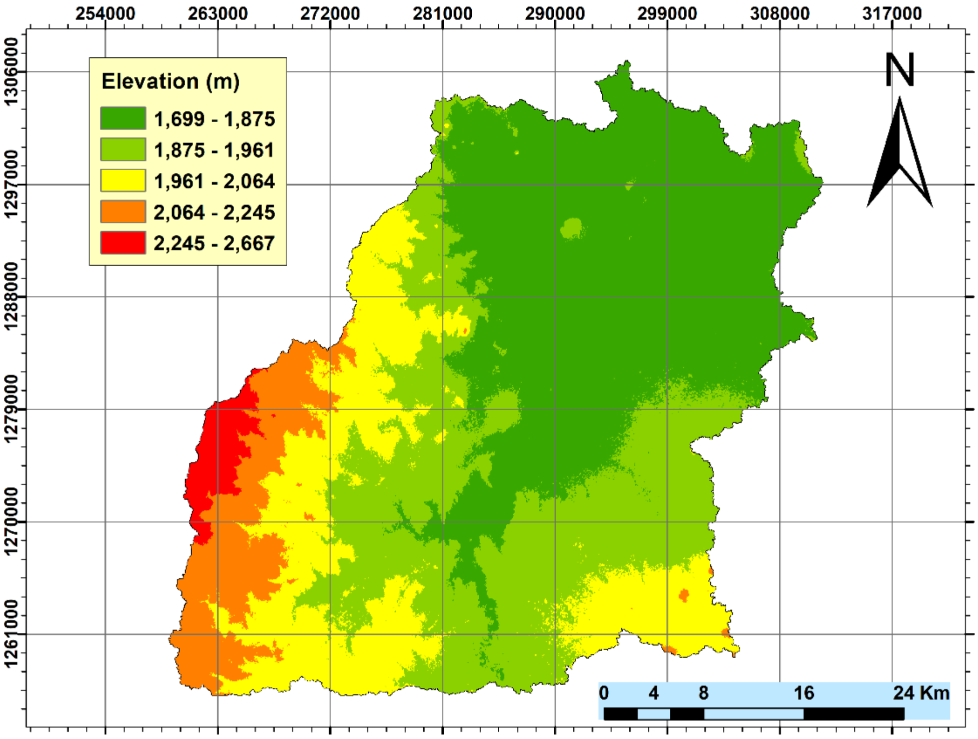

Figure 3.2: Elevation map of the study area

Table 3.1: FAO slope classification of the study area

No	FAO Classification			Covered area (km^2)	Coverage in %
	Slope Range	Description	Code		
1	0 to 2%	Level	LE	64.489	3.70
2	2 to 4%	Very Gentle Sloping	VG	169.012	9.69
3	4 to 8%	Gently sloping	GS	474.028	27.19
4	8 to 16%	Sloping	SL	695.440	39.89
5	16 to 30%	Strongly sloping	SS	296.570	17.01
6	30 to 50%	Moderate steep	MS	38.506	2.21
7	>50%	Very steep	VS	5.423	0.31

3.1.4. Climate of the study area

The climate of Ethiopia is mainly controlled by the seasonal migration of the Inter-Tropical Convergence Zone (ITCZ) and associated atmospheric circulation as well as by the complex topography of the country. It has a diversified climate ranging from semi-arid desert type in the low lands to humid and temperate type in the South-West. Like most of the central highlands, the elevated position of the Gilgel Abay River watershed area makes for a temperate, subtropical, and equable climate despite its proximity to the equator. There are two seasons, rainy and dry. The rainy season has two periods, the little rains, during April and May, and the big rains, which last from mid June to mid September (Getachew, 2014).

The inter-annual oscillation of the surface position of the ITCZ causes variations in the wind flow patterns in Ethiopia (Kebede, 2009). In its oscillation to the North and South of the equator, the ITCZ passes over Ethiopia twice a year and this migration alternatively causes the onset and withdrawals of winds from North and South (EMA, 1981). The catchment receives big rains between June and September when the ITCZ is to the North of Ethiopia, while the small rainy season is usually between March and May. Winds from the Gulf of Eden and maximums of the Indian Ocean attracted towards the centre of Ethiopia. These humid winds from the east and southeast produce small spring rains in the east central part of the North-western highlands (Kahsay, 2004). In general, the annual climate of the study area can be classified as rain (from June to September) and dry seasons (from October to May). There is a large spatial and temporal variation of rainfall in the study area.

The spatial variation in the amount of rainfall in the area indicated a decreasing trend from the south to the north of the catchment area. The long term means the annual precipitation of the study area of the automatic weather station Bahir Dar 950 mm (Kebede, 2009). The temperature in the study area is very influenced by the altitude where the temperature decreases with the increase in altitude. In general, the annual average temperature of the Gilgel Abay basin falls in the range of 16 ^{0}C to 20 ^{0}C (Kebede, 2009). The climate is generally temperate at the highest elevations and tropical at the lowest elevation.

As shown in Figure 3.3, the long term average monthly rainfall (1996 to 2015) from Bahir Dar Automatic weather station (AWS) shows an average of 119 mm/month and the average monthly maximum and minimum temperature of the station 22.90 ^{0}C and 17.60 ^{0}C, respectively.

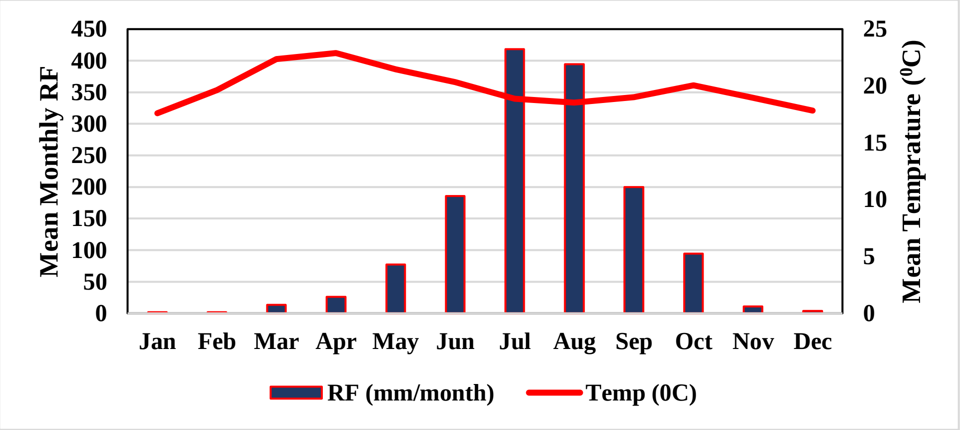

Figure 3.3: Average monthly rainfall (1996-2015) and average temperature (2014-2016) (Source: EMA)

3.1.5. Soil and Geology

The basin is part of the highlands that largely owe their altitude to the rise of the Arab-Ethiopian landmass and the subsequent spillage of basaltic lava that flows during the Tertiary period. This consists of quaternary volcanic rocks that overlap the oldest tertiary rocks of the basin. The volcanic Quaternary is mainly represented by olivine alkaline basalt, often interspersed with clayey palaeosoils. As discussed in SMEC (2007) the volcanic Quaternary comprises vesicular block and fractured basalt, some basaltic breccias and tuffs perhaps as much as 200 - 300 mm thick (Kebede, 2009). As shown in the Table 3.2, most of the catchment /study area/ covered by Basaltic geology type.

Table 3.2: Major Geology and area coverage of the study area (MoWIE 2008)

No	CODE	GEOLOGY	Area (km^2)	Area (%)
1	LAKE	Lake	0.44	0.03
2	QALL	Alluvium	205.57	11.79
3	QCB2	Basalts related to volcanic centre (2)	1235.86	70.89
4	QCB3	Basalts related to volcanic centre (3)	299.29	17.17
5	TABL	Lateriteon Amba Alaji Rhyolite	0.52	0.03
6	TTB2	Termaber Basalts (2)	1.78	0.10

Based on BCEOM, (1998) report, thirteen major soils types in this watershed have been found after clipping the vector format of the soil shape file to the study area. Above 80% of the area is represented by Haplic Luvisols, Chromic Luvisols, Eutric Vertisols and Lithic Leptosols (Table 3.3 and Figure 3.4).

Table 3.3: Major soil group in the watershed (BCEOM, 1998)

No	Group	Majorsoil	Area (km^2)	Area (%)
1	AeFl	Eutric Fluvisols	3.01	0.17
2	ReVr	Eutric Fluvisols	35.71	2.05
3	RhLv	Haplic Luvisols	492.43	28.24
4	RhNT	Haplic Nitisols	64.83	3.72
5	RxLv	Chromic Luvisols	391.65	22.46
6	V/SeLp	Eutric Leptosols	0.31	0.02
7	V/ShLv	Haplic Luvisols	122.07	7.00
8	V/SqLp	Lithic Leptosols	254.29	14.59
9	VeRg	Eutric Regosols	18.68	1.07
10	VeVr	Eutric Vertisols	272.70	15.64
11	VhLv	Haplic Luvisols	39.73	2.28
12	VxLv	Chromic Luvisols	47.63	2.73
13	W	Water	0.44	0.03

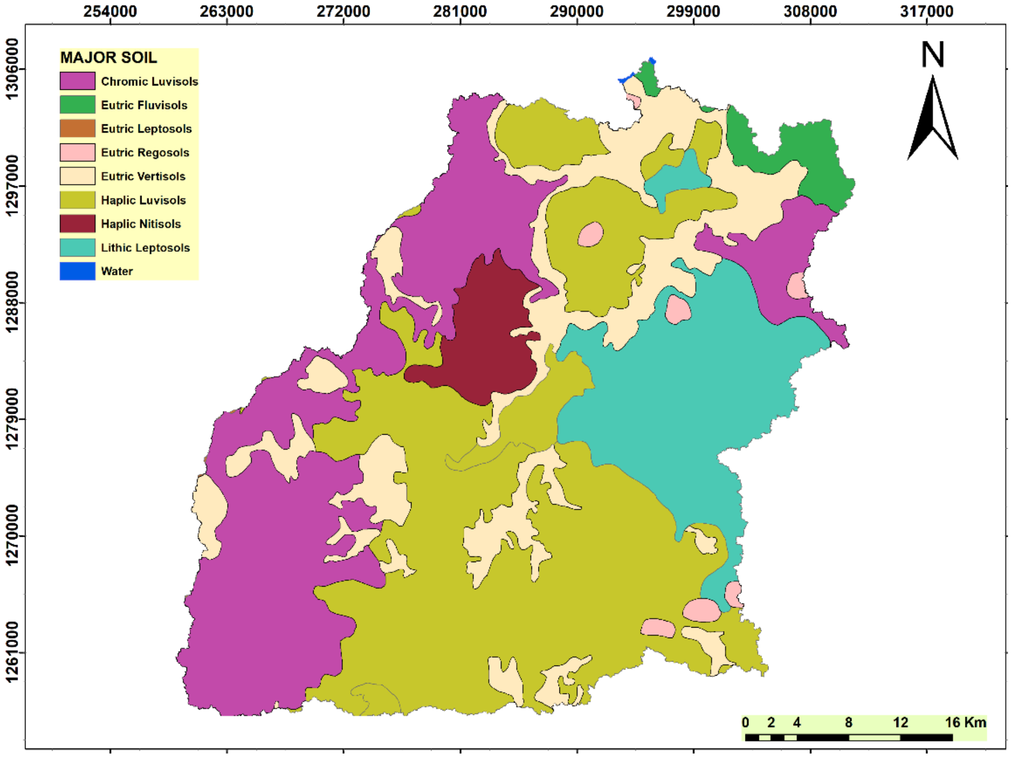

Figure 3.4: Map of major soil types in the study area

3.1.6. Land Cover

The economic activity of the study catchment is mainly depending on rain fed agriculture. Furthermore, irrigated land and perennial crops also cover large parts of the catchment.

The land use/cover classification was derived from www.geoportal.rcmrd.org website and nine land use types were identified (Figure 3.5), for the study area. The largest percentage of the study area (more than 88%) is occupied by annual crop land use types (Table 3.4).

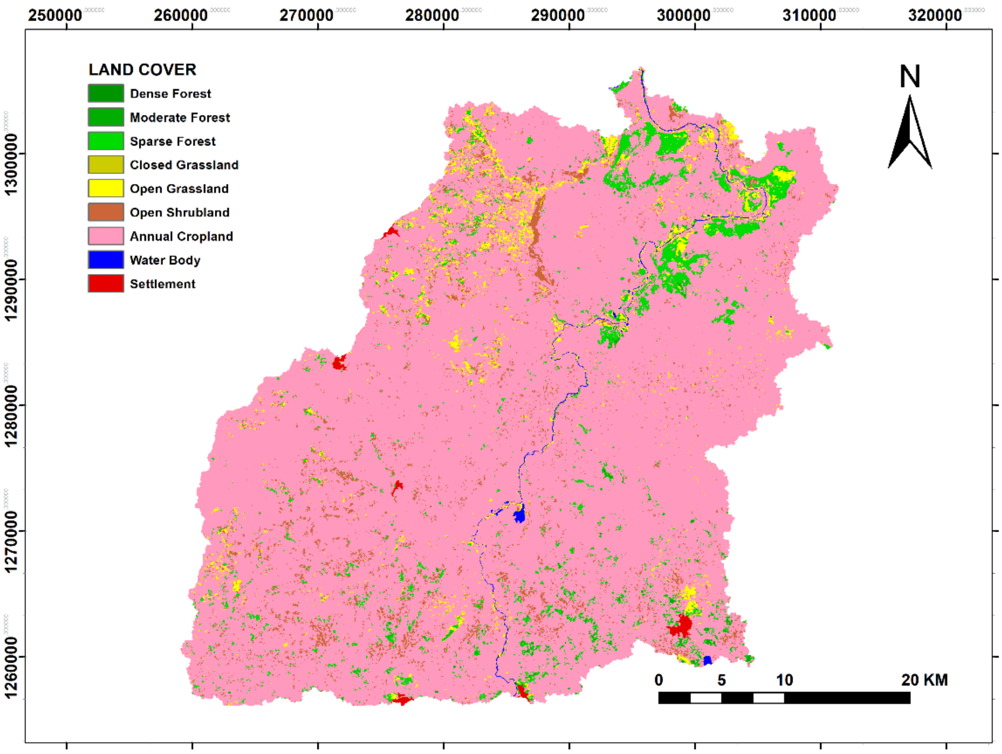

Figure 3.5: Land Use Map of the study area (Source: RCMRD (2015))

Table 3.4: Area and percentage of Land-use land-cover types of the study area.

No	Land-use and land-cover type	Area (km^2)	% Total
1	Dense Forest	0.23	0.01
2	Moderate Forest	6.36	0.37
3	Sparse Forest	68.55	3.99
4	Closed Grassland	0.51	0.03
5	Open Grassland	49.52	2.88
6	Open Shrub land	61.79	3.60
7	Annual Crop land	1,518.65	88.48
8	Water Body	6.01	0.35
9	Settlement	4.85	0.28
	Total	**1,716.47**	**100**

3.2. Data requirements and data preparation

Remote sensing and weather data are used as an input to compute evapotranspiration. Moreover, the SEBAL GRASS python file was used to run the algorism.

3.2.1. Remote Sensing Data

SEBAL requires a satellite image and some weather data. A land-use map for the area is also helpful.

In order to complete the estimation of ET, the main remote sensing data used were the blue, green, red (RED), near infrared (NIR), shortwave infrared (SWIR) and thermal infrared (TIR) bands. All bands were used to derive multi-temporal images of the normalized difference vegetation index (NDVI), leaf area index (LAI), surface albedo (α), net radiation (Rn) and all components in a sequence of calculations required to estimate ET of the season 2016.

The free images were provided from USGS Landsat archive https://earthexplorer.usgs.gov/. Cloud free Landsat-8 data OLI/TIRS for the day of Dec 23, Jan 22, Feb 07 and Mar 10/2016 with Path: 170 and Row: 52 were used as the source of remote sensing data for this study. Only seven bands (2, 3, 4, 5, 6, 7 and 10) were used in SEBAL from eleven bands (1 to 11).

A Digital Elevation Model with 30 m x 30 m resolution (https://earthexplorer.usgs.gov/) was used for watershed delineation, flow accumulation generation, slope length and slope gradient of the study area.

3.2.1.1. Cloudy Conditions

It is important that the image used be for a very clear sky. It is not possible to calculate ET for terrestrial surfaces covered with clouds, since even a thin layer of clouds can reduce considerably the readings of the thermal band and cause big errors in the calculation of sensible heat fluxes (Waters et al., 2002). Therefore, the image must be thoroughly reviewed to detect the presence of a cloud layer.

3.2.1.2. Header File Information

TM images are usually created with an associated "header" file. The header file for the satellite image is a relatively small file that contains important information for the SEBAL process. The following information must be obtained from the header file to enter SEBAL:

- The satellite overpass date and time
- The latitude and longitude of the center of the image
- The sun elevation angle (β) at the overpass time
- Gain and Bias levels for each band for Landsat 7

Accordingly, Landsat-8 OLI/TIRS bands data can be converted to TOA spectral radiance using the radiance rescaling factors provided in the metadata of images.

3.2.1.3. Land-Use Map

A land use map is not a requirement for SEBAL, but it is highly recommended, as it is useful for estimating the surface roughness parameter (Z_{om}). The land use map divides the area of interest into several general classes of land use, such as agriculture, city, water, desert, forest, pasture, etc.

3.2.1.4. Weather Data

The following weather data are recommend for processing SEBAL, Table 3.5 was used for this calculation.

- Wind speed (required, hourly data is preferred)
- Precipitation (daily data are recommended for a several week period prior to the image)

  In addition to wind speed data, the following meteorological data are recommended to calculate baseline ET per hour and per day. If the reference ET data is available for the image area, then the following data is not necessary.

- Humidity (hourly data such as vapor pressure or dew point temperature)
- Solar radiation (hourly is preferred)
- Air Temperature (hourly is preferred)
- Reference evapotranspiration, ET_r (hourly is preferred)

Table 3.5: Hourly weather data for December 23/2016 (Source: EMA)

DOY*	Time (Hr)	Year	WD (Degree)	RF (mm)	Tmax (^{0}C)	Tmin (^{0}C)	RH Max (%)	RH Min (%)	W.Speed (m/s)	Glo.Rad (W/m^2)
358	12 AM	2016	0.45	0	16.90	16.00	56.10	61.30	0.14	0.45
358	1 AM	2016	0.43	0	15.60	13.10	61.60	70.90	0.02	0.45
358	2 AM	2016	0.50	0	12.70	10.50	72.60	81.00	0.07	0.50
358	3 AM	2016	0.53	0	10.40	9.80	79.50	84.60	0.04	1.35
358	4 AM	2016	0.50	0	13.30	10.00	71.10	80.30	0.12	74.45
358	5 AM	2016	0.60	0	21.80	15.70	36.30	66.80	0.50	273.45
358	6 AM	2016	0.73	0	23.00	22.10	31.20	34.50	2.38	475.65
358	7 AM	2016	0.75	0	24.50	23.40	27.80	30.40	2.79	633.45
358	8 AM	2016	0.68	0	25.70	25.00	23.20	26.80	2.54	736.50
358	9 AM	2016	0.68	0	26.70	26.00	21.60	21.90	2.11	774.90
358	10 AM	2016	0.68	0	28.10	27.10	20.90	21.70	1.92	742.15
358	11 AM	2016	0.65	0	28.00	27.60	20.70	26.40	1.67	645.35
358	12 PM	2016	0.68	0	27.50	27.30	24.80	28.30	2.05	498.20
358	1 PM	2016	0.63	0	26.50	25.80	33.00	35.90	1.87	315.10
358	2 PM	2016	0.60	0	25.40	23.70	35.60	38.10	0.97	105.50
358	3 PM	2016	0.40	0	22.40	18.40	43.20	57.50	0.06	6.85
358	4 PM	2016	0.48	0	17.40	15.30	62.60	75.10	0.01	0.50
358	5 PM	2016	0.50	0	15.40	14.10	71.50	75.60	0.00	0.50
358	6 PM	2016	0.60	0	18.90	14.60	38.10	69.80	0.50	0.50
358	7 PM	2016	0.53	0	18.70	16.10	39.40	49.50	0.27	0.45
358	8 PM	2016	0.53	0	14.20	13.00	57.30	61.70	0.05	0.45
358	9 PM	2016	0.58	0	16.70	15.20	42.50	50.60	0.40	0.50
358	10 PM	2016	0.45	0	17.00	16.40	41.10	42.30	0.11	0.45
358	11 PM	2016	0.53	0	17.50	16.50	35.90	40.90	0.32	0.50

* is the sequential day of the year.

Hourly weather data for the date and time of satellite image is required. The weather data should include air temperature, solar radiation, wind speed, and humidity and created before running the REF-ET. Data for other days can be processed at the same time and will be useful for predicting ET for adjacent time periods in SEBAL.

3.2.2. GRASS GIS

GRASS GIS is used to run the SEBAL_GRASS-Master file in this research. GRASS GIS was used in evapotranspiration computation in previous study (Wagner, 2017).

Wagner, (2016) develop a script (python Sebal70.py) to calculate daily evapotranspiration for Landsat 8 images in GRASS-GIS. The script follows the same procedure as SEBAL model manual. Hence, it requires GRASS GIS 7.x software from https://grass.osgeo.org/ Python 2.7.X https://www.python.org/.

Cloud free Landsat 8 scene (LS8 - OLI/TIRS) including MTL file and Reflectance of each band, Digital Elevation Model (DEM) from ASTER UTM format, Re projected the DEM and renamed to MDT_Sebal.TIF, shape file of the study area and SEBAL_GRASS-Master file from (https://github.com/wwolff7/SEBAL_GRASS) all are organized in the same datasets. Data availability and purposes are described in Table 3.6.

Table 3.6: Source, description and purpose of the data used in the study.

No	Type of Data	Source	Description	Purpose	Data Length	Date and/or Time (GMT)	Data Quality
1	Landsat-8 data OLI/TIRS	USGS Earth explorer	OLI Multispectral bands: 30m x 30m OLI Panchromatic band: 15 meters TIRS Thermal bands: 100 meters (resampled to 30 meters to match multispectral bands) 16-bit pixel values /spectral resolution 16 days temporal resolution **Row: 52** **Path: 170** **DOY: 358, 22,38 and 70**	For SEBAL model processing (To calculate Daily and and Seasonal ET)	One Day One Day One Day One Day	12/23/2016 7:52:11 1/22/2016 7:52:02 2/7/2016 7:51:58 3/10/2016 7:51:49	0% Cloud 12% Cloud 21% Cloud 0% Cloud
2	ASTER GLOBAL DEM	USGS Earth explorer	1 ARC-SECOND (30 m x 30 m) resolution	For watershed delineation, for **rah** calculation in SEBAL model and others	No	10/17/2011	Ok
3	Meteorological Data	EMA	Six parametres (Wind speed, relative humidity, rainfall, temprature, wind direction and global radiation) recorded data for Bahir Dar automatic weather station (AWS)	To calculate daily value of reference evapotranspiration and instantanious of reference evapotranspiration during the time of satelite overpass at the weather station as well as for SEBAL model	15 minute	2014-2016	Ok
4	Landuse Map	rcmrd	30 m x30 m resolution schema II	For calculating ET at different landuse types		2008	Ok
5	SEBAL GRASS Phyton file (Sebal70.py)	Wogner Wolff	The code contains all the SEBAL parameters and follows the same procedure developed for SEBAL calculation	To run the SEBAL model using GRASS GIS			Ok

3.3. Software tools used

Different software tools are used in this work. Those software tools with their purpose are reported in Table 3.7.

Table 3.7: Software and tools used for the study

No	Software and Tools	Purpose
1	ArcGIS and QGIS	Analyzing, Displaying, developing maps and viewing Spatial data
2	GRASS-GIS	To run the model/algorithm
3	REF-ET	To calculate instantaneous Etr and Eto for a given period of time

3.4. Methods of Data analysis

The SEBAL algorithm (Bastiaanssen et al. 1998; 2005) is used to compute the evapotranspiration.

To calculate the ET using the SEBAL method, the mathematical equations necessary to construct the algorithms of the processing and analysis models are compiled. Sixteen spatial analysis models were prepared, that is, atmospheric correction models to calculate reflectance, surface albedo, emissivity, surface temperature and elements of the solar radiation balance, including net radiation, soil heat flux, sensitive heat flow, latent heat flow and finally calculate instantaneous and daily evapotranspiration values. The methodological framework used in the research is provided in Figure 3.6.

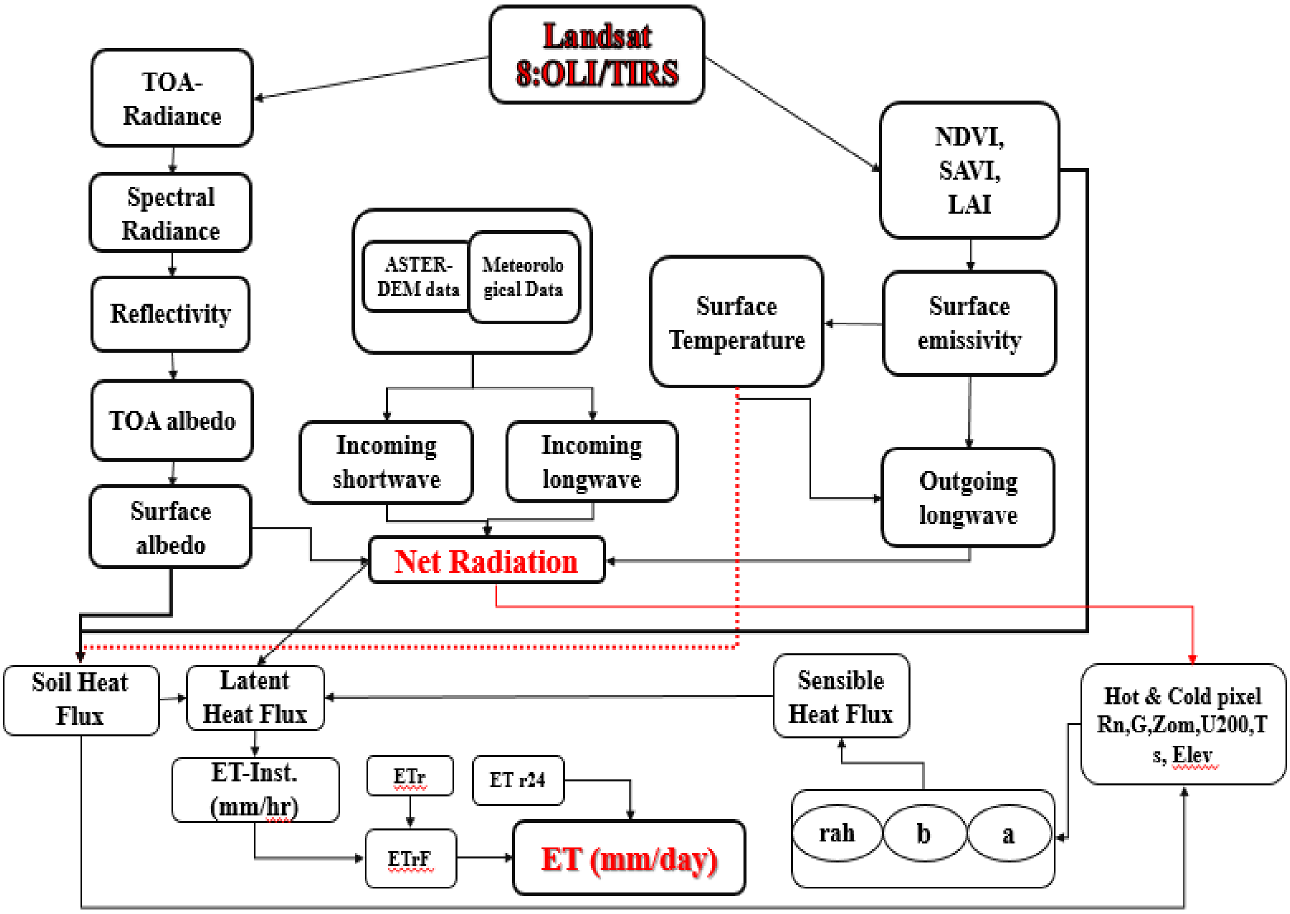

Figure 3.6: General methodological framework employed in the research (Source: SEBAL training manual, 2002)

3.4.1. Atmospheric correction

Correcting satellite data for differences between radiation at the top of the atmosphere (TOA) and radiation at the surface is an important step due to molecules and particulate scattering and absorption in the atmosphere. This reduces the amount of radiation that reaches the surface. Therefore, the TOA reflectance and radiance values must be corrected for atmospheric attenuation so that they characterize the amount of energy that reaches the earth's surface (radiation) and how much is reflected back from the surface (reflection).

Atmospheric correction for solar radiations is important in remote sensing analysis; its necessity depends on the objectives of the analysis (Mather & Tso, 2009).

3.4.2. Spectral Radiance

Estimation of the ground target reflectance starts with converting the pixel value to radiance (Mather & Tso, 2009). Accordingly, Landsat-8 OLI/TIRS bands data can be converted to TOA spectral radiance using the radiance rescaling factors provided in the metadata of images (see equation 3.1)

$$L\lambda = ML * Qcal + AL \text{ ------------------------- } (3.1)$$

Where, $L\lambda$ = TOA **spectral radiance** (Watts/ (m^2*srad*µm));

ML= Band-specific multiplicative rescaling factor from the metadata (RADIANCE_MULT_BAND_x, where x is the band number);

AL= Band-specific additive rescaling factor from the metadata (RADIANCE_ADD_BAND_x; x is the band number);

Qcal = Quantized and calibrated standard product pixel values (DN).

3.4.3. Reflectivity

The reflectivity of a surface is defined as the ratio of the reflected radiation flux to the incident radiation flux. It is computed using the following equation given for Landsat images (Chander & Markham, 2003; Kosa, 2011).

$$\rho\lambda = \frac{\pi \times L\lambda \times {d_r}^2}{ESUN_\lambda \times \cos\theta} \text{ ------------- } (3.2)$$

Where; $\rho\lambda$ = top of atmospheric reflectance,

$L\lambda$ = the spectral radiance for each band,

$ESUN_\lambda$ = the mean solar exo-atmospheric irradiance for each band ($W/m^2/\mu m$),

Cos θ = the cosine of the solar incidence angle (from nadir) is computed using the header file data on sun elevation angle (β) where θ = (90 - β), and

d_r = the inverse squared relative earth-sun distance.

dr is computed using the following equation by (Duffie & Beckman, 1980), also given in FAO 56 paper Crop evapotranspiration (Allen, et al., 1998).

$$dr = 1 + 0.033\cos\left(DOY\,\frac{2\pi}{365}\right) \text{-----------------} (3.3)$$

Where; DOY is the sequential day of the year

Values for d_r range from 0.97 to 1.03 and are dimensionless.

Moreover, land surface reflectance **(**ρ**)** is given by (Moran et al., 1992).

$$\rho = \frac{\pi \times (L\lambda - Lp) \times {d_r}^2}{ESUN_\lambda \times \cos\theta} \text{-----------------} (3.4)$$

$$ESUN = (\pi * dr^2) * RADIANCE\_MAXIMUM \,/\, REFLECTANCE\_MAXIMUM$$

$$L_P = ML * DN_{\min} + AL - 0.01 * ESUN_\lambda * \cos\theta / (\pi * d^2)$$

Where: RADIANCE_MAXIMUM and REFLECTANCE_MAXIMUM are provided by image metadata for Landsat 8.

Lp = Path radiance

3.4.4. Surface Albedo (α)

Surface albedo is defined as the ratio of the reflected radiation to the incident shortwave radiation. According to the equations mentioned in Smith (2010); Kosa (2011); Tasumi, et al. (2008) the values of albedo for the top of atmosphere are calculated as:

$$\alpha_{TOA} = \sum(\omega\lambda \times \rho\lambda) \text{--------------------} (3.5)$$

$$\omega\lambda = \frac{ESUN\lambda}{\sum ESUN\lambda} \text{--------------------} (3.6)$$

Where;		
	α_{TOA}	the weighted albedo.
	ρλ	the reflectivity for each band,
	ωλ	a weighting coefficient for each band (2,3,…7)
	ESUN	Exoatmospheric spectral solar irradiance.

Surface albedo is computed by correcting the α_{toa} for atmospheric transmissivity:

$$\alpha = \frac{\alpha_{TOA} - \alpha_{Path\_radiance}}{\tau_{sw}{}^{2}}$$ ----------- (3.7)

Where; $\alpha_{path\_radiance}$ the average portion of the incoming solar radiation across all bands that is back scattered to the satellite before it reaches the earth's surface, (Ranged from 0.025 to 0.04), in SEBAL and 0.03 is recommended.

τ_{sw} the shortwave atmospheric transmissivity.

$$\tau_{sw} = 0.75 + 2\times10^{-5} \times z$$ ---------------- (3.8)

Where; z is an elevation of area where is defined by ASTER GDEM Data (MDT_Sebal).

3.4.5. Emissivity and Land Surface Temperature

To calculate the surface temperature, first the black body temperature at satellite must be calculated (Chander & Markham, 2003 and Weng, et al., 2004).

$$T_b = \frac{K_2}{\ln\left(\frac{K_1}{L_\lambda} + 1\right)}$$ ------------------------ (3.9)

Where; T_b is black body temperature at satellite in Kelvins (corrected band-10),

K_1 and K_2 are calibration constants for Landsat-8 OLI/TIRS thermal band-10,

$L\lambda$ is spectral radiance in $W.m^{-2}.ster^{-1}.\mu m^{-1}$ and is calculated by the following equation (Weng, Lu, & Schubring, 2004)

$$L_\lambda = 0.0370588 \times DN + 3.2$$ ----------------- (3.10)

To compute the land surface temperature, the black body temperature is corrected with respect to the surface emissivity (ε) values. The surface emissivity is a factor that describes the efficiency of an object radiates energy in comparing with black body (Lillesand, et al., 2004).

The values of emissivity are estimated from NDVI and LAI as follows:

$$\varepsilon = 1.009 + 0.047 \times \ln(NDVI)$$ -------------- (3.11)

Where NDVI > 0, otherwise, emissivity is assumed zero (e.g. water)

$$\varepsilon NB = 0.97 + 0.0033 \times LAI \text{ ---------------------- } (3.12)$$

For *LAI* < 3, ε = 0.98 when *LAI* >= 3;

For water, *NDVI* < 0 and surface albedo < 0.47, ε_0 = 0.985 and εNB = 0.99

For snow, *NDVI* < 0 and surface albedo >= 0.47, ε_0 = *0.985* and εNB = 0.99

Where, εNB is narrow band emissivity.

NDVI (Normalized Difference Vegetation Index), and LAI (Leaf Area Index), are calculated by visible and near infrared bands For Landsat-8, NDVI is a sensitive indicator of the amount and condition of green vegetation. Values for NDVI range between -1 and +1. Green surfaces have a NDVI between 0 and 1 and water and cloud are usually less than zero.

$$NDVI = \left(\frac{NIR - RED}{NIR + RED} \right) \text{ ------------------- } (3.13)$$

SAVI is an index that attempts to "subtract" the effects of background soil from NDVI so that impacts of soil wetness are reduced in the index. It is computed as:

$$SAVI = \left(\frac{(1 + L)(NIR - RED)}{L + NIR + RED} \right) \text{ -------------------- } (3.14)$$

Where; L is a constant for SAVI. If L is zero, SAVI becomes equal to NDVI. A value of 0.5 frequently appears in the literature for L (Waters, et al., 2002).

LAI is the ratio of the total area of all leaves on a plant to the ground area represented by the plant. It is an indicator of biomass and canopy resistance. LAI is computed for southern Idaho using the following empirical equation:

$$LAI = -\ln \frac{\left(\frac{0.69 - SAVI}{0.59} \right)}{0.91} \qquad \text{ ------------------- } (3.15)$$

Then the corrected land surface temperature (T_S) is calculated according to the formula given by (Weng, et al., 2004).

$$Ts = \frac{Tb}{1 + (\lambda \times Tb / \gamma) \times \ln \varepsilon NB} \quad \text{---------------- (3.16)}$$

Where: **λ** is the average of limiting wavelengths of band 10 of Landsat8-TIRS (10.8)

$$\gamma = h \times c / a(0.01438m.K) \quad \text{-------------------- (3.17)}$$

γ = 14380

a = Boltzmann constant (1.38x10^{-23} j.k)

h = Plank’s constant (6.626x10^{-34} J.s)

c = velocity of light (2.998 x 10^8 m/s)

The DEM corrected surface temperature is calculated by the following equation:

$$T_{s-dem} = Ts + 0.0065\Delta Z \quad \text{---------------- (3.18)}$$

Where; Δz is the elevation of each pixel minus the elevation of a datum (meters). The term Δz is positive if the elevation of a pixel is higher than the datum. The representative elevation for the image, usually at the weather station, is used for the datum elevation.

The corrected surface temperature (Ts-dem) is used for the selection of the two "anchor" pixels. The Ts image shows high and low pixels instead of wet or dry pixels due to the lifting effects. For pixels higher than the data, the lapse correction is added and Ts-dem is greater than Ts. The use of Ts-dem data allows us to find really wet and dry pixels.

3.4.6. Solar Radiations Elements and ET

ET estimation by SEBAL is a model to calculate ET from remote sensing images. It depends on the thermodynamic equilibrium between the turbulent transport process in the atmosphere and the laminar process in the secondary surface. This process called the energy balance of the earth's surface (Bastiaanssen, et al., 1998). According to Hailegiorgis, (2006) the exchange of energy that governs the ET process on the surface of the vegetation can be expressed mathematically as:

$$Rn = G + H + \lambda ET \quad \text{----------------------------------- (3.19)}$$

$$R_n = RS\downarrow - \alpha\, RS\downarrow + RL\downarrow - RL\uparrow - (1-\varepsilon o)\, RL\downarrow \text{--------------------- (3.20)}$$

Where, ε0 is surface emissivity

Incoming shortwave radiation (RS↓) is calculated from the available climatic parameters, such as sunshine hours, relative humidity, minimum and maximum temperature cloud cover, and geographic location. The amount of shortwave radiation (RS↓) that remained on the surface is a function of (α) which is a reflection coefficient defined as the ratio between the reflected radiant flux and the incident radiant flux over the solar spectrum. It is calculated using satellite image information on the spectral radiance for each satellite band.

Incoming shortwave radiation (RS↓) is calculated using the solar constant, the solar incidence angle, a relative earth-sun distance and a calculated atmospheric transmissivity.

$$Rs \downarrow = G_{Sc} \times \cos\theta \times d_r \times \tau_{sw} \text{ -------------- } (3.21)$$

Where G_{Sc} is solar constant (1,367 W/m^2), θ is the solar incidence angle, $\theta = 90 - \phi$, ϕ = sun elevation angle, given in the header data file of the LANDSAT_8 imagery, *dr*= the inverse squared relative earth-sun distance, and τ_{sw} is the atmospheric transmissivity.

The outgoing longwave radiation (RL↑) is computed at each pixel using Stefan-Boltzmann equation (see equation 3.22) with a calculated surface emissivity and surface temperature (Waters, et al., 2002).

$$RL \uparrow = \varepsilon 0 \times \sigma \times Ts^4 \text{ ------------------ } (3.22)$$

Where **ε** is the broadband surface emissivity, **σ** is Stefan-Boltzmann constant (5.67 x 10^{-8} W/ m^2 / K^4) and Ts is surface temperature in K.

The surface emissivity is the ratio of the actual radiation emitted by a surface to that emitted by a black body at the same surface temperature. In SEBAL, emissivity is computed as a function of a vegetation index.

The final term in Equation (3.20), (1-εo) RL↓, represents the fraction of incoming longwave radiation that is lost from the surface due to reflection.

The incoming longwave radiation (RL↓) is the downward thermal radiation flux from the atmosphere (W/m^2). It is computed using a modified Stefan-Boltzmann equation with atmospheric transmissivity and a selected surface reference temperature. To compute the incoming longwave radiation ($RL\downarrow$), the hot and cold pixels must be selected as anchor pixels. Cold pixel is selected from the area of high density of vegetation cover with LAI > 3 from irrigated crops, at which the surface temperature and near surface air temperature are assumed to be similar.

$$H_{Cold} = Rn - G - 1.05 * ETr \text{ ---------------------- (3.23)}$$

Where, ETr is the rate of ET from reference.

The hot pixel is located at bare soil or rock outcrop with LAI range and calculated using the equation given below:

$$H_{Hot} = Rn - G \text{ -------------------------- (3.24)}$$

Using the procedure mentioned in (Waters, et al., 2002) hot and cold pixel parameters are calculated. The surface temperature of cold pixel is used as near surface air temperature (Ta) to calculate the incoming longwave radiation (RL↓) using the following equation:

$$RL \downarrow = \varepsilon_a \times \sigma \times Ta^4 \text{ ------------------ (3.25)}$$

The incoming longwave radiation (RL↓) is computed since the transmissivity of air is no longer a constant for all pixels. The reference temperature (T_{cold}) is adjusted for the lapse effect in a similar way as in equation below:

$$T_{Cold} = T_{Cold} + 0.0065\Delta Z \text{ ---------------- (3.26)}$$

Where; Δz is the elevation of the "cold" pixel minus the elevation of each pixel. The elevation of the "cold" pixel is taken from the DEM subset image by entering its coordinates.

εa is the atmospheric emissivity (dimensionless), σ is the Stefan-Boltzmann constant (5.67×10^{-8} W/m^2/K^2), and

Ta = Tcold is the near surface air temperature for selected cold pixel in (K).

The atmospheric emissivity ε_a is computed from the following empirical equation given by (Waters et al., 2002).

$$\varepsilon a = 0.85 \times (-\ln \tau_{sw})^{0.09} \text{ ------------------------ (3.27)}$$

Where; τsw is the atmospheric transmissivity calculated from Equation (3.8)

3.4.7. Soil Heat Flux (G)

Soil heat flux is the rate of heat storage in the soil as a result of the temperature gradient between the soil surface and the underlying upper layers of the soil (Opoku Duah, et al., 2008; Waters et al., 2002; Tasumi et al., 2003).

G is calculated empirically using vegetation indices, surface temperature and surface albedo and H is calculated using observations of wind speed, estimated surface roughness and temperature differences between surface and air. SEBAL uses an iterative process to correct atmospheric instability due to the floating effects of surface heating. SEBAL first calculates the G/Rn ratio using the following empirical equation developed by Bastiaanssen (2000) that represents the values close to noon:

$$G/R_n = T_s/\alpha(0.0038\alpha + 0.0074\alpha^2)(1 - 0.98NDVI^4) \text{ --------------- (3.28)}$$

Where; T_s is the surface temperature (^{0}C),

α is the surface albedo, and

NDVI is the Normalized Difference Vegetation Index.

G is then readily calculated by multiplying G/Rn by the value for Rn computed in (equation 3.20)

First, the ratio of G/Rn is computed and checked for the condition of NDVI < 0: and if Ts < 4 ^{0}C and α > 0.45, then the ratio of G/Rn will be assigned equal to 0.5. The result image will be converted to soil heat flux (G) in W/m^2 by multiplying the ratio G/R_n by R_n.

3.4.8. Sensible Heat Flux (H)

Sensible Heat Flux (H) is the rate of heat loss to the air by convection and conduction, due to temperature gradients (Morse, et al., 2001) and (Oberg & Melesss, 2006). It is computed using the following equation for heat transport:

$$H = (\rho \times c_p \times dT)/r_{ah} \text{ ------------ (3:29)}$$

Where: **H** is sensible heat flux, **ρ** is air density (kg/m^3), C_p is air specific heat (1004 J/kg/K), dT is near surface temperature differences (T_1-T_2) in K between two heights (Z_1 & Z_2) above the zero plane displacement, and r_{ah} is aerodynamic resistance to heat transport (s/m).

The sensible heat flux (H) is a function of the temperature gradient, surface roughness, and wind speed. Equation (3.30) is difficult to solve because there are two unknowns, r_{ah} and dT.

$$dT = aT_s + b, \text{------------------------------ (3.30)}$$

Where *a* and *b* are the correlation coefficients which are calculated iteratively from the data of hot and cold anchor pixels using Excel-spreadsheet.

The aerodynamic resistance to heat transport (r_{ah}) is computed for neutral stability as:

$$r_{ah} = \frac{\ln\left(\frac{Z_2}{Z_1}\right)}{U * \times k} \text{ -------------------------- (3.31)}$$

Where; Z1 and Z2 are heights in meters above the zero plane displacement (d) of the vegetation, u* is the friction velocity (m/s) which quantifies the turbulent velocity fluctuations in the air, and k is von Karman’s constant (0.41) **(**Waters, et al., 2002)**.**

To start the process of H computation, some weather data should be collected. Wind speed U_x, Z_{om} at weather station, air temperature, and air pressure. These parameters are used in the computation of H. many steps to do Figure 3.7.

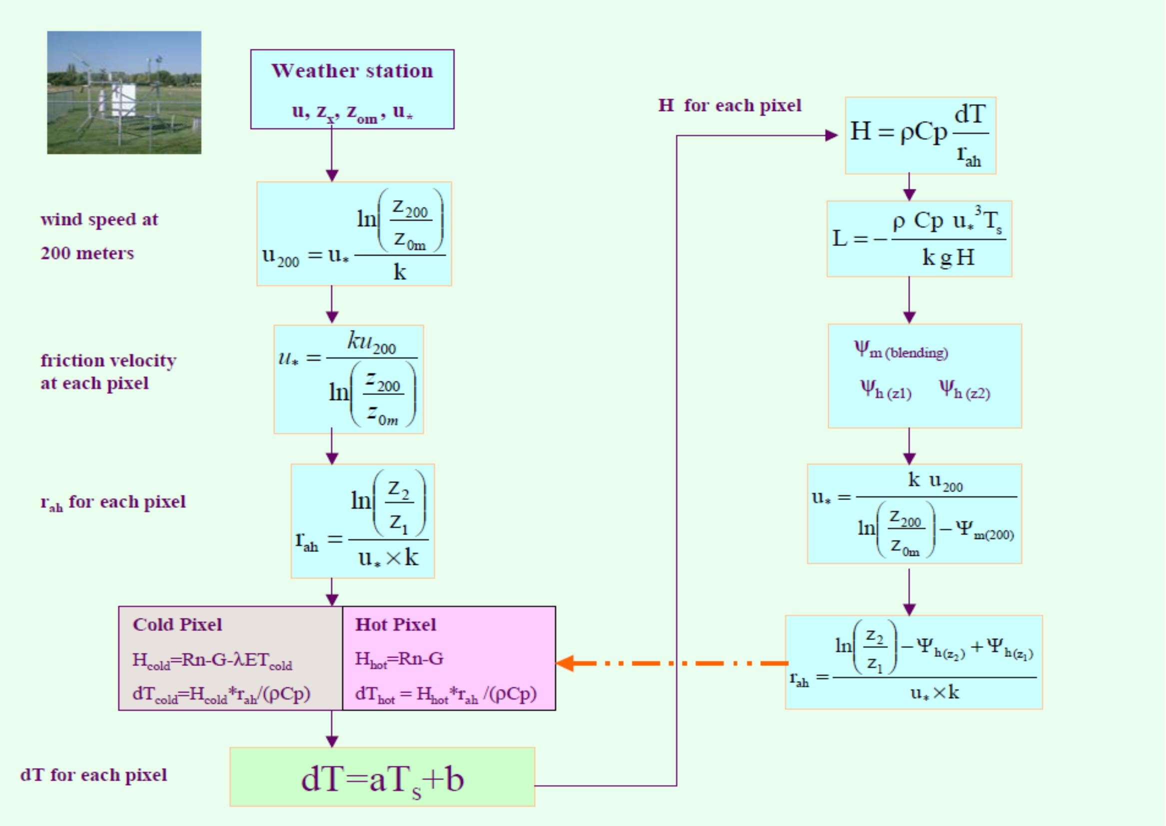

Figure 3.7: Flow Chart of the Iterative Process for the Calculation of Sensible Heat (H) (Source: SEBAL training manual, 2002)

The friction velocity (U*) is computed using the logarithmic wind law for neutral atmospheric conditions:

$$U* = K \times U_x / \ln(Z_x / Z_{om}) \text{ ------------------------ } (3.32)$$

Where: *Ux* is the wind speed (m/s) at height Zx meter (Oberg & Melesss, 2006).

Zx is the height above surface in meter (eg. 2 m)

Zom is surface roughness for momentum transport (m)

Wind speed and surface roughness values must be assigned "pixel by pixel", to calculate the friction velocity with spatial variation. SEBAL estimates a pixel based value for friction velocity by extrapolating downward from a common value for wind speed determined at a blending height at around 200 m where it is assumed that wind speed is independent of the surface roughness. The wind speed of the blending height (200 m) is extrapolated upward from an observed wind speed at a weather station then assigned "pixel by pixel" using the equation:

$$U* = K \times U_{200} / \ln(Z_{200} / Z_{om})\text{------------------ (3.33)}$$

To compute H for the first round for the two pixels, ET for hot pixel is assumed to be zero, which is a bare soil as given above equation (H_{cold} and H_{hot}).

Calculate dT should for the two pixels as follows:

$$dT_{cold} = H_{cold} \text{ x } r_{ah\_cold} / (\rho cold \text{ x } C_p) \text{ ------------------ (3.34)}$$

$$dT_{hot} = H_{hot} \text{ x } r_{ah\_hot} / (\rho hot \text{ x } C_p) \text{ ----------------------- (3.35)}$$

The momentum roughness length (*Z_{om}*) for each pixel is calculated as a function of *LAI* (Opoku Duah, et al., 2008).

$$Z_{om} = 0.018 \times LAI \quad \text{----------------------- (3.36)}$$

The atmospheric conditions of stability have a large effect on the aerodynamic resistance (*rah*).

The length of Monin-Obukhov (L) is used to define the conditions of stability of the atmosphere in the iterative process (note, this is not the same "L" that is used in the SAVI calculation). It is a function of the heat and momentum fluxes and is calculated as follows:

$$L = \frac{\rho \times C_p \times U_*^{\ 3} \times T_s}{K \times g \times H} \quad \text{--------------------- (3.37)}$$

Where; ρ and C*p*, Ts, *K* and H are defined previously, g is g is the gravitational constant (9.81 m/s^2).

Depending on the atmospheric conditions, the values of the stability corrections for the impulse and the heat transport (ψm and ψh) are calculated iteratively by the use of xls spreadsheets designed on the basis of the equations mentioned (Waters, et al., 2002).

The values of the cold and hot pixels are adjusted to their elevations and are computed iteratively and then the last iteration values of a, b and *rah* are used to calculate the sensible heat flux (H).

These two terms are calculated depending on the value of L since there are three conditions; stable (L >1), unstable (L<1), and neutral conditions (L= 0) using the equations developed by Paulson (1970) and Webb (1970).

If L< 1, unstable conditions:

$$\psi_{m,200m} = 2\ln\left(\frac{1+x_{200m}}{2}\right) + \ln\left(\frac{1+x_{200m}{}^{2}}{2}\right) - 2ArcTAN(x_{200m}) + 0.5\pi \text{ ------- } (3.38)$$

$$\psi_{h,2m} = 2\ln\left(\frac{1+x_{2m}{}^{2}}{2}\right) \text{ ---------------------- } (3.39)$$

$$\psi_{h,0.1m} = 2\ln\left(\frac{1+x_{0.1m}{}^{2}}{2}\right) \text{ ------------ } (3.40)$$

Where,

$$X_{200m} = \left(1-16\frac{200}{L}\right)^{0.25}, \quad X_{2m} = \left(1-16\frac{2}{L}\right)^{0.25} \text{ and } X_{0.1m} = \left(1-16\frac{0.1}{L}\right)^{0.25} \text{ ------- } (3.41)$$

If L > 0, stable conditions:

$$\psi_{m,200m} = -5\left(\frac{2}{L}\right), \; \psi_{m,2m} = -5\left(\frac{2}{L}\right) \text{ and } \psi_{m,0.1m} = -5\left(\frac{0.1}{L}\right) \text{ -------- } (3.42)$$

If L= 0; neutral conditions/stable so the two terms are zero: ψ_m and $\psi_h = 0$.

A corrected value for the friction velocity (u*) is now computed for each successive iteration as:

$$U* = \frac{U_{200}K}{\ln\left(\frac{200}{Z_{0m}}\right) - \psi_{m(200m)}} \text{ ----------------------- } (3.43)$$

Where;

U_{200} is the wind speed at 200 meters (m/s),

K is von Karman’s constant (0.41),

Z_{om} is the roughness length for each pixel (m),
Ψm(200m) is the stability correction for momentum transport at 200 meters.

A corrected value for the aerodynamic resistance to heat transport (rah) is now computed during each iteration as:

$$r_{ah} = \frac{\ln\left(\frac{Z_2}{Z_1}\right) - \psi_{h(z2)} + \psi_{h(z1)}}{U * xK} \text{ ------------------------ (3.44)}$$

Where
z2 = 2.0 meters,
z1 = 0.1 meters, and
ψh (Z_2) and ψh (Z_1) are the stability corrections for heat transport at 2 meters and 1 meters.

Repeat the stability correction steps four to five times until Rah and dT are stabilized for the hot pixel for sensible heat flux estimation.

The mathematical formulation of the sensible heat flux is based on the theory of the transport of mass of heat and momentum between the surface (limit) and the environment of the near surface. The sensible heat flux (H) is a function of the temperature gradient, the roughness of the surface and the wind speed.

The iteration process is performed with the initial value of ψm (correction factor for moment transport) and ψh (correction factor for heat transport) as zero and then calculates the friction velocity maps (U*), aerodynamic drag for heat transport (Rah) Sensitive Heat (H), Monin Obukhov Length (L), xm, ψm, xh, ψh in sequential order. The value of ψm and ψh at the end of the first iteration is taken for the next iteration. This iterative process is carried out until a constant value of sensible heat is reached.

3.4.9. Latent Heat Flux, Instantaneous ET, & Reference ET Fraction

Latent heat flux is the rate of latent heat loss from the surface due to evapotranspiration (Waters, et al., 2002). It can be computed for each pixel using Equation 3.45

$$\lambda ET = R_n - G - H \text{ ---------------------- (3.45)}$$

Where: λ ET is an instantaneous value for the time of the satellite overpass (W/m^2).

An instantaneous value of ET in equivalent evaporation depth is computed as:

$$ET_{inst} = 3600 \times \frac{\lambda ET}{\lambda} \text{ --------------------- (3.46)}$$

Where: ET$_{inst}$ is the instantaneous ET (mm/hr), 3600 is the time conversion from seconds to hours, and λ is the latent heat of vaporization or the heat absorbed when a kilogram of water evaporates (J/kg).

$$\lambda = 2.501 - (T_a - 273) \times 0.002361 \text{ ----------------------- (3.47)}$$

Where, Ta is the mean air temperature (K).

The Fraction of reference ET (ETrF) is defined as the ratio of the instantaneous ET calculated (ETinst) for each pixel to the reference ET (ETr) calculated from meteorological data:

$$ETrF = \frac{ET_{inst}}{ET_r} \text{ ------------------------ (3.48)}$$

Where, ET$_{inst}$ is instantaneous ET (mm/hr) and ETr is the reference ET at the time of the image from the REF-ET software (mm/hr) developed by University of Idaho (Allen R. , 2000). ETrF is similar to the well-known crop coefficient, Kc. ETrF is used to extrapolate ET from image time to periods of 24 hours or more.

The reference evapotranspiration (ETr) is the ET rate expected from a well-defined surface of full-cover alfalfa or clipped grass. ETr is used in SEBAL to estimate the ET at the “cold” pixel and to calculate the reference ET fraction (ETrF) and ETr can be computed for a given weather station using the REF-ET software made available by the University of Idaho www.kimberly.uidaho.edu/ref-et/ (Allen R. , 2000).

In general, ETrF values are expected to vary from 0 to 1. With a totally dry pixel, ET = 0 and ETrF = 0. A pixel in a well-established field of alfalfa or corn may occasionally have an ET slightly higher than ETr and, therefore, ETrF > 1. However, ETr generally represents an upper limit in ET for large extensions of well-watered vegetation. Negative values for ETrF can occur in SEBAL due to systematic errors caused by several assumptions made earlier in the energy balance process (Waters, et al., 2002).

The meteorological parameter for the instantaneous image time will have to be interpolated from averages representing two periods of time. A general formula for determining what periods of time to use in interpolation is the following equation (Waters, et al., 2002).

$$t_1 = \operatorname{int}\left[\frac{t_{image(Localtime)}}{\Delta t} + \frac{1}{2} - Flag_{period}\right]\Delta t + Flag_{DST} \text{ ----------- } (3.49)$$

$$t_2 = t_1 + \Delta t \text{ -------------------- } (3.50)$$

Where; t1 = time identifier for the first weather period in hours

t2 = time identifier for the second weather period in hours

Δt = length of weather period in units consistent with t1 and t2 (i.e., hours)

$t_{\text{image (local time)}}$ = the satellite image time (local time, with no adjustment for daylight savings) = GMT + Correction

$Flag_{period}$ = a flag for the way that the weather data period is represented by its "time label". $Flag_{period}$ = zero if the time label is the endpoint of the weather data period; = 1 if the time label is the beginning of the weather data period; = 0.5 if the time label represents the midpoint of the weather data period.

FlagDST = a flag for use of DST in the weather data set. FlagDST = 0 if no DST is used and FlagDST = 1 hour if DST is used in the weather data set. DST is not used in Ethiopia.

Estimate the instantaneous velocity of the wind by applying a simple linear data interpolation, assuming that the averages of the periods represent measurements that occur at the midpoints of the periods. A general interpolation formula based on the identifiers of period t1 and t2 of the above equation is:

$$Data_{image} = Data_{t1} + \frac{\left(Data_{t2} - Data_{t1}\right)}{\Delta t}\left[t_{image(Localtime)} - \left(t_1 - Flag_{DST} + \Delta t Flag_{Period} - \frac{\Delta t}{2}\right)\right] \text{--- } (3.51)$$

Where:

Data t_1 = the average value for the specific data parameter (i.e., wind or ETr) for the t_1 time.

Data t_2= the average value for the specific data parameter (i.e., wind or ETr) for the t_2 time.

The values obtained from this calculation are useful for calculating SEBAL algorism using GRASS-GIS.

3.4.10. 24-Hour Evapotranspiration (ET_{24})

Daily values of ET (ET_{24}) are often more useful than instantaneous ET. SEBAL computes the ET_{24} by assuming that the instantaneous ETrF computed in the model is the same as the 24-hour average. Finally, the ET_{24} (mm/day) can be computed as:

$$ET_{24} = ETrF \times ET_{r\_24} \text{ -------------------------- (3.52)}$$

Where, ETr-24 is the cumulative 24-hour ETr for the day of the image (Waters, et al., 2002). This is calculated by adding the hourly ETr values over the day of the image.

$$ET_{r\_24} = \sum_{h}^{24} ET_{r-h} \text{ ---------------------------- (3.53)}$$

ET_{24} or Daily ET is computed in this model. Enter the files for H, G, Rn, Ts, and the values for ETr and ETr-24. Save the output files and the model. The range of values for ET_{24} can be colored so that ET intensity can be readily observed on the image.

3.4.11. Seasonal Evapotranspiration (ET_{Season})

The development of an evapotranspiration map that covers a season/month of full growth is often valuable. This can be derived from the 24-hour evapotranspiration data by extrapolating the ET_{24} proportionally to the reference evapotranspiration (ETr). Suppose that the ET for the entire area of interest changes in proportion to the change in the ETr in the weather station. ETr is calculated for a specific location and, therefore, does not represent the actual condition in each pixel. However, this does not matter, since ETr is used only as an index of the relative change in climate, and therefore ET, for the area of the image. Also, suppose that the ETrF calculated for the time of the image is constant throughout the period represented by the image (Waters, et al., 2002).

Based on Waters et al., (2002) the following steps show the process for computing seasonal ET:-

- The first step is to decide the length of the season for which ET is desired.
- The second step is to determine the period represented by each satellite image within the chosen season (i.e., if the image for the above season are on

December 23, then the period represented by the image would be December 1 to December 31).

- The third step is to compute the cumulative instantaneous reference ET (ETr) for the period represented by the image. This is simply the sum of daily ETr values over the period. These 24-hour values can be computed using the REF-ET software. The same ETr method must be used through the SEBAL process.
- The fourth step is to compute the cumulative ET for each period as follows:

$$ET_{period} = ET_r F_{period} \sum_{1}^{n} ET_{r-24} \text{ ------------------------- } (3.54)$$

$$ET_{Commulative} = \sum_{i=1}^{n} (ET_{SEBAL-24})_i (K_m)_i \text{ ------------------------ } (3.55)$$

Where; ET_rF_{period} is the representative *ETrF* for the period, ET_{r-24} is the daily ETr, and n is the number of days in the period. Units for ET_{period} will be in mm when ET_{r-24} is in mm/day.

Where: $ET_{SEBAL-24}$ is the 24-hour ET predicted by SEBAL for each pixel of image "i",

Km is the multiplier for ET for the representative period where, Km = (Cumulative ETr)/ (24-hour ETr), and

n is the number of satellite images processed.

Units for $ET_{cumulative}$ will be in mm when $ET_{SEBAL-24}$ is in mm/day.

- The fifth step is to compute the seasonal ET by summing all of the ET_{period} values for the length of the season.

The following difficulties encountered in the computation of seasonal ET must be understood:

- If there is any cloud layer in one of the images used for the seasonal ET calculation, then there can be no ET or ETrF values represented for this area during the period represented by the image. ETrF values can be assigned to cloud covered areas by interpolating between ETrF values for images on both sides of the cloud cover image.
- When the ETr in the weather station is not representative of the entire area (i.e., where the image covers many mountainous valleys or includes coastal and inland areas that have different effects of clouds or wind that are not well correlated through the image), then the image should be divided into secondary images, each with its own value of ETr. In this situation, simple executions of SEBAL must be carried out for each sub-image.

- If an agricultural field is dry on the day of the image and then irrigated the next day, the increase of ET for this field during the representative period of the image will not be considered in the seasonal ET calculation. This problem can be minimized if many satellite images are used for the calculation of seasonal ET with each image representing a shorter period of time. You can also apply a water balance model to each pixel that includes irrigation and precipitation as inputs.

3.5. Building of Spatial Modeling

To achieve the requirements of SEBAL method for estimating the spatio-temporal evapotranspiration on pixel wise, all the mathematical equations described above, meteorological data, remote sensing data and SEBAL-GRASS python file were used for the analysis of the model to meet the final objective. The model was run in GRASS GIS software and analyzed in QGIS and ArcGIS software.

3.6. Ground based evapotranspiration estimation methods

A large number of empirical methods have been developed over the last 50 years to estimate evapotranspiration from different climatic variables. Some of these derived from the now well-known Penman equation (Penman 1948) to determine evaporation from open water, bare soil, and grass (now called evapotranspiration) based on a combination of an energy balance and an aerodynamic formula. The REF-ET software can calculate the reference ET for different empirical models. The result obtained from SEBAL calculation for Dec, 23 2016 were compared with Penman-Monteith method, which is globally accepted as a standard method.

4. Results and Discussions

The analysis of results (maps, statistics and graphs) and discussion for the spatial variation of solar radiation elements and evapotranspiration of pixel wise are presented under this chapter.

4.1. Weather Data & Reference Evapotranspiration, ETr

The results of the instantaneous reference evapotranspiration (Etr) is provided in Table 4.1

Table 4.1: Computed ETr from weather data for December 23/2016.

Mon	Day	Year	DoY	HrMn	Tmax (0c)	Tmin (0c)	Rs (Solar Radiation) (W/m2)	Wind (m/s)	DewP (0c)	ASCE stPM Etr (mm/hr)	ASCE stPM Eto (mm/hr)
12	23	2016	358	0	16.900	16.000	0.000	0.140	8.370	-0.030	-0.020
12	23	2016	358	100	15.600	13.100	0.000	0.020	8.270	-0.030	-0.020
12	23	2016	358	200	12.700	10.500	0.000	0.070	7.760	-0.030	-0.020
12	23	2016	358	300	10.400	9.800	1.000	0.040	7.190	-0.030	-0.020
12	23	2016	358	400	13.300	10.000	74.000	0.120	7.680	0.020	0.010
12	23	2016	358	500	21.800	15.700	273.000	0.500	9.610	0.190	0.170
12	23	2016	358	600	23.000	22.100	475.000	2.380	5.440	0.500	0.390
12	23	2016	358	700	24.500	23.400	633.000	2.790	4.920	0.670	0.530
12	23	2016	358	800	25.700	25.000	736.000	2.540	3.940	0.760	0.610
12	23	2016	358	900	26.700	26.000	775.000	2.110	2.790	0.780	0.640
12	23	2016	358	1000	28.100	27.100	742.000	1.920	3.540	0.750	0.620
12	**23**	**2016**	**358**	**1100**	**28.000**	**27.600**	**645.000**	**1.670**	**5.140**	**0.650**	**0.540**
12	**23**	**2016**	**358**	**1200**	**27.500**	**27.300**	**498.000**	**2.050**	**6.520**	**0.540**	**0.420**
12	23	2016	358	1300	26.500	25.800	315.000	1.870	9.270	0.410	0.310
12	23	2016	358	1400	25.400	23.700	105.000	0.970	8.890	0.170	0.130
12	23	2016	358	1500	22.400	18.400	7.000	0.060	10.100	0.010	0.000
12	23	2016	358	1600	17.400	15.300	0.000	0.010	10.740	0.000	0.000
12	23	2016	358	1700	15.400	14.100	0.000	0.000	10.100	0.000	0.000
12	23	2016	358	1800	18.900	14.600	0.000	0.500	8.080	0.020	0.010
12	23	2016	358	1900	18.700	16.100	0.000	0.270	5.360	0.020	0.010
12	23	2016	358	2000	14.200	13.000	0.000	0.050	5.900	0.000	0.000
12	23	2016	358	2100	16.700	15.200	0.000	0.400	4.600	0.020	0.010
12	23	2016	358	2200	17.000	16.400	0.000	0.110	3.640	0.000	0.000
12	23	2016	358	2300	17.500	16.500	0.000	0.320	2.780	0.020	0.010
										Daily ETo	**4.33**

4.1.1. Instantaneous Wind Speed and ETr Calculation

From Table 4.1, the instantaneous wind speed and the reference ET at the satellite overpass time are determined.

Hence, the instantaneous value of reference evapotranspiration from the weather station and instantaneous wind speed value at satellite overpass time (ETr & U @10:52:11 local time) is **0.61mm/hr** and **1.81m/s** respectively and the daily value of reference evapotranspiration (ETo) from the weather station was **4.33 mm/day**.

Table 4.2 shows instantaneous wind speed, ETr and ETo at image time (local time) for the month Dec, Jan, Feb and Mar. Those values are useful for seasonal calculation (selected months).

Table 4.2: Instantaneous wind speed, ETr and ETo at image time 2016

Date	**23-Dec**	**22-Jan**	**7-Feb**	**10-Mar**
Wind speed @ the time of satellite overpass (Local time) (m/s)	1.81	1.88	1.83	1.77
Instantaneous Reference evapotranspiration @ the time of satellite overpass (Local time) (mm)	0.61	0.66	0.59	0.71
Daily ASCE stPM **ETo** (mm)	4.33	4.39	3.83	5.02

4.2. Surface Radiation Balance

4.2.1. Reflectance

With Semi-Automatic Classification Plugin (SCP), each band of the original Landsat image of the study area was converted to surface reflectance using the method Dark Object Subtraction (DOS1) and to TOA reflectance. Figure 4.1 shows higher in closed grassland (0.072) and lower in forest areas (0.027). Hence, at low reflectance, surface temperature remains low with increasing reflectance because of the presence of sufficient water under these conditions. At higher reflectance, surface temperature is higher. This result was supported by Yuei-An & Sanjib (2014).

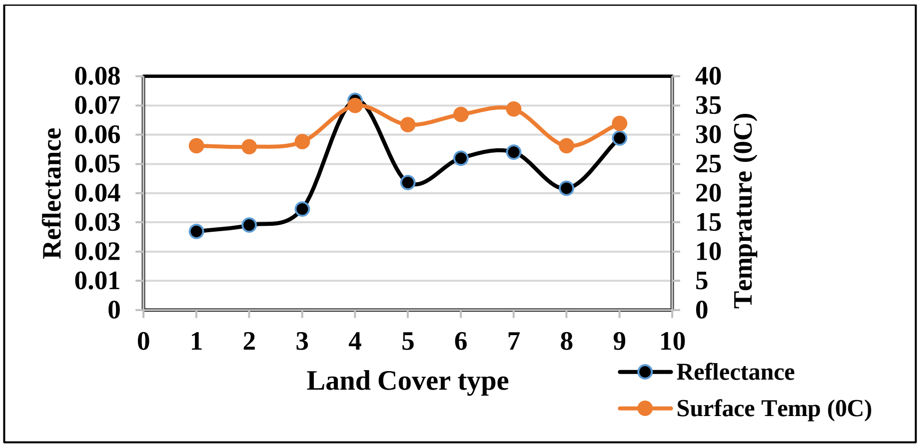

Figure 4.1: Graphical representation of land cover type, surface temperature & reflectance

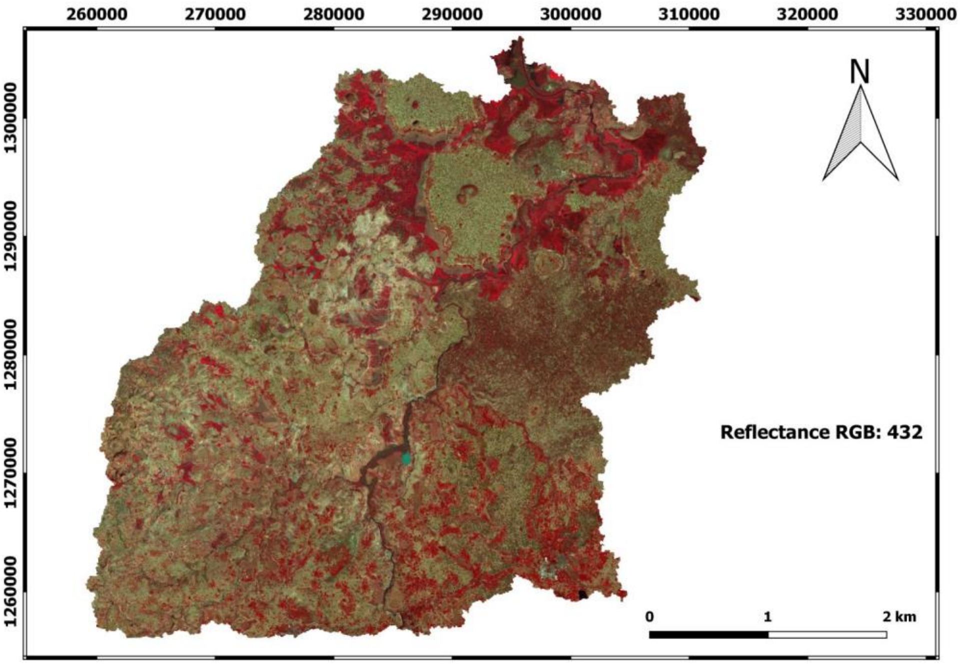

Figure 4.2: Map of reflectance (Band 2 to 7)

4.2.2. Surface albedo (α)

The result of the surface albedo is shown in the Figure 4.3 and its albedo values are ranges in between 0.027 to 0.500 that is in the recommended range [0, 1]. The minimum, maximum, range, mean and standard deviation values were used for the characteristics of land cover classes' indications. Mean values are the most important statistic parameters and the value of the surface albedo within each class of land cover is shown in the Figure 4.4. The lower surface albedo represent for water body, forest and grass land having average value of 0.106, 0.117 and 0.123 respectively recognised due to high absorption properties. While closed grassland, annual cropland, open shrub and settlement having the highest albedo with average value of 0.194, 0.163, 0.164, 0.172 and 0.194 respectively this is because of the low absorption and scattering from such land cover types. Ayad et al., (2016), supported this result.

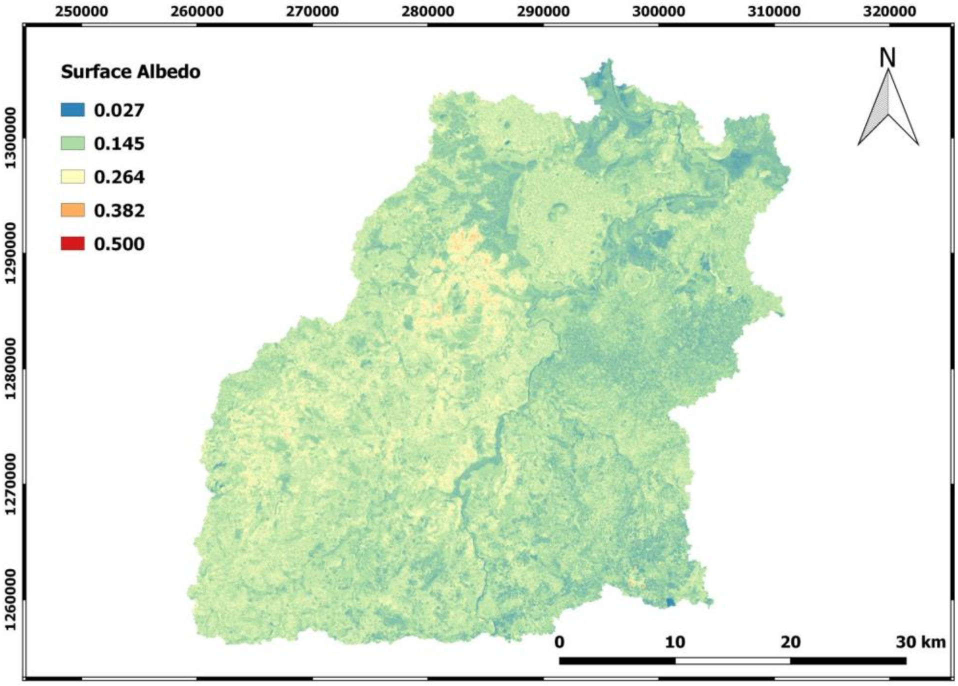

Figure 4.3: Map of Surface albedo

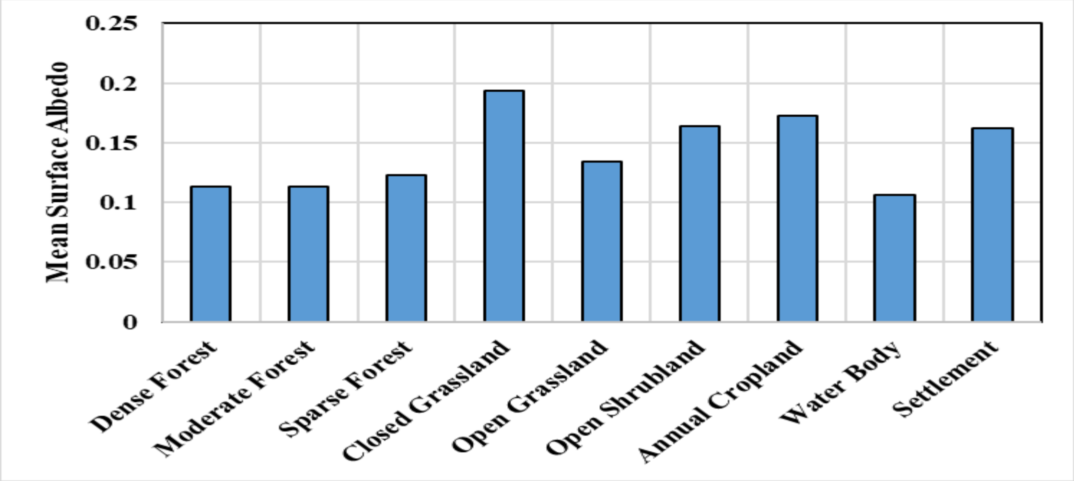

Figure 4.4: Graphical representation of average surface albedo for different land covers

4.3. Incoming shortwave radiation (Rs↓)

Figure 4.5 represents the result of the incoming shortwave radiation from SEBAL for Dec 23/2016 at the satellite overpass time (see Appendix 5). The values are in the ranges between (814.47 to 834.58 W/m^2). As shown in this figure higher values are located in southwest part of the study area due to higher elevation and angle of sun elevation.

As a consequence of the calculation method of atmospheric transmissivity, a consistent positive altitudinal gradient in the RS↓ is observed. The calculation of transmissivity could be improved by taking into account the cloudiness or the suspended fine dust in the air. However, this type of satellite data cannot be used in the presence of clouds and there are no significant sources of fine dust in the study area. Therefore, their effect can be neglected in the calculation of the transmissivity.

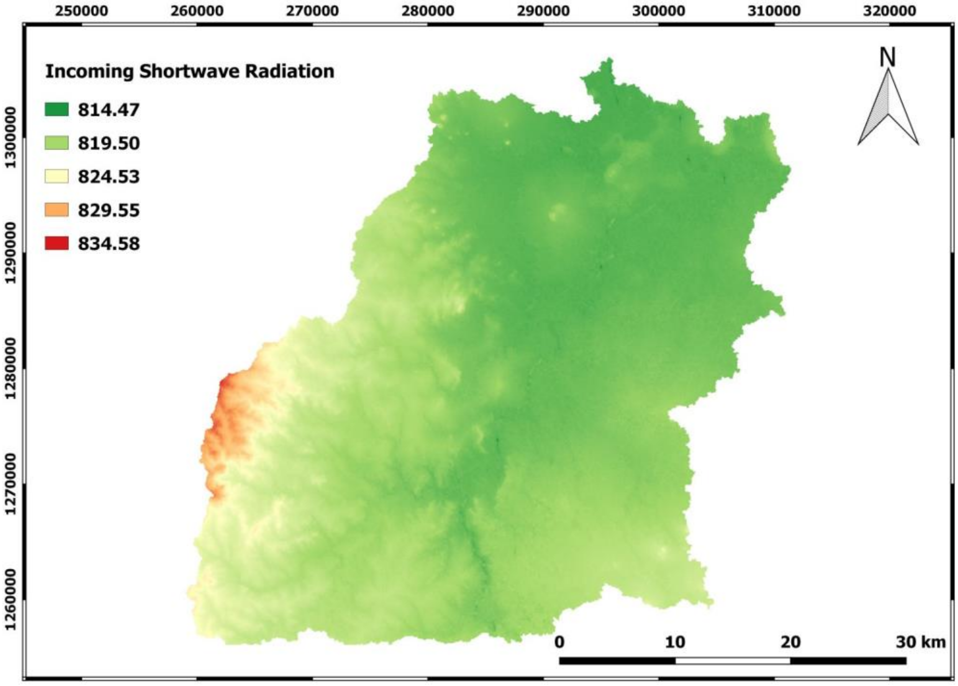

Figure 4.5: Map of Incoming shortwave radiation (W/m^2)

4.4. Outgoing Longwave Radiation (RL↑)

The outgoing longwave radiation is the thermal radiation flux emitted from the earth's surface to the atmosphere (W/m^2) primarily dependent on the temperature of the surface. The hotter the surface the more radiant energy it will emit. Three commonly used vegetation indices are computed in SEBAL using GRASS-GIS.

4.4.1. Normalized Difference Vegetation Index (NDVI)

The NDVI value for the study region was calculated from the above equation. The spatial variation of the computed NDVI map for the study catchment is reported in Figure 4.6 showing values ranging between -0.90 to 0.85 on 23 December 2016. From Figure 4.7, the areas along with the water body represent low NDVI of the mean value 0.12, whereas 4.37% of the area coverage (forest) showing high NDVI with the mean value of 0.61.

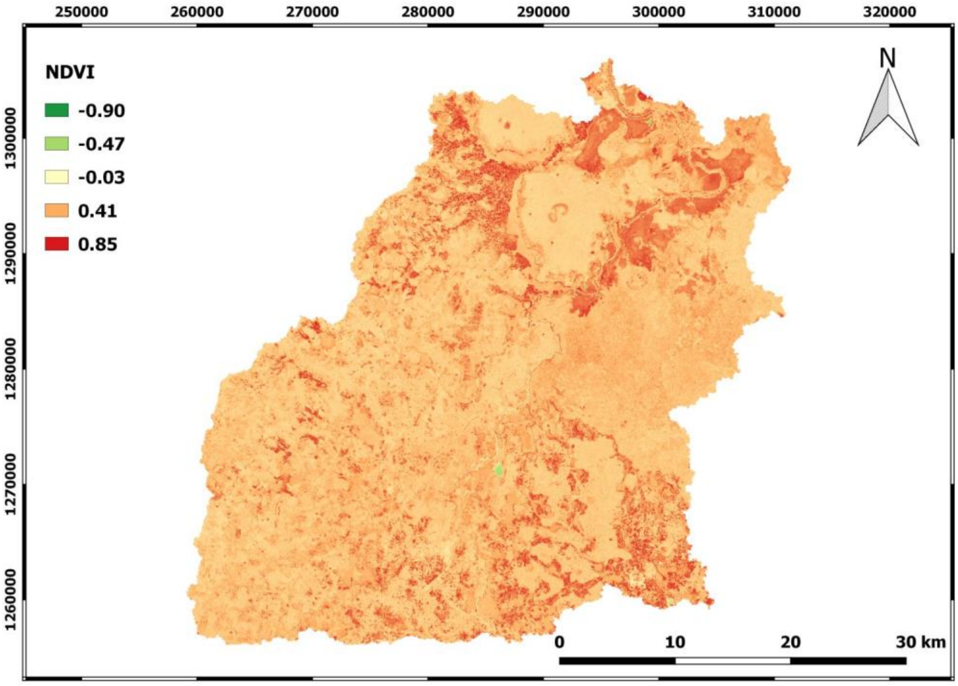

Figure 4.6: Map of Normalized Difference Vegetation Index

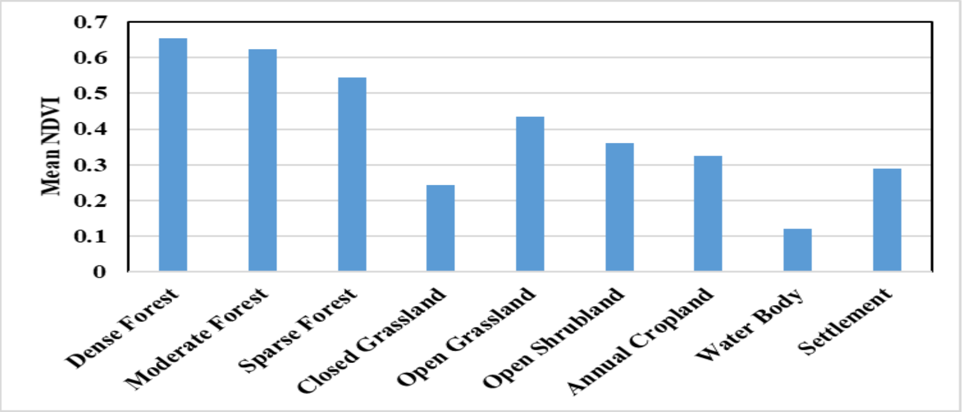

Figure 4.7: Graphical representation of average NDVI for different land covers

4.4.2. Soil Adjusted Vegetation Index (SAVI)

SAVI is computed using the equation given above. An example of SAVI map generated for the study area is given in Figure 4.8 and shows a variation in value in the range of -0.26 to 0.68 on 23 December 2016.

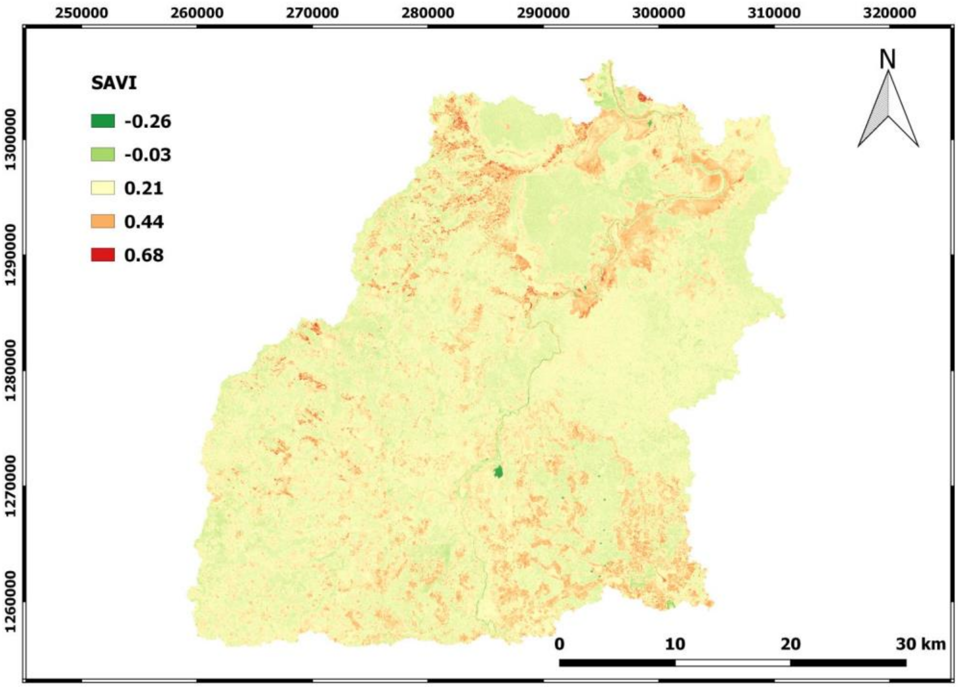

Figure 4.8: Map of Soil Adjusted Vegetation Index

4.4.3. Leaf Area Index (LAI)

LAI is computed using the above empirical equation. Figure 4.9 shows the adjusted value of leaf area index for the study area. The LAI values varied from 0.00 to 4.38 on 23 December 2016. The areas along with the closed grassland represent low LAI of the mean value 0.12, whereas 4.37% of the area coverage (forest) showing high LAI with the mean value of 0.68.

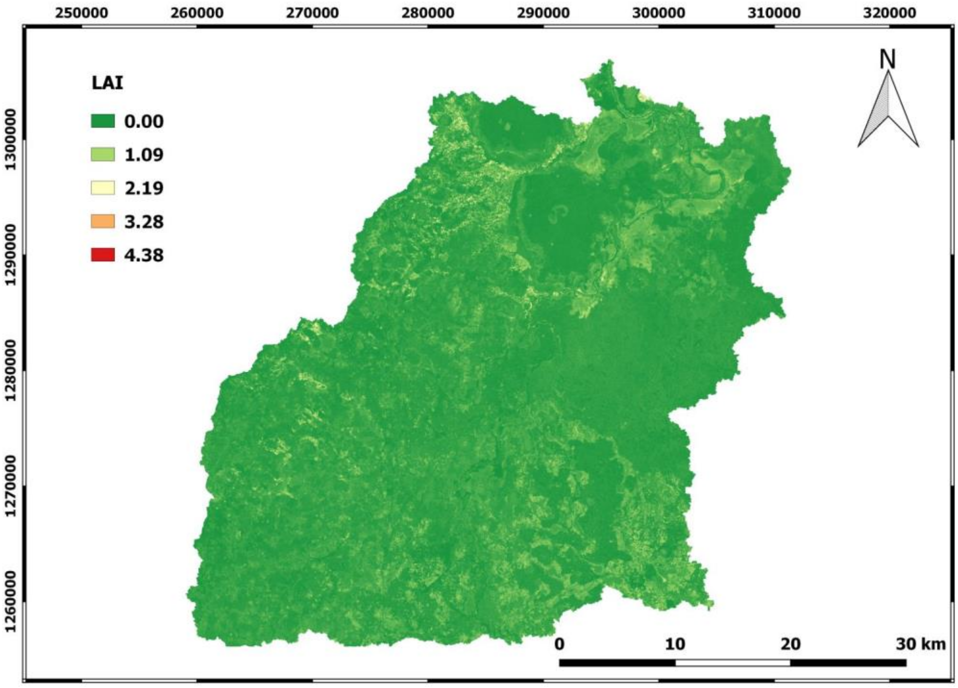

Figure 4.9: Map of Leaf Area Index

4.4.4. **Surface emissivity** (ε)

Surface emissivity maps are generated for the study is given in Figure 4.10 and shows a variation in value in the range of 0.95 to 0.99 for both emissivity on 23 December 2016. The broadband surface emissivity is used to calculate total long wave radiation emission from the surface, while narrowband surface emissivity is used for the calculation of surface temperature. The values of both emissivity for all the land cover classes are relatively close Appendix 6. Hence, water body have higher emissivity in both cases.

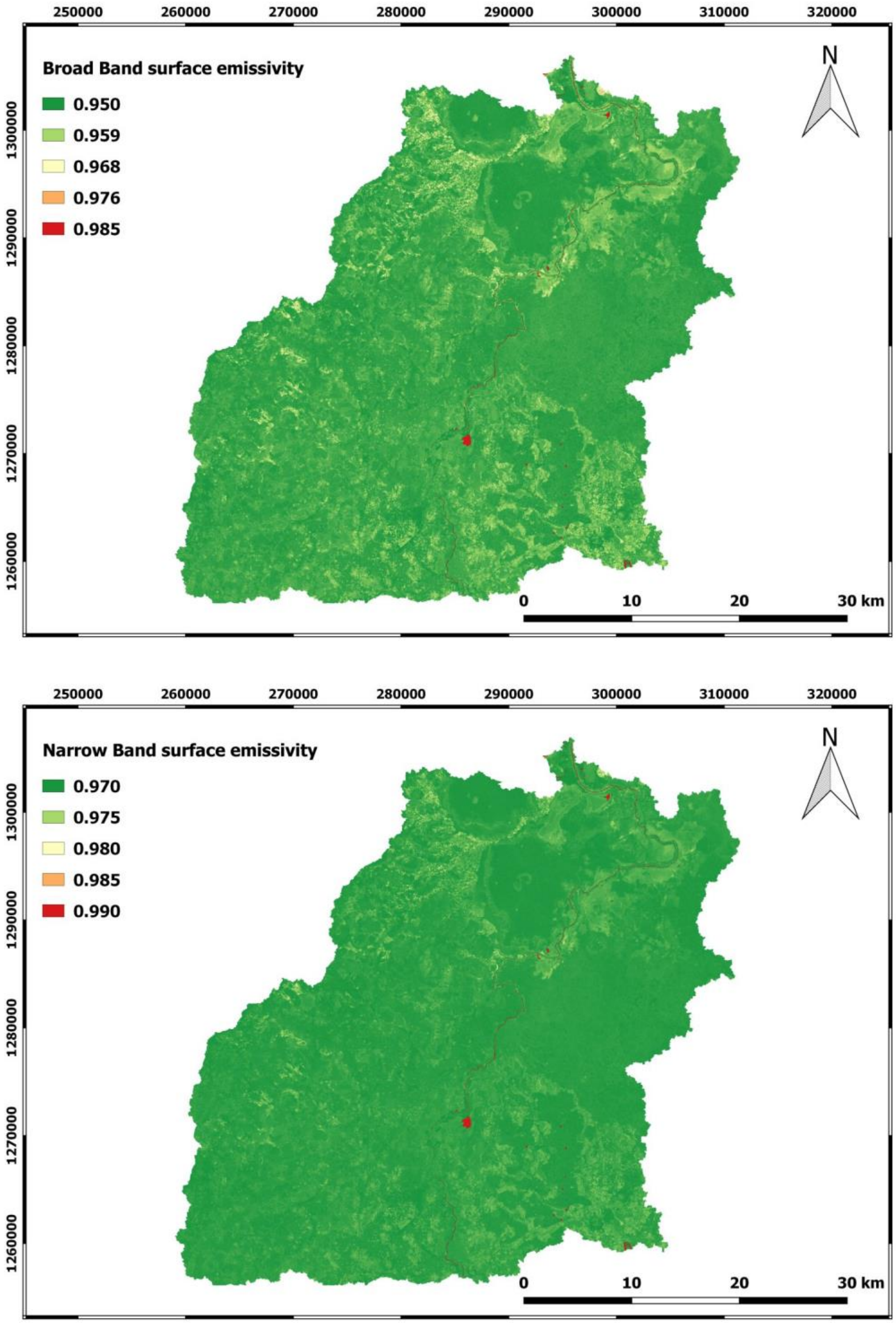

Figure 4.10: Map of Broad and Narrow Band Surface Emissivity

4.4.5. Surface Temperature (Ts)

Using the radiant temperature and the computed value of surface emissivity (narrow band surface emissivity εNB), the surface temperature (K) map is derived as shown in Figure 4.11. The image clearly shows the dependence of the Surface Temperature estimation on the surface albedo and the vegetation. The land surface temperature shows low variations in the mean temperature values ranged from 28.23 ^{0}C in forest area and water body to 33.28 ^{0}C for the other land cover types (Figure 4.12).

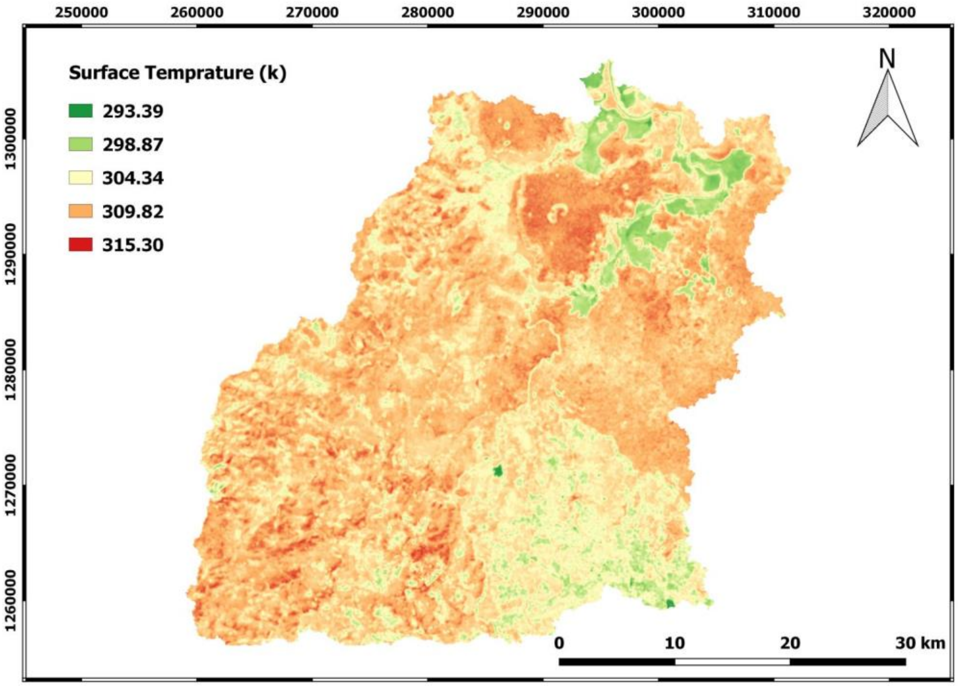

Figure 4.11: Map of Surface Temperature (K)

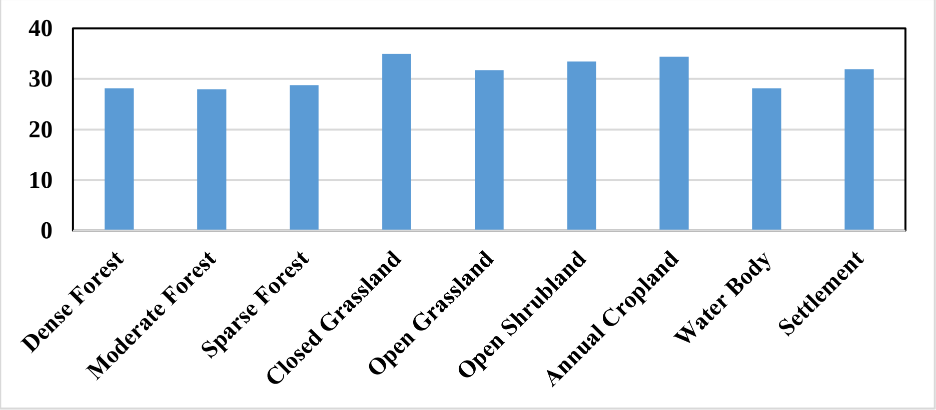

Figure 4.12: Graphical representation of mean surface temperature for land covers

Finally, using the Stefan-Boltzmann equation the outgoing longwave radiation (RL↑) is computed. Values for RL↑ can range from 200 – 700 W/m^2 depending on the location and time of the image (Waters, et al., 2002). As shown in the Figure 4.13, the range of outgoing longwave radiation and was found to range from 406.250 to 533.118 W/m^2 on 23 December 2016 for the study area at the satellite overpass time (see Appendix 5). Figure 4.14 states that the emitted longwave radiation is lower in water body and forest areas while higher in relatively in other land cover types.

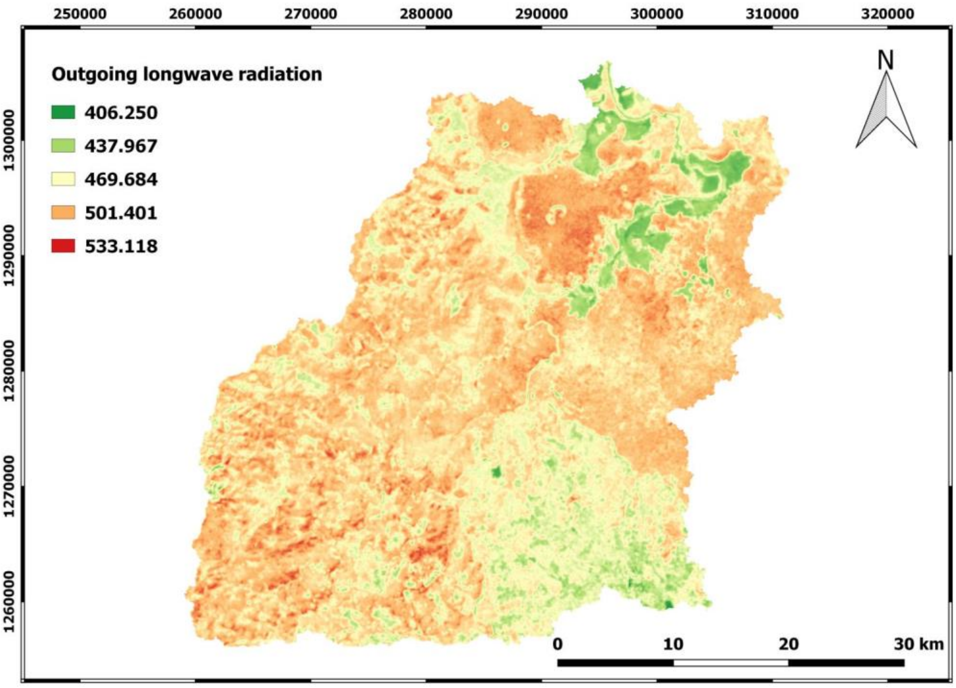

Figure 4.13: Map of Outgoing Longwave Radiation (W/m^2)

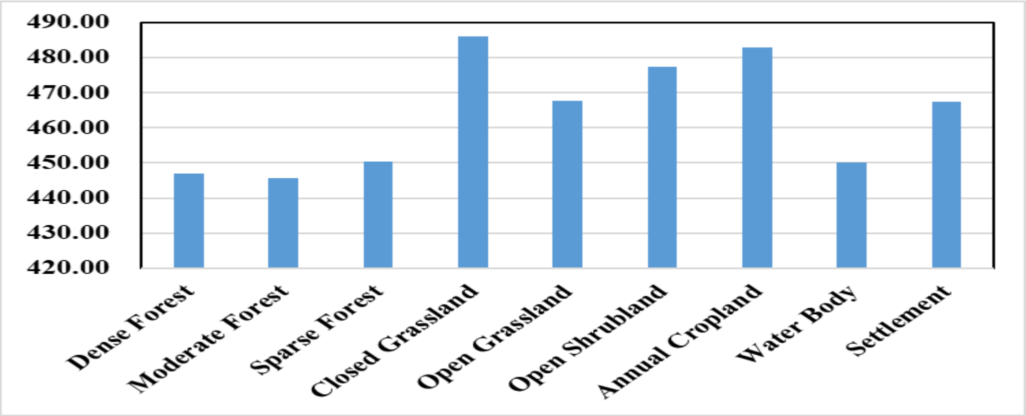

Figure 4.14: Graphical representation of mean outgoing longwave radiation for land covers

4.5. Incoming Longwave Radiation ($R_L\downarrow$)

GRASS-GIS map calculator can calculate cold pixel temperature in K using NDVI (NDVI > 0.4), surface temperature (median) and surface albedo. Selecting appropriate cold pixel location in irrigation areas are useful the calculation of incoming longwave radiation, net radiation and soil heat flux. However, it is difficult to select the appropriate location. In this case, the maximum value of cold pixel temperature location was used.

Values for RL↓ can range from 200 to 500 W/m^2, depending on the location and time of image (Waters et al., 2002). As shown in the Figure 4.15, the range of outgoing longwave radiation is 375.99 to 379.58 W/m^2 for Dec 23/2016 at the satellite overpass time and lower in southwest part of the study area due to higher elevation. The incoming longwave radiation shows close variations in the mean radiation values ranged from 378.46 to 379.11 W/m^2 for all land cover types (Figure 4.16).

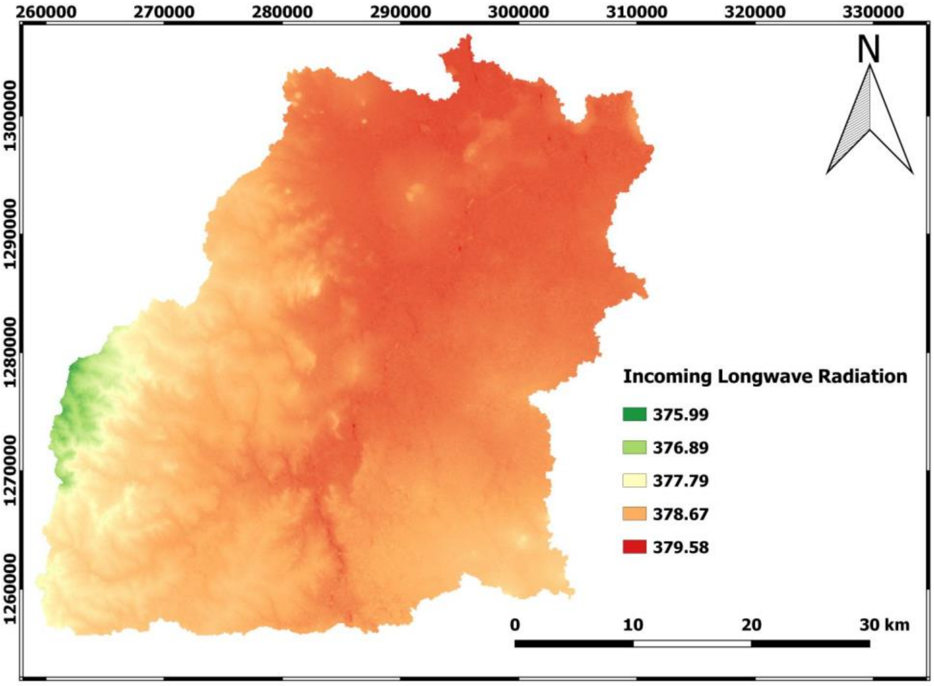

Figure 4.15: Map of Incoming Longwave Radiation (W/m^2)

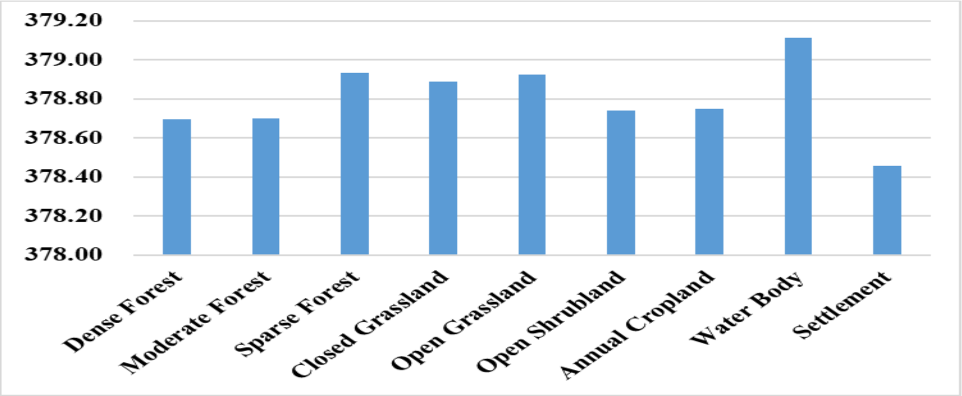

Figure 4.16: Graphical representation of mean incoming longwave radiation for each land covers.

4.6. Net Surface Radiation Flux (Rn)

Using surface albedo (α), outgoing longwave radiation (RL↑) and broadband surface emissivity (ε0) along with the incoming shortwave radiation (RS↓) and the incoming longwave radiation (RL↓), net radiation flux was calculated. Figure 4.17 shows that, the range of net surface radiation is -125.31 to 754.55 W/m^2 at the satellite overpass time for Dec 23/2016. The mean Rn (561.13 W/m^2) have been found within the range from 100 to 700 W/m^2, depending on the surface image (Waters et al., 2002).

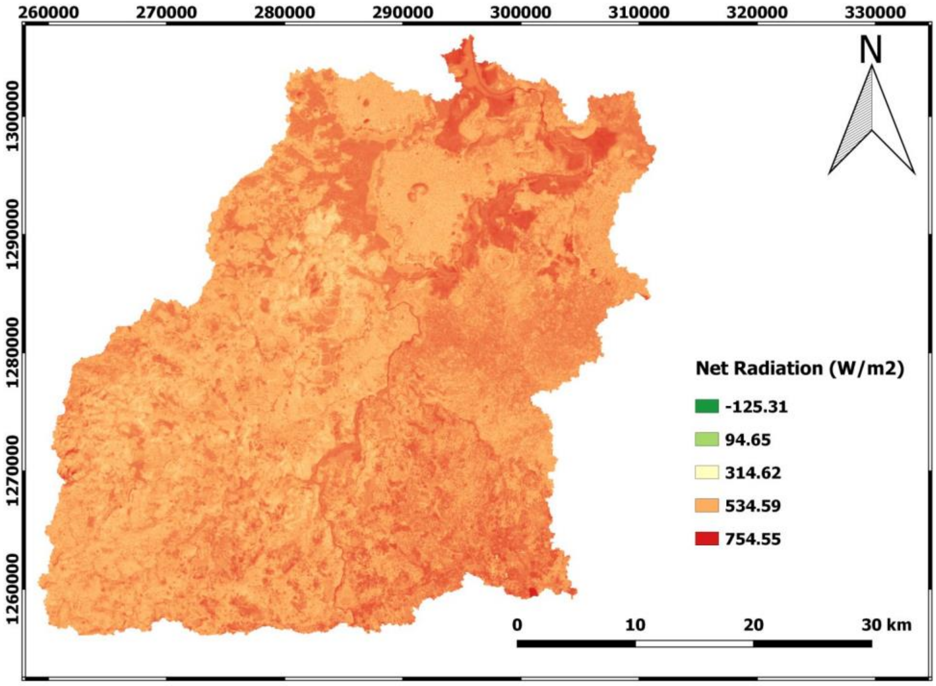

Figure 4.17: Map of Net Surface Radiation (W/m^2)

4.7. Surface Energy Balance

SEBAL procedure is to compute the terms G and H of the surface energy budget equation. The net radiation flux (Rn) is the net amount of radiant energy that is available at the surface for warming the soil, warming the air, or evaporating soil moisture. This is written as the surface energy budget equation. SEBAL computes the latent heat flux as a “residual” of net radiant energy after soil heat flux and sensible heat flux are subtracted.

4.7.1. Soil Heat Flux (G)

The evaluation of G is usually presented as a ratio G/Rn is related to factors such as, the normalized difference vegetation index (NDVI), surface temperature, surface albedo and net radiation (Rn).

The maximum soil heat flux for the study area on 23 December 2016 Figure 4.18 was estimated at 377.28 W/m^2 at the satellite overpass time for 23 December 2016. Negative ground heat flux value represents the soil is cooling that means the subsurface is warmer than the surface and then heat is transferred upwards and found in annual cropland cover type. In this case, maximum value was found in water body. On the contrary, a positive ground heat flux means that the surface is warmer than the subsurface, then heat is transferred downwards via conduction.

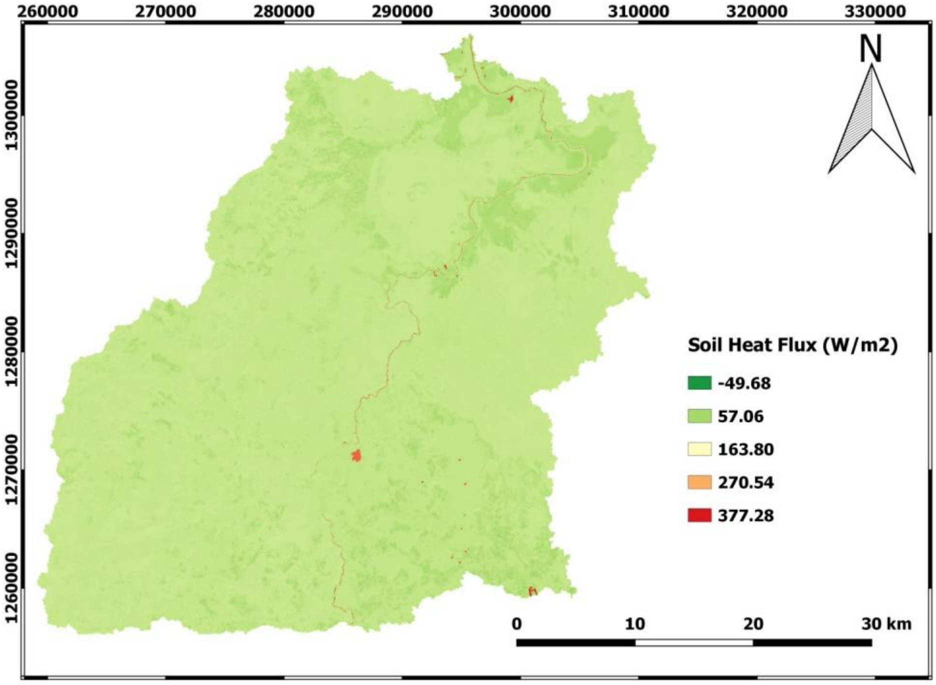

Figure 4.18: Map of Soil Heat Flux (G) (W/m^2)

4.7.2. Sensible Heat Flux (H)

Figure 4.19 shows the final map of sensible heat derived after six (6) runs of the iterative process. Sensible heat flux ranged from -41.04 to 373.26 W/m^2 for the study area on 23 December 2016 at the satellite overpass time. For wet pixel usually with low temperature and high NDVI is assumed that sensible heat flux is zero. While, the sensible heat flux was put the maximum value of the difference between net radiation and soil heat flux selected as the dry pixel.

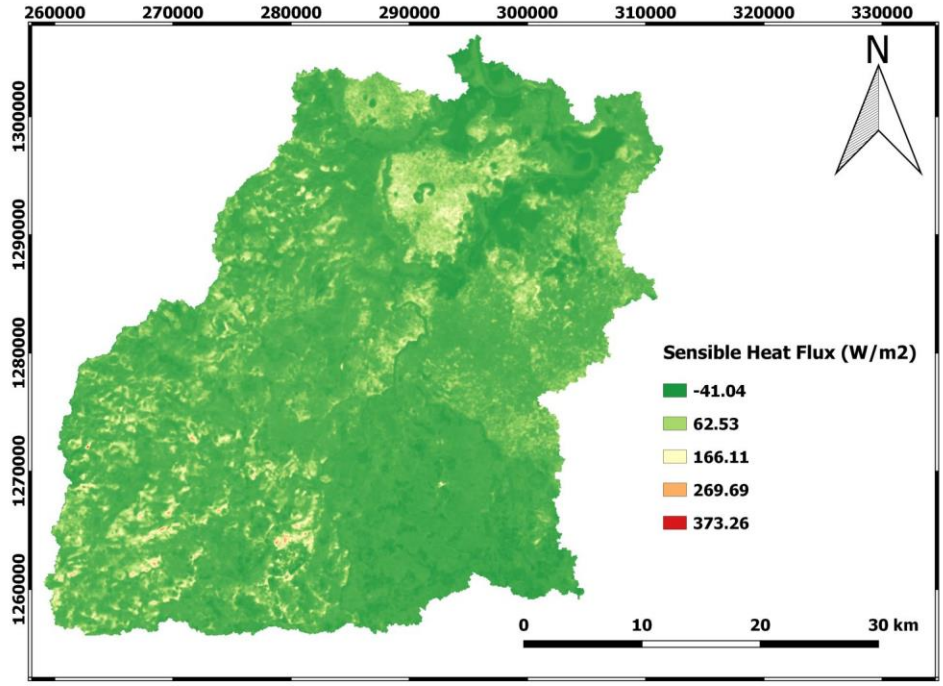

Figure 4.19: Map of sensible heat flux (H)

4.7.3. Latent Heat Flux (λET)

After the estimation of net radiation, soil heat flux and sensible heat, the instantaneous latent heat flux at the time of the satellite overpass was calculated as a residual term of the energy balance equation in W/m^2. The value of latent heat flux ranged from -84.20 to 708.26 W/m^2 for the study area on 23 December 2016 at the satellite overpass time. The map of latent heat flux is shown in Figure 4.20. Figure 4.21 shows latent heat flux for different land cover types. Hence, the mean value ranges from 423.53 to 599.44 W/m^2 for all land cover types of the study area.

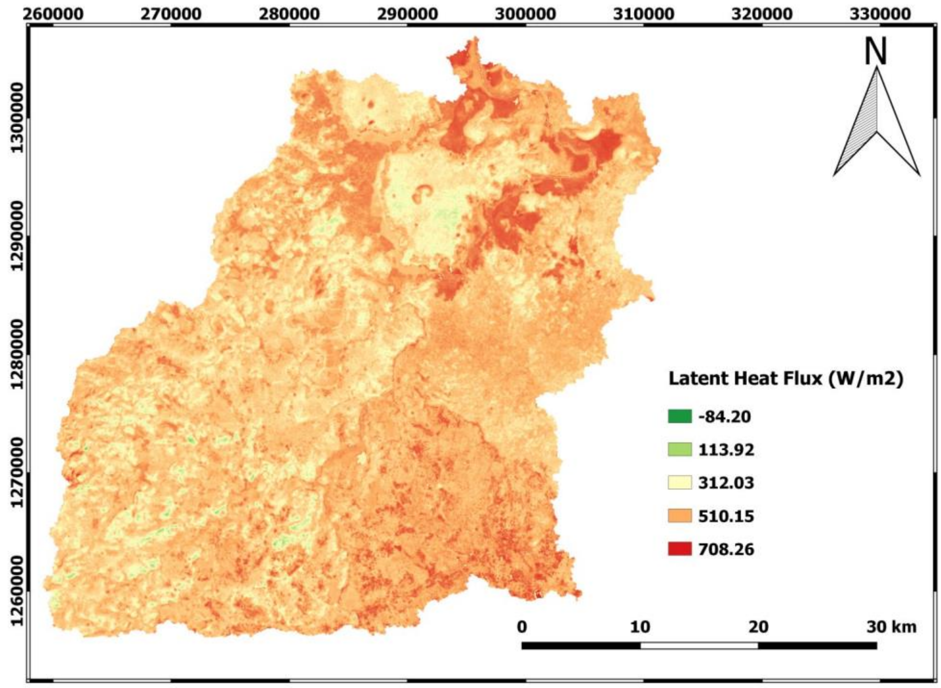

Figure 4.20: Map of Latent Heat Flux estimated as residual term of energy balance.

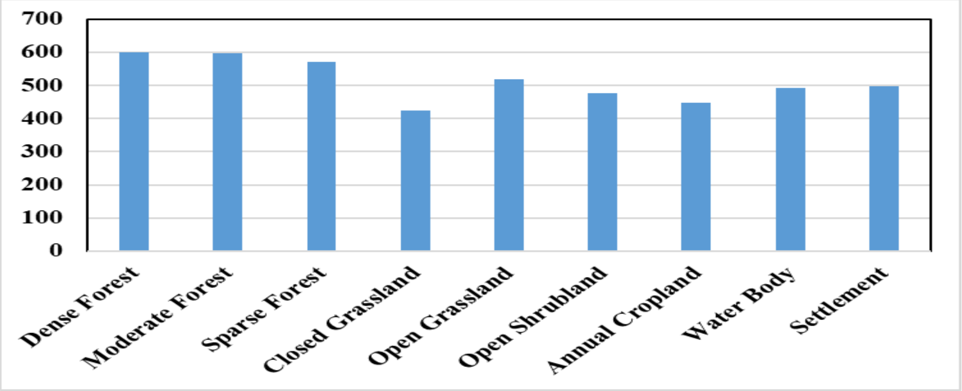

Figure 4.21: Graphical representation of mean latent heat flux for each land cover types

4.8. Instantaneous ET (ETinst) and Reference ET Fraction (ETrF)

After latent heat flux (λ) calculated, ETinst and reference ET fraction (ETrF) was calculated simultaneously at each pixel level for the image time. Figure 4.22 shows the results of ETinst (mm/hr) and ETrF for the day of 23 December 2016.

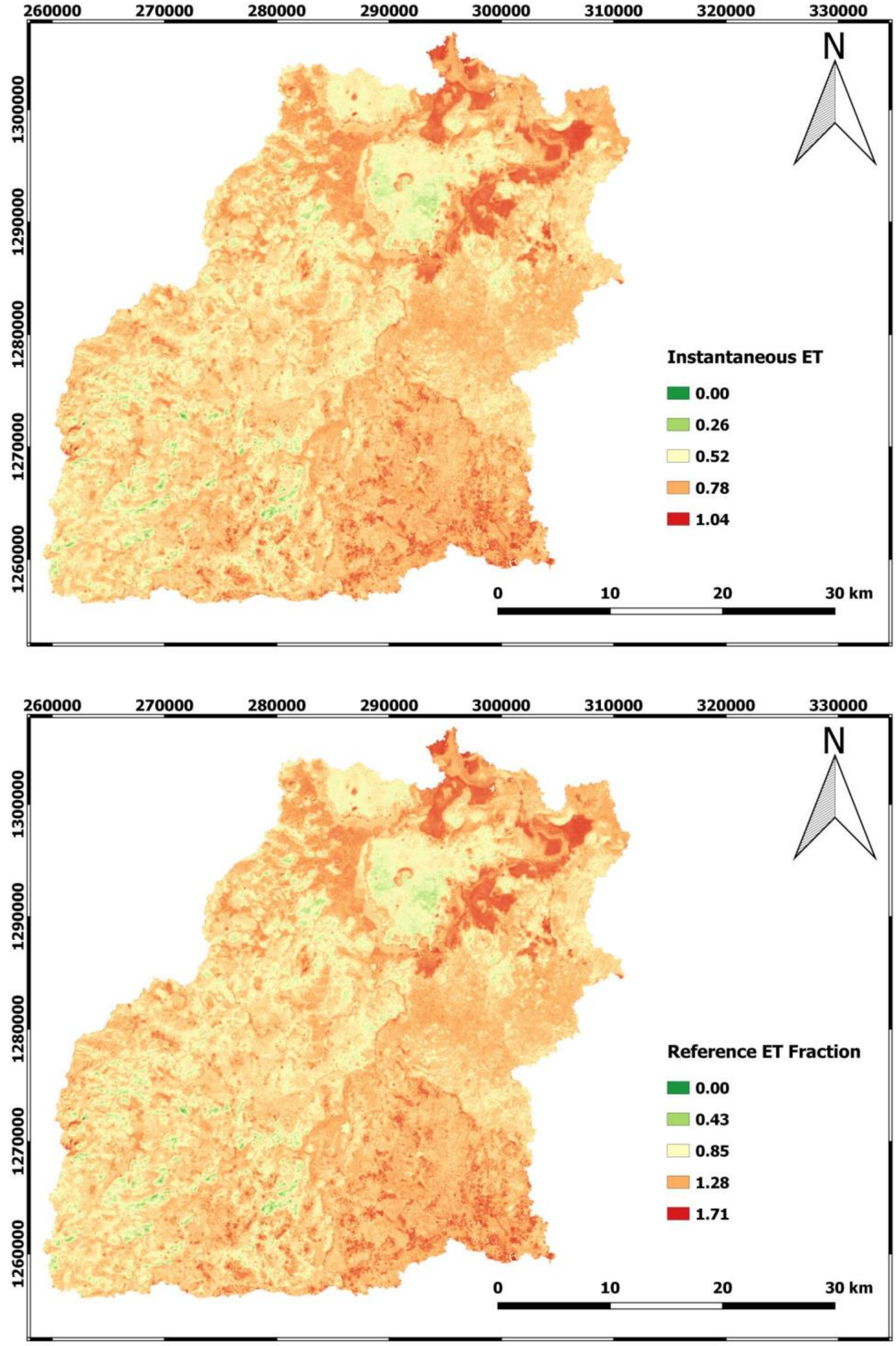

Figure 4.22: Map of Instantaneous ET and reference ET fraction

4.9. Daily Evapotranspiration (ET_{24})

Once the Instantaneous ET (ETinst) and Reference ET Fraction (ETrF) was developed, daily evapotranspiration calculation was made assuming that the instantaneous evaporation fraction (ETrF) values are the same as the 24-hour values. A large number of field studies

(Bastiaanssen et al., 1998) support this assumption. The daily evapotranspiration value ranged from 0 to 7.39 mm/day having the mean value 4.78 mm/day on 23 December 2016 and is shown in Figure 4.23. Mean values of ET for each land cover types of the study area are shown in the Table 4.3. Similar results have been found (2.88 mm/day and 3.3 mm/day) by Temesgen, (2009) for Dec and Jan respectively in Fogera floodplain, (Muhammed, 2012) estimates 0.78 mm/day for Mar in upper Gilgel abay catchment using SEBS model, (Ayalew, 2003) estimate 0.2 mm/day to 4.5 mm/day in Ethiopian rift and adjacent highlands from Thematic mapper satellite data using SEBAL, (Mulugeta et al., 2017) estimates 0.0 to 6.85 and 0.0-9.36 mm/day for Jan 25 and Feb 26 respectively using SEBAL algorism.

Variation of ET in mm/day in relation to NDVI and surface temperature in ^{0}C for the different land use system were compared and presented in Figure 4.26. From this figure, it can be noted that during satellite overpass time on December 23, 2016, water body was having high surface temperature of about 28.10 ^{0}C and the estimated ET from the same land use was mainly contributed from evaporation, which is about 5.13 mm/day. On the other hand, forest area shows average surface temperature of 28.27 ^{0}C with high vegetation index (0.61) and mean ET value (6.15 mm/day).

Figure 4.24 shows images of twenty-four hour ET as computed by SEBAL for the same study area in different months of 2016 (Dec 23, Jan 22, Feb 07 and Mar 10). The maximum estimated actual evapotranspiration over the whole catchment ranged from 6.51 mm/day (Jan) to 7.82 mm/day (Mar). The mean actual evapotranspiration ranged from 4.37 mm/day (Feb) to 4.78 mm/day (Dec). Table 4.4 and Figure 4.25 shows the area coverage for each month and twenty-four hour evapotranspiration. Most of the area coverage (an average of 76.76%) received 4 to 7 mm/day for each months.

The daily ET map for December 23 2016 image and land use/land cover map of 2015 is shown in Figure 4.23. The figure clearly indicates that daily ET is nearly the same as the average ET in annual cropland (88.49%), higher in the forestland cover types and lower in closed grassland cover type Table 4.3.

Figure 4.27 shows both daily ET (mm/day) and ETinst (mm/hr) have the same trend for each land cover types.

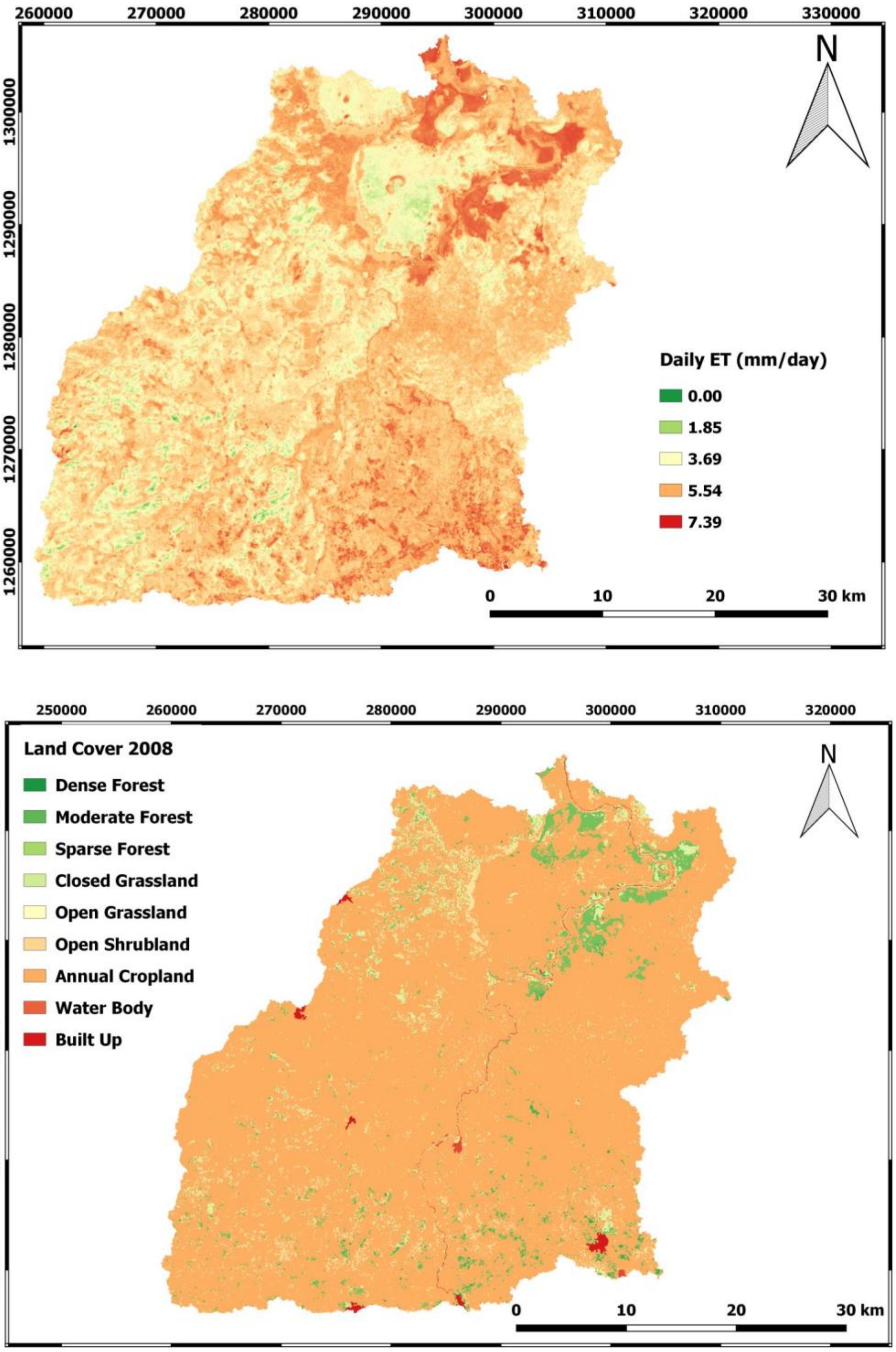

Figure 4.23: Map of Daily Evapotranspiration and land use/land cover of the study area

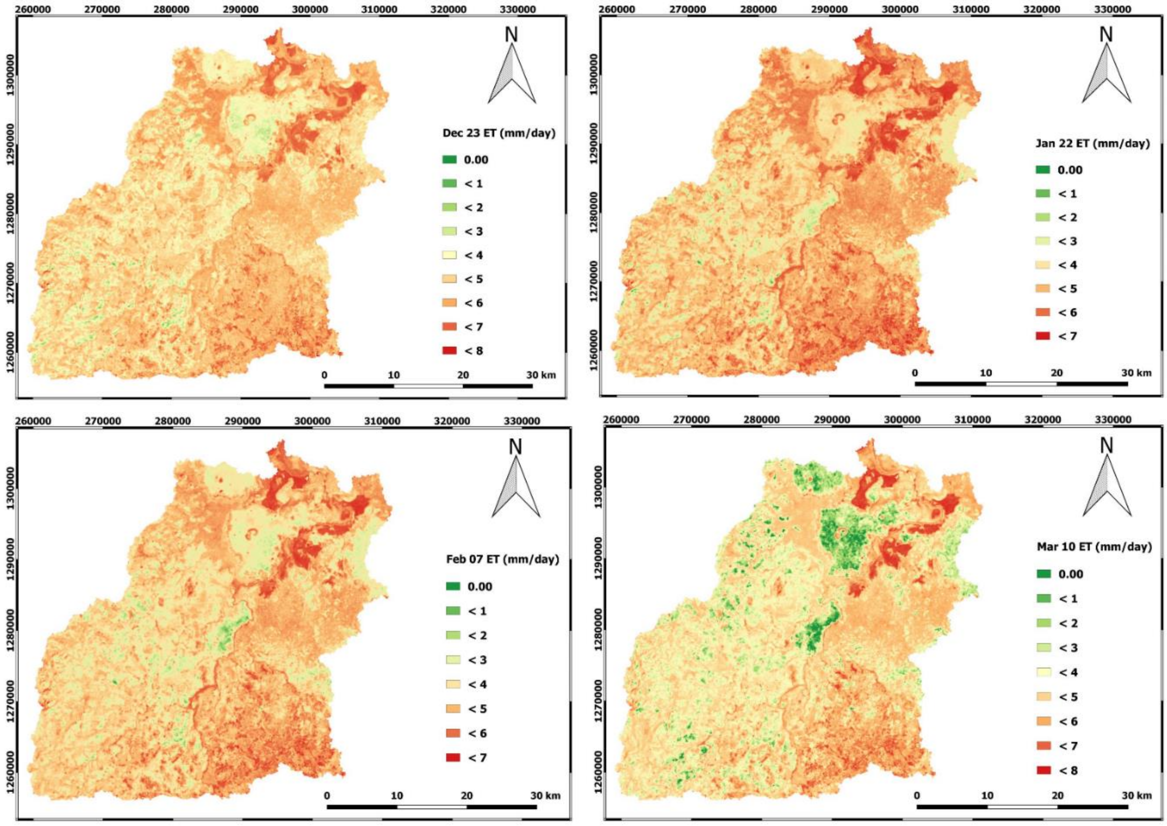

Figure 4.24: Map of Twenty-Four hour evapotranspiration for four months

Table 4.3: Dec 23/2016 daily evapotranspiration (mm/day) distribution for different land cover type

ID	Land Cover Type	Area (km2)	%	Daily ET (mm/day)				
				Min	Max	Range	Mean	STD
1	Dense Forest	0.22	0.01	4.82	7.00	2.18	6.25	0.38
2	Moderate Forest	6.33	0.37	0.64	7.09	6.45	6.23	0.46
3	Sparse Forest	68.41	3.99	1.14	7.00	5.86	5.97	0.50
4	Closed Grassland	0.51	0.03	2.51	5.89	3.38	4.42	0.50
5	Open Grassland	49.43	2.88	0.63	7.17	6.55	5.42	0.77
6	Open Shrub land	61.67	3.60	0.27	6.81	6.54	4.96	0.62
7	Annual Cropland	1,516.57	88.49	0.00	7.09	7.09	4.69	0.73
8	Water Body	5.99	0.35	3.25	7.39	4.14	5.13	1.15
9	Settlement	4.72	0.28	3.17	6.69	3.52	5.20	0.51

Table 4.4: Daily evapotranspiration distribution and its area coverage for selected months

Daily ET (mm/Day)	Dec-23-2016		Jan-22-2016		Feb-07-2016		Mar-10-2016		Average	
	Area (km2)	% tage	Area (km2)	% tage	Area (km2)	% tage	Area (km2)	% tage	Area (km2)	% tage
1	22.75	1.31	19.53	1.12	21.52	1.24	40.06	2.30	25.97	1.49
2	85.26	4.90	75.57	4.34	84.51	4.86	83.55	4.80	82.22	4.73
3	174.68	10.04	155.76	8.95	170.81	9.82	154.56	8.88	163.95	9.42
4	266.17	15.30	249.50	14.34	258.35	14.85	274.72	15.79	262.18	15.07
5	366.90	21.09	371.67	21.37	356.36	20.48	414.78	23.84	377.43	21.70
6	390.53	22.45	386.29	22.21	392.53	22.56	419.95	24.14	397.32	22.84
7	299.48	17.22	325.09	18.69	316.39	18.19	252.77	14.53	298.43	17.16
8	133.85	7.69	156.20	8.98	139.15	8.00	99.21	5.70	132.10	7.59

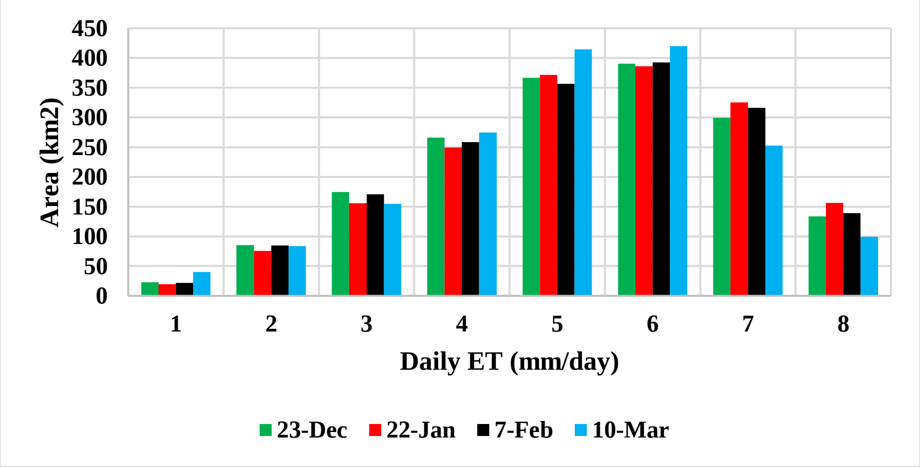

Figure 4.25: Daily Evapotranspiration distribution (Dec 23, Jan 22, Feb 07 and Mar 10)

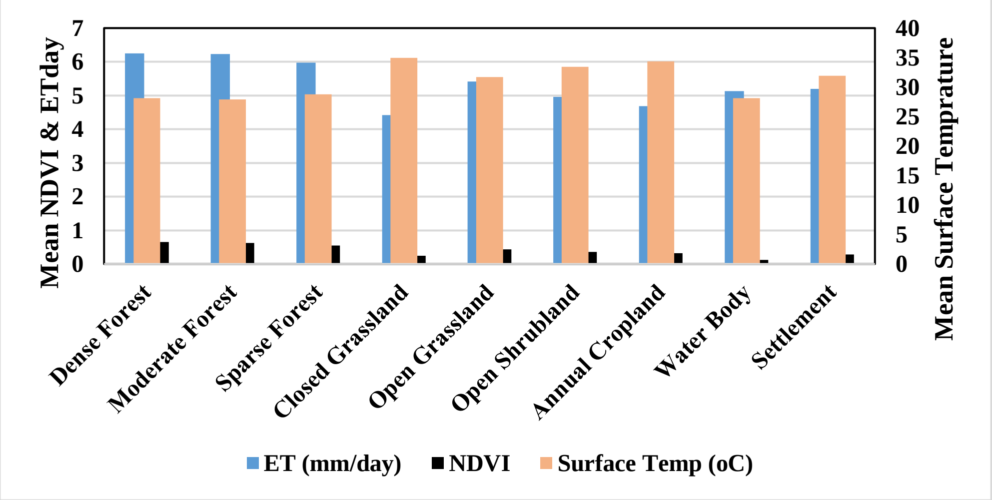

Figure 4.26: Comparison between ET, NDVI & Surface temperature (Ts) during satellite overpass time.

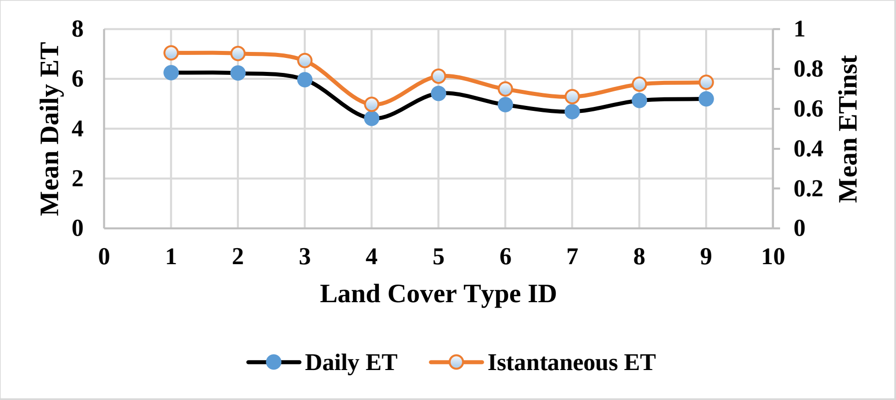

Figure 4.27: Daily ET and instantaneous ET distribution

4.10. Seasonal Evapotranspiration

A cumulative evapotranspiration map can be derived from the 24-hour evapotranspiration maps with a set of weather data.

The concept of this method is to expand 24-hour evapotranspiration proportionally to the reference evapotranspiration, where the reference evapotranspiration is derived from weather data. The assumption made is that the ET for the entire image area changes in proportion to the change in the reference ET at the index weather site.

The first step in computing season ET is to determine the period represented by each ET image. In this case, the December 23rd image was assigned to represent December, the January 22nd image to represent January, the February 7th image to represent February, and the March 10th image to represent March of 2016.

The second step in the cumulative ET process is computing reference evapotranspiration (ETr) for the period represented by each image. The ETr data for this study were calculated using REF-ET software. The values for ETr are summarized in Table 4.5.

Table 4.5: Values reference ET, ETr and cumulative ETr for the study area in 2016

Date	**23-Dec**	**22-Jan**	**7-Feb**	**10-Mar**
Cumulative ETr for the month (mm) from REF-ET software	117.74	111.04	125.52	159.6
ETr on image date (mm)	4.35	3.6	4.13	5.27

The third step is computing the value for multiplier (Km) for each period. Km is used to convert ET for the day of the image into ET for the month. For 2016, the values of Km used are summarized in Table 4.6.

Table 4.6: Values computed for Km, for the study area in 2016

Period	Dec 1-31	Jan 1-31	Feb 1-29	Mar 1-31
K_m	27.07	30.84	30.39	30.28

Seasonal ET is estimated on a monthly or four-month basis (December, January, February and March). The total seasonal ET is estimated by summing up ET from all periods (selected months). A seasonal ET map is prepared for a year 2016 selected months of the study area are presented in Figure 4.28 below. As Table 4.7 describes, the mean maximum ET (mm) was found in forestland cover type but it covers low area (4.37%). The maximum area coverage (88.49 km^2) produces the minimum ET (528.08 mm). The value of the study area form this selected month was found 537.92 mm for 2016.

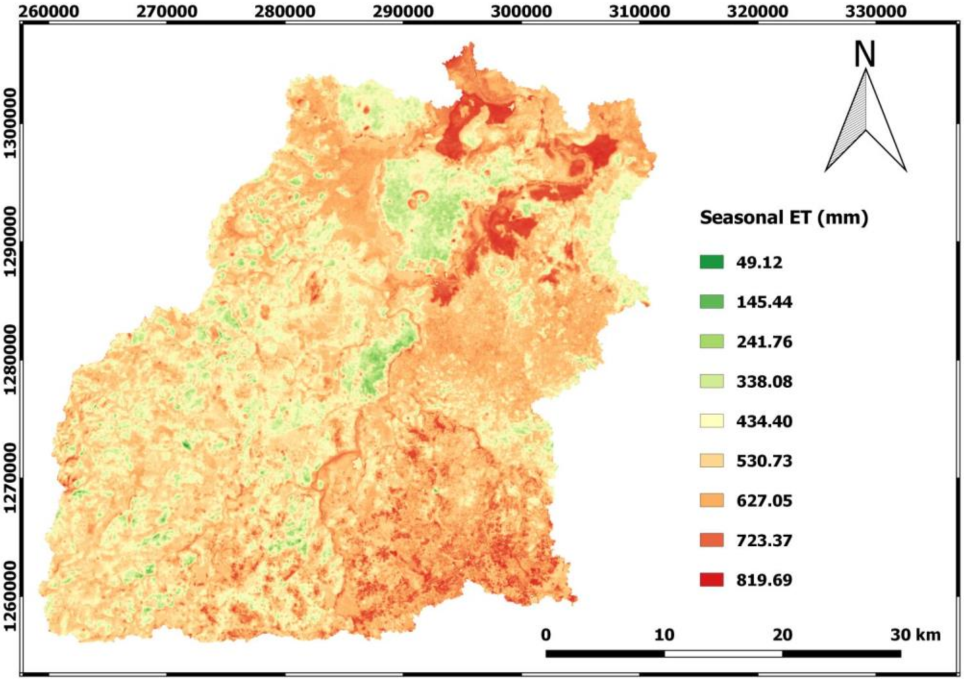

Figure 4.28: An image showing ET for the period December to March 2016 of the study area.

Table 4.7: Seasonal ET distribution and its area coverage for each land use type.

ID	Land Cover Type	Area (km2)	%	Min ET(mm)	Max ET(mm)	Range	Mean ET(mm)	STD
1	Dense Forest	0.22	0.01	587.52	812.40	224.88	732.88	43.97
2	Moderate Forest	6.33	0.37	424.14	812.58	388.44	729.33	48.57
3	Sparse Forest	68.41	3.99	411.27	817.96	406.69	693.85	68.77
4	Closed Grassland	0.51	0.03	308.07	639.72	331.65	527.66	48.88
5	Open Grassland	49.43	2.88	114.77	819.69	704.92	612.09	90.21
6	Open Shrub land	61.67	3.60	152.77	781.97	629.19	556.12	78.25
7	Annual Cropland	1,516.57	88.49	49.12	804.21	755.09	528.08	95.65
8	Water Body	5.99	0.35	401.29	802.78	401.48	618.61	104.84
9	Settlement	4.72	0.28	393.08	785.80	392.71	612.76	60.42

4.11. Comparison of ground based evapotranspiration estimation methods with SEBAL

The different conventional methods were computed using REF-ET software Table 4.8.

Table 4.8: ETo results for different conventional methods

Name	ASCE st Penman Monteith (mm/h)	FAO 56 Penman Monteith (mm/h)	1996 Kimberly penman (mm/h)	1972 Kimberly penman (mm/h)	1948 Penman (mm/h)	CIMIS Pen penman (mm/h)	1985 Hargreaves and Samani (mm/h)	Priestly-Taylor (mm/h)	1957 Makkink (mm/h)	1961 Turc (mm/h)
ETo	**4.33**	**4.05**	**3.62**	**4.11**	**5.07**	**4.96**	**1.24**	**4.35**	**3.64**	**5.18**

From Table 4.8, the value for standard P-M (4.33 mm/hr) for the weather station used as a reference to compare the value obtained from other conventional methods as well as SEBAL method. Hence, the mean value of the study area from SEBAL calculation was 4.78 mm/hr and this result approached to CIMIS penman, standard P-M and Priestly Taylor methods. Provided that, estimation of ET from SEBAL would be practically applicable for future use.

Currently, we used empirical models to compute ET. However, estimation of ET from empirical models provide point data for a certain location near to the weather station. Hence, it is impractical and this value doesn’t represent the area of interest because the value of ET is not the same in space and time. Therefore, to overcome this problem an efficient, accurate, and inexpensive procedures from remote sensing based approach would be used. Predicting and proper quantification of the actual evaporation fluxes through a remote sensing approach would provide spatial as well as temporal distribution of ET from irrigated lands throughout a growing season is important for maximizing the agricultural production and improve water balance.

5. Conclusion and Recommendations

The main objective of this study was estimation of evapotranspiration using Surface Energy Balance Algorism for Land (SEBAL) over lower Gilgel Abay. To perform this operation Landsat 8 and ASTER Global DEM from USGS and land use land cover map of 2008 schema II from www.geoportal.rcmrd.org products were used as remote sensing data. For ground-based data, Bahir Dar automatic weather station data and SEBAL GRASS Master Python file also used.

Landsat 8 data including MTL file and reflectance of each band, DEM in the form MDT_Sebal, shape file of the study area and SEBAL_GRASS-Master file were organized in the same folder to perform the operation using GRASS-GIS.

Ground based data were used to calculate instantaneous value of reference evapotranspiration from weather station for the time of satellite overpass in (mm), wind speed value for height at 2 m and daily value of reference evapotranspiration using REF-ET software at the weather station.

The actual evapotranspiration (ET) was estimated using SEBAL model through surface radiation balance and energy budget equations displayed in the above equations. This is accomplished in a serious of steps using GRASS GIS environment.

Using land use/land cover Figure 3.5, the pattern and behaviour of land surface interaction with solar radiation elements are carried out. The majority of the land cover which is controlling the solar radiation and ET regime is represented by annual crop land with coverage of 88.49% of the total area, followed by sparse forest covers about 4% and the remain land cover types with 11.51% of the total area coverage. The variation of ET for the daily ET varied from 0 to 6.26 mm/day at the same land cover classes.

The spatial variation of the main solar radiation elements is analysed. The principle statistic measurements i.e., minimum, maximum, mean, range and standard deviation values are used to give indications about the characteristics of land cover classes. Mean values are the most important statistic parameters, which reflect the characteristics of most pixels that are controlling the solar radiations behaviour within each class of land cover.

The reason SEBAL would be suitable to estimate ET on hourly basis and not suitable on daily basis could be due to the use of ETrF in extrapolating instantaneous ET to daily values.

The extrapolation assumes that the ETrF at the time of satellite overpass remains constant throughout the day.

Similar assumptions were followed for seasonal ET estimation with that of the 24-hour ET estimation for a certain time period between images. The assumption is not always true, especially if a time period represented by one satellite image is long, one should estimate seasonal ET using the most satellite images possible like MODIS image products.

The results of this study suggested that the SEBAL model can be applied in our country to quantify the actual ET from irrigated agriculture. Hence, SEBAL model can be useful in irrigation water use related studies in the future in the absence of ground data.

References

Al Zayed, I., Elagib, N., Ribbe, L., & Heinrich, J. (2016). Satellite-based evapotranspiration over Gezira Irrigation Scheme, Sudan: A comparative study. Agricultural Water Management, 66-76.

Allen, G., R., Pereira, L., R., D., Smith, a., & M. (1998). Crop Evapotranspiration. Food and Agriculture Organization of the United Nations, Rome, Italy, ISBN 92-5-104219-5, 290.

Allen, R. (2000). REF-ET: Reference Evapotranspiration Calculation Software for FAO and ASCE Standardized Equations. University of Idaho, 47.

Allen, R., Irmak, A., Trezza, R., Hendrickx, J., Bastiaanssen, W., & Kjaersgaard, J. (2011). Satellite-based ET estimation in agriculture using SEBAL and METRIC. Hydrological Processes, 4011-4027.

Allen, R., Pereira, G., Raes, L., & Smith, D. (1998). Crop Evapotranspiration. Food and Agriculture Organization of the United Nations, Rome, Italy, ISBN 92-5-104219-5, 290.

Allen, R., Pereira, L., Raes, D., & Smith, M. (1990). Crop Evapotranspiration (guidelines for computing crop water requirements). Rome: FAO Irrigation and Drainage Paper No. 56.

Allen, R., Tasumi, M., & Morse, A. (2005). Satellite-based evapotranspiration by METRIC and Landsat for western states water management. Presented at the US Bureau of Reclamation Evapotranspiration Workshop, Ft. Collins, CO, USA.

Allen, R., Tasumi, M., & Trezza, R. (2007). Satellite-based energy balance for mapping evapotranspiration with internalized calibration (METRIC)-model. J. Irrig. Drain. E ASCE, 133, 380–394.

Allen, R., Walter, G., Elliot, I., Howell, R., Itenfsu, T., Jensen, D., & Snyder, M. (2005). The ASCE standardized reference evapotranspiration equation. ASCE and American Society of Civil Engineers.

Almhab, A., & Busu, L. (2008). Estimation of Evapotranspiration with modified SEBAL model using Landsat-TM and NOAA-AVHRR images in arid mountains area. 2nd Asia International Conference on Modelling and Simulation, AMS 2008, (pp. 350-355).

Ayad, A. F., Ahmed, H. A.-S., Adrian, O., Anna, J., & Adriana, M. (2016). Estimation of Evapotranspiration Using SEBAL Algorithm and Landsat-8 Data—A Case Study: Tatra Mountains Region. Geological Resource and Engineering 6, 257-270.

Ayalew, T. (2003). Evapotranspiration estimation using thematic mapper spectral satellite data in the Ethiopian rift and adjacent highlands. Hydrology 279, 83-93.

Ayoub, A. A. (2009). Estimation Of Regional Evapotranspiration Using Remote Sensing Data In Arid Areas. Faculty of Geoinformation Science and Engineering Universiti Teknologi Malaysia The thesis for degree of Doctor of Philosophy (Remote Sensing), 1-2.

Bashir, M., Hata, T., Abdelhadi, A., & Tanakamaru, H. (2006). Satellite-Based Evapotranspiration and Crop Coefficient for Irrigated Sorghum in the Gezira Scheme, Sudan. Hydrology and Earth System Sciences Discussions 3:, 793-817.

Bastiaanssen, W. (1995). Regionalization of surface flux densities and moisture indicators in composite terrain. Ph.D. Thesis. The Netherlands: Wageningen Agricultural University, Wageningen.

Bastiaanssen, W. (2000). SEBAL-based sensible and latent heat fluxes in the irrigated Gediz Basin,Turkey. J. Hydrol, 229, 87–100.

Bastiaanssen, W., Menenti, M., Feddes, R., & Holtslag, A. (1998). A remote sensing surface energy balance algorithm for land (SEBAL): 1. Formulation. J. Hydrology, 212-213, p. 198-212.

Bastiaanssen, W., Noordman, E., Pelgrum, H., Davids, G., Thoreson, B., & Allen, R. (2005). SEBAL model with remotely sensed data to improve water-resources management under actual field conditions. J. Irrig. Drain. E ASCE, 131, 85–93.

Bastiaanssen, W., Pelgrum, H., Wang, J., Ma, Y., Moreno, J., Roerink, G., & val der Wal, T. (1998). “A Remote Sensing Surface Energy Balance Algorithm for Land (SEBAL): Part 2: Validation”. Journal of Hydrology 212:, 213-29.

BCEOM. (1998). Abay River Basin Integrated Development Master Plan-Phase 2 – Data collection Site investigation survey and analysis section II Volume I (part 1 Geology). Ministry of Water Resources, Addis Ababa.

Chander, G., & Markham, B. (2003). “Revised Landsat-5 TM Radiometric Calibration Procedures and Postcalibration Dynamic Ranges.”. Geoscience and Remote Sensing, IEEE Transactions 41, 2674-7.

Chen, D., & Xu, C. (2005). Comparison of seven models for estimation of evapotranspiration and groundwater recharge using lysimeter measurement data in Germany. Hydrol. Process, 19, 3717–3734.

Choudhury, B. (1989). Estimating evaporation and carbon assimilation using infrared temperature data: vistas in modeling. In Theory and Applications of Optical Remote Sensing; Asrar, G., Ed.; Wiley: New York, NY, USA, pp. 628–690.

Choudhury, B., & Menenti, M. (1993). Parameterization of Land Surface Evaporation by means of Location Dependent Potential Evaporation and Surface Temperature Range. Department for Environment, Food and Rural Affairs (Defra) London, UK, Volume 212, pp. 561–568.

Compaoré, H., Hendrickx, a. M., Hong, S. h., Friesen, J., van de Giesen, N., Rodgers, C., . . . Vlek, P. (2008). Evaporation mapping at two scales using optical imagery in the White Volta Basin, Upper East Ghana. Physics and Chemistry of the Earth, 127-140.

Dile, Y. T., Berndtsson, R., & Setegn, S. G. (2013). Hydrological Response to Climate Change for Gilgel Abay River, in the Lake Tana Basin - Upper Blue Nile Basin of Ethiopia. PLoS ONE 8(10), e79296. doi: 10.1371/journal.pone.0079296.

Dingman, S. (2002). Physical hydrology. Upper Saddle River,. Prentice Hall,, 646 pp.

Duffie, J., & Beckman, &. W. (1980). “Solar Engineering of Thermal Processes.”. John Wiley and Sons, New York, 1-109.

EMA. (1981). Meterlogical Report. Addis Abeba, Ethiopia: Ethiopian Meterological Agency.

FAO, F. A. (1993). THE STATE OF FOOD AND AGRICULTURE. Rome, Italy: (FAO Agriculture Series, no. 26).

Gao , Y., Long, D., & Li, Z. (2008). Estimation of daily actual evapotranspiration from remotely sensed data under complex terrain over the upper Chao river basin in North China. Int. J. Remote Sens, 29, 3295–3315.

Gao, Y., & Long, D. (2008). Intercomparison of remote sensing-based models for estimation of evapotranspiration and accuracy assessment based on SWAT. Hydrol. Process, 22, 4850–4869.

Getachew, T. D. (2014). Watershed Modeling of Gilgel Abay River Using SWAT.

GRASS Development Team. (1997). Retrieved from http://grass.osgeo.org

Hafeez, M., Chemin, Y., Van De Giesen, N., & Bouman, B. (2002). Field evapotranspiration estimation in Central Luzon, Philippines, using different sensors: Landsat 7 ETM+, Terra MODIS and ASTER. Symposium on Geospatial Theory Processing and Applications, 7.

Hailegiorgis, W. S. (2006). “Remote Sensing Analysis of Summer Time Evapotranspiration Using SEBS Algorithm.”. ITC, Enschede.

Hamimed, A., Khaldi, A., Mederbal, K., & Seddini, A. (2009). Estimation of daily actual evapotranspiration in Algerian semiarid environment with satellite ASTER. Remote Sensing for a Changing Europe, 448-459.

Hong, S., Hendrickx, J., & Borchers, B. (2009). Up-scaling of SEBAL derived evapotranspiration maps from Landsat (30 m) to MODIS (250 m) scale. Journal of Hydrology, 122-138.

Irmak, A., Martin, D., Koelliker, J., & Eisenhauer, D. (2006a). Modeling the effects of terracing on water supplies in the Medicine Creek, Nebraska. ASABE Annual Int. Meetings, Portland, Ore., Paper No. 062291.

Irmak, S., Payero, J., Martin, D., Irmak, A., & Howell, T. (2006b). Sensitivity analyses and sensitivity coefficients of the standardized ASCE-Penman-Monteith equation to climate variables. Irrig. Drain. Eng., 1326, 564–578.

Jaber, H., Mansor, S., Pradhan, B., & Ahmad, N. (2016). Evaluation of SEBAL model for Evapotranspiration mapping in Iraq using remote sensing and GIS. International Journal of Applied Engineering Research, 3950-3955.

Jackson, R., Idso, S., Reginato, R., & Pinter, P. (1981). Canopy temperature as a crop water stress indicator. Water Resour. Res, 17, 1133–1138.

Jensen, E., Burman, D., & R. Allen, G. (1990). Evapotranspiration and Irrigation Water Requirements. American Society of Civil Engineers, New York.: ASCE Manuals and Reports on Engineering Practice No. 70.

Kahsay, B. (2004). Land use and land cover change in central high lands of Ethiopia. MSc research paper. Addis Ababa University, Ethiopia.

Kebede, E. W. (2009). Hydrological responses to land cover changes in Gilgel Abbay catchment, Ethiopia. Enschede, ITC.

Kimura, R., Bai, L., Fan, J., Takayama, N., & Hinokidani, O. (2007). Evapo-transpiration estimation over the river basin of the Loess Plateau of China based on remote sensing. Journal of Arid Environments, 53-65.

Kosa, P. (2011). The Effect of Temperature on Actual Evapotranspiration Based on Landsat-5 TM Satellite Imagery. INTECH Open Access Publisher.

Li, Z., Liu, X., Ma, T., Kejia, D., Zhou, Q., Yao, B., & Niu, T. (2013). Retrieval of the surface evapotranspiration patterns in the alpine grassland-wetland ecosystem applying SEBAL model in the source region of the Yellow River, China. Ecological Modelling, 64-75.

Lillesand, M., Kiefer, W., & Chipman, W. (2004). Remote Sensing and Image Interpretation. John Wiley & Sons Ltd.

Long, D., & Singh, V. (2012). A modified surface energy balance algorithm for land (M-SEBAL) based on a trapezoidal framework. Water Resoures.

Long, D., & Singh, V. (2013). Assessing the impact of end-member selection on the accuracy of satellite-based spatial variability models for actual evapotranspiration estimation. Water Resour.Res, 49, 2601–2618.

Long, D., Singh, V., & Li, Z. (2011). How sensitive is SEBAL to changes in input variables, domain size and satellite sensor? J. Geography. Res. Atmos., 116.

Martin, S., Dirk, R., Luis S., P., & Richard G, A. (2000). Crop Evapotranspiration (guidelines for computing crop water requirements) FAO Irrigation and Drainage Paper 56. Rome, Italy.

Mather, P., & Tso, B. (2009). Classification Methods for Remotely Sensed Data. CRC press.

McCabe, M., & Wood, E. (2006). Scale influences on the remote estimation of evapotranspiration using multiple satellite sensors. Remote Sens. Environ, 105, 271–285.

Merlin, O., Chirouze, J., Olioso, A., Jarlan, L., Chehbouni, G., & Boulet, G. (2014). “An Image-Based Four-Source Surface Energy Balance Model to Estimate Crop Evapotranspiration from Solar Reflectance/Thermal Emission Data (SEB-4S).”. Agricultural and Forest Meteorology 184:, 188-203.

Moran, M., Jackson, R., Slater, P., & Teillet, P. (1992). Evaluation of simplified procedures for retrieval of land surface reflectance factors from satellite sensor output. Remote Sensing of Environment, 41, 169-184.

Morse, A., Allen, R., Tasumi, M., Kramber, W., Trezza, R., & Wright, L. (2001). Application of the SEBAL Methodology for Estimating Evapotranspiration and Consumptive Use of Water through Remote Sensing. Idaho: Idaho Department of Water Resources.

Muhammed, A. H. (2012). Satellite based evapotranspiration estimation and runoff simulation: a topmodel application to the gilgel abay catchment, Ethiopia. Enschede, The Netherlands.

Mulugeta, G., Tena, A., Gabriel, S., & Mekonnen, G. (2017). Remote Sensing Based Estimation of Evapo-Transpiration Using Selected Algorithms: The Case of Wonji Shoa Sugar Cane Estate, Ethiopia. Sensors and Sensor Networks, Vol. 5, No. 1, 1-13.

Norman, J., Divakarla, M., & Goel, N. (1995). Algorithms for extracting information from remote thermal-IR observations of the earth's surface. Remote Sensing of Environment, 51(1), 157-168.

Oberg, W., & Melesss, A. M. (2006). Evapotranspiration Dynamics at an Eco-hydrological Restoration Site: An Energy Balance and Remote Sensing Approach. In Wiley Online Library.

Opoku Duah, S., Donoghue, N. M., & Burt, T. (2008). Intercomparison of Evapotranspiration over the Savannah Volta Basin in West Africa Using Remote Sensing Data. Sensors 8, 2736-61.

Paulson, C. (1970). The mathematical representation of wind speed and temperature profiles in the unstable atmospheric surface layer. Appl. Meteorol. 9, 857-861.

Ramesh , S. K., Ayse , I., Suat, I., & Martin, D. L. (2008). Application of SEBAL Model for Mapping Evapotranspiration and Estimating Surface Energy Fluxes in South-Central Nebraska. Journal of Irrigation and Drainage Engineering.

RCMRD. (2015, April 8). The Regional Centre for Mapping of Resources for Development. Retrieved from http://geoportal.rcmrd.org: http://geoportal.rcmrd.org

Roerink, G., Su, Z., & Menenti, M. (2000). S-SEBI: A simple remote sensing algorithm to estimate the surface energy balance. Phys. Chem. Earth B, 25, 147–157.

Ruhoff, A., Paz, A., Collischonn, W., Aragao, L., Rocha, H., & Malhi, Y. (2012). A MODIS-Based Energy Balance to Estimate Evapotranspiration for Clear-Sky Days in Brazilian Tropical Savannas. Remote Sensing, 703-725.

Setegn, S. G., Ragahavan, S., Bijan, D., & Melesse, A. (2009). Spatial delination of soil erosion vulnerability in the lake Tana Basin. Wiley InterScience.

Smith, R. B. (2010). The Heat Budget of the Earth’s Surface Deduced from Space. Retrieved from http://www.yale.edu/ceo/Documentation/Surface_Heat_Budget_From_Space.pdf.

Spiliotopoulos, M., Adaktylou, N., Loukas, A., Michalopoulou, H., Mylopoulos, N., & Toulios, L. (2013). A spatial downscaling procedure of MODIS derived actual evapotranspiration using Landsat images at central Greece. First International Conference on Remote Sensing and Geoinformation of Environment, 879508.

Su, Z. (2001). A Surface Energy Balance System (SEBS) for estimation of turbulent heat fluxes from point to continental scale. In Advanced Earth Observation—Land Surface Climate; Su, Z.,Jacobs, J., Eds. Publications of the National Remote Sensing Board (BCRS): Delft, The Netherlands, Volume 01–02, pp. 91–108.

Su, Z. (2002). The Surface Energy Balance System (SEBS) for estimation of turbulent heat fluxes. Hydrology and Earth System Sciences, 6(1), 85-99.

Su, Z. (2005). Hydrological applications of remote sensing. Surface fluxes and other derived variables surface energy balance. In Encyclopedia of Hydrological Sciences; Anderson, M., Ed.; John Wiley and Sons: Hoboken, NJ, USA.

Su, Z., Li, X., Zhou, Y., Wan, L., Wen, J., & Sinton, K. (2003). Estimating areal evaporation from remote sensing. Proc. IEEE Int, 2, 1166–1168.

Sun, Z., Wei, B., Su, W., Shen, W., Wang, C., You, D., & Liu, Z. (2011). Evapotranspiration estimation based on the SEBAL model in the Nansi Lake Wetland of China. Mathematical and Computer Modelling, 1086-1092.

Tasumi, M., Allen, R. G., & Trezza, R. (2008). At-Surface Reflectance and Albedo from Satellite for Operational Calculation of Land Surface Energy Balance. Hydrologic Engineering 13, 51-63.

Tasumi, M., Trezza, R., Allen, R., & Wright, J. (2005). Operational aspects of satellite-based energy balance models for irrigated crops in the semi-arid U.S. Irrigation and Drainage Systems, 355-376.

Tasumi, M., Trezza, R., Allen, R., & Wright, L. (2003). US Validation Tests on the SEBAL Model for Evapotranspiration via Satellite. In Proceedings of 54th IEC Meeting of the International Commission on Irrigation and Drainage (ICID) Workshop. Remote Sensing of ET for Large Regions.

Temesgen, E. (2009). Estimation of Evapotranspiration from Satellite Remote Sensing and Meteorological Data over the Fogera Flood Plain - Ethiopia. A thesis for the degree of Master of Science in Geo-information Science and Earth Observation The Netherlands, 13.

Tessema, S. (2006). Assessment of temporal hydrological variations due to land use changes using remote sensing/GIS: a case study of Lake Tana Basin, Master Thesis, . KTH, Sweden.

Timmermans, W. (2007). An intercomparison of the Surface Energy Balance Algorithm for Land (SEBAL) and the Two-Source Energy Balance (TSEB) modeling schemes. Remote Sensing of Environment, 108(4), pp.369–384.

Timmermans, W., & Meijerink, A. (1999). Remotely sensed actual evapotranspiration: implications for groundwater management in Botswana. International Journal of Applied Earth Observation and Geoinformation, 222-233.

Trezza, R., Allen, R., & Tasumi, M. (2013). “Estimation of Actual Evapotranspiration along the Middle Rio Grande of New Mexico Using MODIS and Landsat Imagery with the METRIC Model”. Remote Sensing 5:, 5397-423.

USGS. (2013). Landsat-8 Exoatmospheric Irradiance ESUN Values http://www.gisagmaps. Retrieved from ” Available at http://www.gisagmaps.: http://www.gisagmaps.

Wagner, W. (2016, November 17).Retrieved from https://github.com/wwolff7/SEBAL

Wagner, W. (Director). (2017). Treino GIS / SEBAL 5 [Motion Picture].

Wang, J., Sammis, T., Gutschick, V., Gebremichael, M., & Miller, D. (2009). Sensitivity analisis of the surface energy balance algorithm for land (SEBAL). American Society of Agricultural and Biological Engineers, 801-811.

Waters, R., Allen, R., Bastiaanssen, W., Tasumi, M., & Trezza, R. (2002). "Surface Energy Balance Algorithms for Land. Idaho Implementation" Advanced Training and Users Manual. Idaho, USA.

Webb, E. (1970). Profile relationships: the log-linear range, and extension to strong stability. Quart. J. Roy. Meteorol. Soc. 96, 67-90.

Weng, Q., Lu, D., & Schubring, J. (2004). Estimation of Land Surface Temperature–Vegetation Abundance Relationship for Urban Heat Island Studies. Remote Sensing of Environment 89, 467-83.

Yang, Y., Shang, S., & Jiang, L. (2012). Remote sensing temporal and spatial patterns of evapotranspiration and the responses to water management in a large irrigation district of North China. Agricultural and Forest Meteorology, 112-122.

Yuei-An, L., & Sanjib, K. K. (2014). Evapotranspiration Estimation with Remote Sensing and Various Surface Energy Balance Algorithms—A Review. Energies (open access).

Zwart, S., Bastiaanssen, W., Garatuza-Payan, J., & Watts, C. (2006). SEBAL for detecting spatial variation of water productivity for wheat in the Yaqui Valley, Mexico. AIP Conference Proceedings, (pp. 154-161).

Appendix

Appendix 1: Mean monthly climate data at Bahir Dar weather station for the year (2014-2016)

Month	Rainfall (mm)	Aveg.Temp (0C)	Global Solar radiation (W/m2)	Avg. Wind speed (km/hr)	Wind direction (Degree)	Relative Humidity (%)
Jan	0	17.60	214.06	2.20	0.54	50.41
Feb	0.20	19.65	237.76	2.41	0.54	43.43
Mar	68.60	22.35	249.37	3.06	0.57	42.43
Apr	62.20	22.90	242.02	3.20	0.57	40.18
May	275.20	21.46	216.64	3.13	0.63	64.24
Jun	292.40	20.33	198.61	2.86	0.63	71.74
Jul	655.60	18.87	178.00	2.56	0.64	81.03
Aug	743.00	18.54	176.49	2.49	0.64	82.24
Sep	474.80	19.02	198.27	2.37	0.64	79.92
Oct	228.00	20.07	228.32	2.58	0.63	72.88
Nov	12.20	18.96	223.03	2.43	0.59	61.80
Dec	30.20	17.84	211.16	2.19	0.56	59.27

Appendix 2: Daily Etr and ETO for the month January in 2016

Month	Day	Year	Tmax C	Tmin C	Rs(MJ/m2)	Wind (m/s)	DewP C	ASCE stPM Etr (mm/d)	ASCE stPM ETO (mm/d)
1	1	2016	26.1	10.8	17.08	0.64	7.37	3.57	3.05
1	2	2016	25.8	10.3	17.75	0.52	8.43	3.38	2.99
1	3	2016	27.2	9.8	18.29	0.48	9.15	3.44	3.06
1	4	2016	28.7	10.5	18.45	0.65	7.98	3.92	3.33
1	5	2016	27.7	11.2	17.92	0.5	9.18	3.51	3.1
1	6	2016	26	9.4	15.9	0.57	7.47	3.31	2.85
1	7	2016	26	9.1	18.82	0.65	7.25	3.72	3.2
1	8	2016	26.4	8.7	18.33	0.64	7.12	3.69	3.16
1	9	2016	26	7.7	19	0.71	6.32	3.84	3.25
1	10	2016	25.9	6.6	19.41	0.81	3.56	4.14	3.4
1	11	2016	27.9	5.9	19.3	0.72	2.65	4.19	3.43
1	12	2016	26.1	7.5	16.01	0.62	5.41	3.47	2.92
1	13	2016	25.2	7.8	17.12	0.46	6.22	3.22	2.85
1	14	2016	26	8.8	17.94	0.52	5.28	3.51	3.04
1	15	2016	26.2	7.9	13.83	0.56	6.04	3.16	2.67
1	16	2016	25.9	10.5	17.61	0.54	7.51	3.49	3.05
1	17	2016	25.5	8.6	17.97	0.58	5.83	3.57	3.08
1	18	2016	25.5	6.9	18.08	0.7	4.05	3.81	3.19
1	19	2016	25.7	7.2	17.9	0.52	4.42	3.5	3.02
1	20	2016	26.4	5.1	17.54	0.5	4.07	3.45	2.97
1	21	2016	28.1	8	18.4	0.48	5.04	3.65	3.17
1	22	2016	27.2	8.6	18.16	0.53	7.66	3.6	3.15
1	23	2016	28.6	9.3	18.09	0.53	7.46	3.73	3.23
1	24	2016	26.3	10.2	17.12	0.59	8.99	3.52	3.07
1	25	2016	18.4	10.6	18.35	0.61	4.84	3.26	2.9
1	26	2016	19.95	10.09	18.17	0.57	4.63	3.3	2.92
1	27	2016	22.9	8.9	19.18	0.59	4.86	3.59	3.14
1	28	2016	24.7	7.5	18.66	0.6	4.87	3.66	3.17
1	29	2016	24.9	5.6	19.7	0.64	4.94	3.79	3.27
1	30	2016	27.4	7.3	18.72	0.49	5.18	3.69	3.22
1	31	2016	25.8	8	17.63	0.44	6.77	3.36	3
								111.04	95.85

Appendix 3: Daily Etr and ETO for the month February in 2016

Month	Day	Year	Tmax C	Tmin C	Rs(MJ/m2)	Wind (m/s)	DewP C	ASCE stPM Etr (mm/d)	ASCE stPM ETO (mm/d)
2	1	2016	27.3	8.8	19.73	0.57	7.11	3.92	3.42
2	2	2016	27	8.5	19.28	0.48	6.39	3.72	3.28
2	3	2016	28.2	11.8	20.24	0.62	8.99	4.17	3.64
2	4	2016	28.5	11.3	20.16	0.48	8.96	3.94	3.52
2	5	2016	27.5	11.3	19.98	0.58	7.63	4.06	3.55
2	6	2016	27.8	10.1	20.37	0.56	6.12	4.1	3.57
2	7	2016	27.7	9.4	20.32	0.6	6.78	4.13	3.59
2	8	2016	27.4	11	19.77	0.68	7.99	4.19	3.61
2	9	2016	28.5	10.9	19.94	0.59	8.69	4.13	3.61
2	10	2016	27.7	10.8	19.15	0.6	6.46	4.08	3.51
2	11	2016	27.6	10.5	19.9	0.54	7.35	4.01	3.53
2	12	2016	28.6	10.2	19.37	0.5	5.22	4.01	3.49
2	13	2016	28.2	11.5	17.83	0.43	6.87	3.68	3.26
2	14	2016	29.3	10.7	20.55	0.63	5.68	4.46	3.81
2	15	2016	29.5	10.6	20.83	0.55	5.68	4.35	3.77
2	16	2016	30	11.2	20.73	0.58	6.58	4.44	3.83
2	17	2016	28.2	11	20.13	0.67	6.32	4.41	3.77
2	18	2016	27.8	10.8	19.79	0.64	5.89	4.3	3.68
2	19	2016	29.7	9.8	20.4	0.51	4.91	4.26	3.7
2	20	2016	30.3	10.4	20.66	0.6	6.05	4.53	3.88
2	21	2016	30.2	10.6	20.45	0.51	3.95	4.35	3.75
2	22	2016	27.9	10.5	20.21	0.69	6.21	4.45	3.8
2	23	2016	28.5	11.6	18.67	0.64	6.25	4.28	3.64
2	24	2016	29.7	14.3	19.07	0.6	7.73	4.37	3.76
2	25	2016	30.7	13.4	19.72	0.69	8.45	4.66	3.97
2	26	2016	29.4	11.9	20.27	0.67	7.38	4.58	3.92
2	27	2016	30.6	10.8	21.27	0.94	4.08	5.48	4.42
2	28	2016	29.5	13.2	21.81	0.8	8.59	5	4.26
2	29	2016	32.2	14.9	22.04	0.78	3.88	5.46	4.49
								125.52	108.03

Appendix 4: Daily Etr and ETO for the month March in 2016

Month	Day	Year	Tmax C	Tmin C	Rs(MJ/m2)	Wind (m/s)	DewP C	ASCE stPM Etr (mm/d)	ASCE stPM ETO (mm/d)
3	1	2016	31.3	13.4	20.47	0.72	5.08	5.01	4.18
3	2	2016	30.9	11.1	21.54	0.57	5.19	4.71	4.06
3	3	2016	30.4	11.5	20.71	0.56	3.5	4.61	3.94
3	4	2016	31.4	10.7	21.59	0.6	3.57	4.87	4.13
3	5	2016	31.4	12.7	21.09	0.52	7.33	4.6	4.02
3	6	2016	30.4	13.9	20.9	0.63	6.11	4.8	4.11
3	7	2016	29.8	12.6	22.08	0.72	5.66	5.05	4.29
3	8	2016	30.8	10.7	21.98	0.65	3.08	5.02	4.23
3	9	2016	31.1	10.9	22.18	0.69	0.59	5.22	4.33
3	10	2016	31.8	10.6	21.49	0.71	0.38	5.27	4.33
3	11	2016	31.9	13	22.27	0.83	5.26	5.57	4.6
3	12	2016	33	13.7	22.46	0.8	5.93	5.63	4.67
3	13	2016	31.2	15.5	20.45	0.65	6.56	4.92	4.19
3	14	2016	30.8	16.9	21.44	0.99	10.21	5.57	4.64
3	15	2016	30.9	14	22.01	0.6	9.19	4.88	4.28
3	16	2016	31.7	16.4	20.52	0.97	9.25	5.58	4.58
3	17	2016	29.9	15	20.51	0.87	13	4.89	4.24
3	18	2016	30.4	17.4	18.97	1.01	12.37	5.13	4.29
3	19	2016	29.2	17.8	19.81	1.19	13.2	5.3	4.42
3	20	2016	30.2	17.7	22.25	0.97	11.29	5.56	4.71
3	21	2016	30	15.6	15.31	0.97	11.55	4.54	3.73
3	22	2016	30.7	14.5	19.91	0.77	8.06	5.02	4.23
3	23	2016	30.3	12.1	23.41	0.71	2.99	5.37	4.54
3	24	2016	31.6	11.2	22.94	0.7	5.47	5.34	4.53
3	25	2016	31.6	12.1	22.74	0.55	4.07	5.02	4.34
3	26	2016	31.6	16.1	22.03	0.64	5.99	5.2	4.45
3	27	2016	32.6	15	22.4	0.57	6.07	5.13	4.44
3	28	2016	32.7	13.7	22.78	0.67	4.89	5.43	4.6
3	29	2016	32.8	15.1	21.62	0.67	6.62	5.29	4.49
3	30	2016	32.3	18.9	21	0.97	10.59	5.77	4.78
3	31	2016	30.9	17	20.75	0.91	12.17	5.3	4.51
								159.6	134.88

Appendix 5: Land sat 8-satellite image information table for the day 23/December 2016

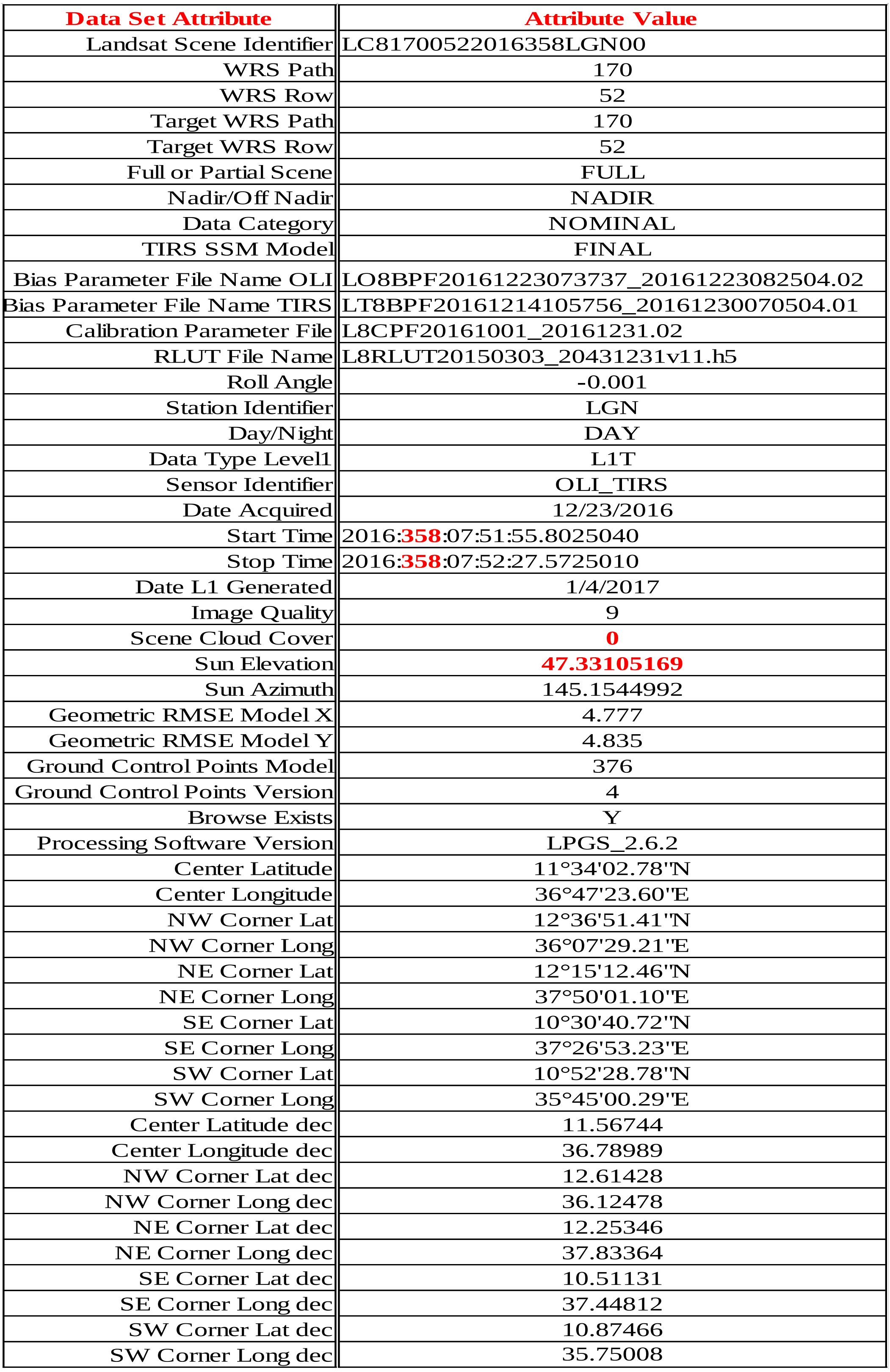

Data Set Attribute	**Attribute Value**
Landsat Scene Identifier	LC81700522016358LGN00
WRS Path	170
WRS Row	52
Target WRS Path	170
Target WRS Row	52
Full or Partial Scene	FULL
Nadir/Off Nadir	NADIR
Data Category	NOMINAL
TIRS SSM Model	FINAL
Bias Parameter File Name OLI	LO8BPF20161223073737_20161223082504.02
Bias Parameter File Name TIRS	LT8BPF20161214105756_20161230070504.01
Calibration Parameter File	L8CPF20161001_20161231.02
RLUT File Name	L8RLUT20150303_20431231v11.h5
Roll Angle	-0.001
Station Identifier	LGN
Day/Night	DAY
Data Type Level1	L1T
Sensor Identifier	OLI_TIRS
Date Acquired	12/23/2016
Start Time	2016:**358**:07:51:55.8025040
Stop Time	2016:**358**:07:52:27.5725010
Date L1 Generated	1/4/2017
Image Quality	9
Scene Cloud Cover	**0**
Sun Elevation	**47.33105169**
Sun Azimuth	145.1544992
Geometric RMSE Model X	4.777
Geometric RMSE Model Y	4.835
Ground Control Points Model	376
Ground Control Points Version	4
Browse Exists	Y
Processing Software Version	LPGS_2.6.2
Center Latitude	11°34'02.78"N
Center Longitude	36°47'23.60"E
NW Corner Lat	12°36'51.41"N
NW Corner Long	36°07'29.21"E
NE Corner Lat	12°15'12.46"N
NE Corner Long	37°50'01.10"E
SE Corner Lat	10°30'40.72"N
SE Corner Long	37°26'53.23"E
SW Corner Lat	10°52'28.78"N
SW Corner Long	35°45'00.29"E
Center Latitude dec	11.56744
Center Longitude dec	36.78989
NW Corner Lat dec	12.61428
NW Corner Long dec	36.12478
NE Corner Lat dec	12.25346
NE Corner Long dec	37.83364
SE Corner Lat dec	10.51131
SE Corner Long dec	37.44812
SW Corner Lat dec	10.87466
SW Corner Long dec	35.75008

Appendix 6: Statistics of emissivity, albedo, NDVI, LAI, surface temperature, solar radiation elements and ET for different land use/land cover in the study area.

ID	Land Cover Type	Area (km2)	%tage	Broad band surface emissivity e0f					Daily ET					Narrow band eNBf				
				Min	Max	Range	Mean	STD	Min	Max	Range	Mean	STD	Min	Max	Range	Mean	STD
1	Dense Forest	0.22	0.01	0.95	0.97	0.02	0.96	0.00	4.82	7.00	2.18	6.25	0.38	0.97	0.98	0.01	0.97	0.00
2	Moderate Forest	6.33	0.37	0.95	0.99	0.03	0.96	0.00	0.64	7.09	6.45	6.23	0.46	0.97	0.99	0.02	0.97	0.00
3	Sparse Forest	68.41	3.99	0.95	0.99	0.03	0.96	0.00	1.14	7.00	5.86	5.97	0.50	0.97	0.99	0.02	0.97	0.00
4	Closed Grassland	0.51	0.03	0.95	0.97	0.02	0.95	0.00	2.51	5.89	3.38	4.42	0.50	0.97	0.98	0.01	0.97	0.00
5	Open Grassland	49.43	2.88	0.95	0.99	0.03	0.95	0.00	0.63	7.17	6.55	5.42	0.77	0.97	0.99	0.02	0.97	0.00
6	Open Shrubland	61.67	3.60	0.95	0.99	0.03	0.95	0.00	0.27	6.81	6.54	4.96	0.62	0.97	0.99	0.02	0.97	0.00
7	Annual Cropland	1,516.57	88.49	0.95	0.99	0.03	0.95	0.00	0.00	7.09	7.09	4.69	0.73	0.97	0.99	0.02	0.97	0.00
8	Water Body	5.99	0.35	0.95	0.99	0.03	0.96	0.02	3.25	7.39	4.14	5.13	1.15	0.97	0.99	0.02	0.98	0.01
9	Settlement	4.72	0.28	0.95	0.96	0.01	0.95	0.00	3.17	6.69	3.52	5.20	0.51	0.97	0.97	0.00	0.97	0.00

ID	Land Cover Type	Area (km2)	%tage	Incoming longwave radiation					Incoming shortwave radiation					Instantaneous ET				
				Min	Max	Range	Mean	STD	Min	Max	Range	Mean	STD	Min	Max	Range	Mean	STD
1	Dense Forest	0.22	0.01	377.89	379.25	1.35	378.70	0.29	816.42	824.11	7.69	819.56	1.66	0.679	0.99	0.31	0.88	0.05
2	Moderate Forest	6.33	0.37	377.22	379.39	2.17	378.70	0.31	815.57	827.87	12.30	819.55	1.74	0.09	1.00	0.91	0.88	0.06
3	Sparse Forest	68.41	3.99	376.62	379.51	2.90	378.93	0.35	814.88	831.19	16.31	818.20	2.01	0.16	0.99	0.83	0.84	0.07
4	Closed Grassland	0.51	0.03	378.17	379.23	1.06	378.89	0.24	816.50	822.57	6.07	818.48	1.38	0.353	0.83	0.48	0.62	0.07
5	Open Grassland	49.43	2.88	376.39	379.56	3.16	378.92	0.38	814.61	832.40	17.79	818.27	2.17	0.088	1.01	0.92	0.76	0.11
6	Open Shrubland	61.67	3.60	376.49	379.46	2.97	378.74	0.35	815.20	831.88	16.68	819.31	2.01	0.038	0.96	0.92	0.70	0.09
7	Annual Cropland	1,516.57	88.49	375.99	379.58	3.59	378.75	0.42	814.47	834.58	20.11	819.26	2.39	0	1.00	1.00	0.66	0.10
8	Water Body	5.99	0.35	378.16	379.58	1.42	379.11	0.20	814.47	822.61	8.14	817.18	1.17	0.457	1.04	0.58	0.72	0.16
9	Settlement	4.72	0.28	378.01	379.03	1.02	378.46	0.19	817.67	823.49	5.82	820.93	1.06	0.446	0.94	0.50	0.73	0.07

ID	Land Cover Type	Area (km2)	%tage	LAI					Latent heat flux					Net Radiation				
				Min	Max	Range	Mean	STD	Min	Max	Range	Mean	STD	Min	Max	Range	Mean	STD
1	Dense Forest	0.22	0.01	0.03	1.92	1.89	0.79	0.30	462.39	671.01	208.62	599.44	36.08	553.03	688.26	135.23	642.26	23.17
2	Moderate Forest	6.33	0.37	0.00	1.72	1.72	0.69	0.25	61.32	679.31	617.99	597.22	43.75	54.22	705.48	651.26	642.41	33.06
3	Sparse Forest	68.41	3.99	0.00	3.46	3.46	0.54	0.26	108.99	670.90	561.91	572.46	47.89	115.79	718.87	603.08	629.35	32.28
4	Closed Grassland	0.51	0.03	0.00	1.53	1.53	0.12	0.12	240.52	564.77	324.25	423.53	47.83	454.62	621.05	166.43	532.99	29.69
5	Open Grassland	49.43	2.88	0.00	3.41	3.41	0.39	0.33	60.18	687.84	627.66	519.55	73.68	377.66	741.90	364.24	602.11	43.66
6	Open Shrubland	61.67	3.60	0.00	4.06	4.06	0.30	0.27	26.06	652.95	626.89	475.59	59.28	39.23	709.49	670.26	568.45	36.89
7	Annual Cropland	1,516.57	88.49	0.00	4.38	4.38	0.23	0.18	(84.20)	679.29	763.49	449.34	70.31	(125.31)	733.68	858.99	555.69	42.51
8	Water Body	5.99	0.35	0.00	1.76	1.76	0.14	0.22	311.33	708.26	396.93	491.91	110.64	482.70	754.55	271.86	644.61	36.52
9	Settlement	4.72	0.28	0.00	1.10	1.10	0.16	0.17	303.59	641.00	337.41	498.51	48.85	396.50	681.32	284.82	580.30	38.66

ID	Land Cover Type	Area (km2)	%tage	Outgoing longwave radiation					Reference ET fraction					SAVI				
				Min	Max	Range	Mean	STD	Min	Max	Range	Mean	STD	Min	Max	Range	Mean	STD
1	Dense Forest	0.22	0.01	428.66	478.73	50.07	446.88	10.25	1.114	1.62	0.50	1.44	0.09	0.12	0.59	0.47	0.39	0.08
2	Moderate Forest	6.33	0.37	422.39	500.21	77.82	445.64	9.95	0.148	1.64	1.49	1.44	0.11	(0.11)	0.57	0.68	0.37	0.08
3	Sparse Forest	68.41	3.99	417.05	507.82	90.77	450.31	16.01	0.263	1.62	1.35	1.38	0.12	(0.21)	0.66	0.88	0.32	0.08
4	Closed Grassland	0.51	0.03	456.88	511.37	54.49	486.02	9.76	0.579	1.36	0.78	1.02	0.12	0.06	0.54	0.48	0.16	0.04
5	Open Grassland	49.43	2.88	417.97	528.06	110.09	467.64	19.17	0.145	1.66	1.51	1.25	0.18	(0.20)	0.66	0.86	0.26	0.11
6	Open Shrubland	61.67	3.60	407.28	527.22	119.94	477.52	13.45	0.063	1.57	1.51	1.15	0.14	(0.19)	0.68	0.87	0.23	0.09
7	Annual Cropland	1,516.57	88.49	408.50	533.12	124.62	483.02	14.65	0	1.64	1.64	1.08	0.17	(0.26)	0.68	0.94	0.21	0.07
8	Water Body	5.99	0.35	406.25	496.16	89.91	450.03	17.50	0.75	1.71	0.96	1.18	0.27	(0.21)	0.57	0.79	0.08	0.17
9	Settlement	4.72	0.28	435.49	499.54	64.06	467.36	10.83	0.731	1.54	0.81	1.20	0.12	0.00	0.47	0.47	0.17	0.08

ID	Land Cover Type	Area (km2)	%tage	Sensible heat flux					Soil heat flux					Temprature 0c				
				Min	Max	Range	Mean	STD	Min	Max	Range	Mean	STD	Min	Max	Range	Mean	STD
1	Dense Forest	0.22	0.01	(35.91)	(3.38)	32.53	(23.49)	6.23	46.20	94.03	47.83	66.28	10.51	24.81	33.59	8.78	28.10	1.81
2	Moderate Forest	6.33	0.37	(35.50)	49.90	85.40	(23.30)	5.85	14.21	343.89	329.68	68.50	10.88	23.69	37.14	13.45	27.93	1.77
3	Sparse Forest	68.41	3.99	(41.04)	99.04	140.08	(19.43)	8.55	28.67	359.43	330.76	76.32	15.25	21.69	38.40	16.71	28.77	2.74
4	Closed Grassland	0.51	0.03	(17.57)	130.86	148.44	12.70	23.37	60.18	102.46	42.28	96.76	3.88	30.06	38.91	8.84	34.97	1.56
5	Open Grassland	49.43	2.88	(35.98)	309.53	345.51	(4.87)	26.15	44.09	370.95	326.86	87.43	27.69	21.53	41.43	19.90	31.71	3.28
6	Open Shrubland	61.67	3.60	(35.74)	304.33	340.07	1.31	21.65	19.61	354.75	335.13	91.55	10.56	21.73	41.36	19.63	33.44	2.29
7	Annual Cropland	1,516.57	88.49	(38.49)	373.26	411.75	11.94	30.93	(49.68)	366.84	416.52	94.41	9.25	21.86	42.15	20.29	34.36	2.44
8	Water Body	5.99	0.35	(36.76)	34.19	70.95	(16.78)	6.16	51.57	377.28	325.71	169.48	118.93	20.24	36.65	16.41	28.10	3.45
9	Settlement	4.72	0.28	(27.86)	49.27	77.13	(8.71)	6.88	51.04	101.30	50.27	90.49	6.09	26.34	37.12	10.78	31.92	1.83

ID	Land Cover Type	Area (km2)	%tage	NDVI					Surface albedo					Seasonal ET				
				Min	Max	Range	Mean	STD	Min	Max	Range	Mean	STD	Min	Max	Range	Mean	STD
1	Dense Forest	0.22	0.01	0.19	0.81	0.63	0.66	0.11	0.07	0.20	0.13	0.11	0.02	587.52	812.40	224.88	732.88	43.97
2	Moderate Forest	6.33	0.37	(0.54)	0.81	1.35	0.62	0.13	0.05	0.43	0.38	0.11	0.03	424.14	812.58	388.44	729.33	48.57
3	Sparse Forest	68.41	3.99	(0.68)	0.85	1.52	0.55	0.12	0.04	0.50	0.46	0.12	0.03	411.27	817.96	406.69	693.85	68.77
4	Closed Grassland	0.51	0.03	0.11	0.77	0.66	0.24	0.07	0.11	0.29	0.18	0.19	0.03	308.07	639.72	331.65	527.66	48.88
5	Open Grassland	49.43	2.88	(0.84)	0.84	1.67	0.44	0.18	0.03	0.37	0.35	0.13	0.04	114.77	819.69	704.92	612.09	90.21
6	Open Shrubland	61.67	3.60	(0.72)	0.83	1.55	0.36	0.14	0.06	0.48	0.43	0.16	0.03	152.77	781.97	629.19	556.12	78.25
7	Annual Cropland	1,516.57	88.49	(0.81)	0.84	1.65	0.32	0.12	0.03	0.49	0.46	0.17	0.04	49.12	804.21	755.09	528.08	95.65
8	Water Body	5.99	0.35	(0.90)	0.79	1.70	0.12	0.34	0.03	0.27	0.24	0.11	0.04	401.29	802.78	401.48	618.61	104.84
9	Settlement	4.72	0.28	0.01	0.79	0.78	0.29	0.13	0.07	0.36	0.29	0.16	0.04	393.08	785.80	392.71	612.76	60.42

Appendix 7: Organization of datasets

1. Download at [Earth Explorer] (http://earthexplorer.usgs.gov/) Landsat 8 scene (LS8 - OLI/TIRS)
    - For a scene without clouds, select the option **Level 1 GeoTIFF Data Product**

2. Reproject LS8 images for the coordinate system of interest
    - e.g, WGS 84 24N to SIRGAS 2000 24S, using gdal recursively in command line:

    -
      ```
      mkdir rep && for i in *.TIF ; do gdalwarp -s_srs EPSG:32624 -t_srs EPSG:31984 -of GTiff $i rep\$i; done
      ```

3. Remove null values (black borders) of LS8 images
    - e.g, using gdal recursively in command line:

    -
      ```
      mkdir nodata && for i in *.TIF; do gdal_translate -a_nodata 0 $i nodata/$i; done
      ```

4. Download at [Earth Explorer] (http://earthexplorer.usgs.gov/) the Digital Elevation Model (DEM) from ASTER (remember to choose the same region of LS8 scene)

5. It is necessary to reproject the DEM for the coordinate system of interest and rename to **MDT_Sebal.TIF**
    - e.g, WGS 84 24N to SIRGAS 2000 24S, using gdal in command line:

    -
      ```
      gdalwarp -s_srs EPSG:32624 -t_srs EPSG:31984 -of GTiff ASTGTM2_S23W048.tif MDT_Sebal.TIF
      ```

6. Launch a GRASS-GIS 7.X session
    - Select GRASS GIS database directory
    - Define a new GRASS location
        - Read the projection and datum terms from a georeferenced data file
        - Select the raster **MDT_Sebal.TIF**
    - Define a new GRASS mapset

7. Place **Sebal70.py** script in the directory where LS8 images are located